

AN ABSTRACT FOR THE THESIS OF

Louise M. Douglas Priebe for the degree of Master of Science in Oceanography presented on March 3, 1998. Title: Geochemical and Petrogenetic Effects of the Interaction of the Southeast Indian Ridge and the Amsterdam-Saint Paul Hotspot.

Redacted for privacy

Abstract approved: _____

David W. Graham

The interaction of a migrating mid-ocean ridge and a near-ridge hotspot has a significant effect on the geochemistry of magmas produced at the ridge. Although a ridge may have migrated away from a mantle plume on which it was previously centered, it can continue to feel the effects of the hotspot's presence up to distances as great as 1000 km. The construction of the Amsterdam-Saint Paul (ASP) platform on the Southeast Indian Ridge (SEIR) is the result of the ASP mantle plume, which initially lay under the Australian Plate, but because the SEIR has migrated northeastward during the last several million years, today lies approximately 50-100 km southwest of the ridge. The area of the ASP platform today continues to feel the effect of hotspot-ridge interaction.

Mantle plumes represent mantle heterogeneities and each plume has an individual signature with varying major element behavior and degree of enrichment relative to normal mantle composition. Some hotspots (e.g. Galapagos, Azores) influence the chemical composition of mid-ocean ridges so that they do not show the same relationship between chemistry and axial depth as normal mid-ocean ridges, whereas other hotspots (e.g. Iceland) show behavior more consistent with global correlations. In the ASP

region, Fe₈ is lower and Na₈ and CaO/Al₂O₃ are higher than predicted by global axial depth correlations. High pressure crystallization of clinopyroxene may be in part, responsible for the ASP lavas falling intermediate to the 'local' and 'global' trends of Klein and Langmuir.

Polybaric crystallization best explains the trends of the ASP data. Three-phase saturation (olivine:plagioclase:clinopyroxene) is most common, but some lavas are only two-phase saturated.

Lavas atop the ASP platform are more fractionated than those away from the platform and are enriched in incompatible elements. The enrichment of incompatible elements extends beyond the platform to the northwest, and is attributed to the ASP plume. Minor element concentrations such as K₂O, TiO₂ and P₂O₅ show that an over-enriched mantle plume source is mixing with depleted, and also possibly enriched mantle to produce the ASP lavas.

Geochemical and Petrogenetic Effects of the Interaction of the Southeast
Indian Ridge and the Amsterdam-Saint Paul Hotspot

by

Louise M. Douglas Priebe

A Thesis Submitted

to

Oregon State University

In Partial Fulfillment of
the requirements for the degree of
Master of Science

Presented March 3, 1998
Commencement June 1998

Master of Science thesis of Louise M. Douglas Priebe presented on March 3, 1998.

Approved:

Redacted for privacy

Major Professor, representing Oceanography

Redacted for privacy

Dean of College of Oceanography and Atmospheric Sciences

Redacted for privacy

Dean of Graduate School

I understand that my thesis will become part of the permanent collection of Oregon State University libraries. My signature below authorizes release of my thesis to any reader upon request.

Redacted for privacy

Louise M. Douglas Priebe, Author

Acknowledgments

Thanks to my advisor, David Graham, for providing guidance and support during the course of my project. Many thanks also to Anita Grunder and Dave Christie for their helpful comments and suggestions.

I'm grateful for the help with both the electron microprobe analyses, and the crystallization modeling provided by Roger Nielsen.

I am indebted to Kurt for keeping me well fed and watered, and relatively sane while I've been in graduate school.

This research was supported by a grant from the National Science Foundation.

Table of Contents

Section	Page
Introduction	1
Regional Setting	4
Methods	9
Sampling Methods	9
Analytical Methods	14
Compositional Variation of the Basalt Glasses	23
Regional-Scale Variations	23
Segment-Scale Variations	28
Variations in CaO/Al ₂ O ₃ and Fractionation-Corrected Na ₂ O and FeO*	34
Chlorine and Sulfur Variations	38
Discussion	50
Implications of Assimilation	50
Global Major Element Correlations	53
Crystallization	60
Distribution of Plume Material	67
Conclusions	88
Bibliography	90
Appendices	96

List of Figures

Figure		Page
1.	Regional bathymetry of the Southern Indian Ocean.	2
2.	Satellite gravity map of the ASP platform and the surrounding area.	6
3.	Distribution of sampling stations as a function of distance along-axis and depth.	8
4.	Variation of SiO_2 as a function of MgO.	24
5.	Variation of FeO^* (total Fe as FeO^*) as a function of MgO .	25
6.	Along-axis chemical variations in the 126 different chemical groups of the study area.	26
7.	A) TiO_2 , B) K_2O and C) $\text{K}_2\text{O}/\text{TiO}_2$ as a function of MgO.	29
8.	Variations of P_2O_5 , TiO_2 and K_2O .	33
9.	TiO_2 versus $\text{K}_2\text{O}/\text{TiO}_2$ and $\text{P}_2\text{O}_5/\text{TiO}_2$.	35
10.	Along-axis variations in fractionation-corrected oxides.	37
11.	Cl and Cl/K as a function of MgO.	39
12.	Variations of Cl and Cl/K along-axis.	41
13.	A) TiO_2 , B) P_2O_5 and C) K_2O as a function of Cl.	42
14.	A) $\text{K}_2\text{O}/\text{TiO}_2$ vs. Cl/K, B) TiO_2 vs. Cl/ TiO_2 and C) P_2O_5 vs. Cl/ P_2O_5 .	43
15.	A) MgO, B) FeO^* and C) TiO_2 vs. S.	47
16.	Variation of S as a function of distance along-axis.	48
17.	S versus $\text{K}_2\text{O}/\text{TiO}_2$.	49
18.	Klein and Langmuir's mantle melting column model.	54
19.	Along-axis variations in observed and predicted fractionation-corrected oxides.	56
20.	A) Fe_8 vs. Na_8 and B) Si_8 vs. Na_8 .	59

List of Figures, Continued.

Figure	Page
21. Isobaric fractional crystallization model.	62
22. Polybaric fractional crystallization model.	64
23. Variation of K_2O/TiO_2 in the area of the ASP platform.	69
24. Covariation of fractionation-corrected minor elements.	70
25. Fractionation-corrected minor element ratios.	73
26. Melting model of the ASP data.	76

List of Tables

Table		Page
1.	Sampling sites.	10
2.	Glass analyses.	15
3.	Chlorine and sulfur analyses.	21
4.	Partition coefficients and modes used in melting model.	83

List of Appendices

Appendix	Page
1. Ungrouped Major Element Data.	97
2. Analyses of the Basalt Glass Standard VG-A99.	112
3. Analyses of the Basalt Glass Standard IOB.	118
4. Unaveraged Chlorine and Sulfur Data.	124
5. Analyses of Kakanui Augite.	128
6. Calculation of Eight Values.	130

Preface

The study of mid-ocean ridge basalts is a means of understanding the interior of the earth. From mid-ocean ridge basalts we can learn about the composition of the Earth's mantle, and the processes that occur within the mantle and crust. Mid-ocean ridge basalts are produced from the partial melting of mantle peridotite beneath mid-ocean ridges; the melt rises to the surface and is erupted along the global mid-ocean ridge system. The geochemical composition of these mid-ocean ridge basalts can tell us rather specifically what processes have occurred during melt segregation, ascent to the surface, and eruption. In order to interpret correctly what mid-ocean ridge basalt compositions tell us, we have to recognize the signature(s) of each process.

Three major factors contribute to the diversity of mid-ocean ridge basalt compositions (Langmuir et al., 1992). 1) Shallow-level crystallization and differentiation processes modify the compositions of mantle melts. 2) The degree of melting of the mantle affects mid-ocean ridge basalt composition. 3) Heterogeneity in major element, trace element and isotopic mantle compositions will cause variations in mid-ocean ridge basalt composition. One example of mantle heterogeneity is mantle hotspots. Hotspots are supplied with large ion lithophile-rich mantle while normal mid-ocean ridges, unaffected by hotspots, are supplied with large ion lithophile-depleted mantle. The degree of large ion lithophile enrichment and radiogenic Sr and Pb contents varies from one hotspot to another (Schilling, 1986).

Both major and minor element compositions of basalt glasses can be used to unravel the processes occurring beneath a mid-ocean ridge. Variations in fractionation-corrected, mid-ocean ridge basalt oxides reflect varying degrees of melting and varying depths of melting of a peridotitic mantle source (Klein and Langmuir, 1987). Ratios of incompatible elements (e.g. K_2O/TiO_2) can be used to determine source enrichment on

the basis that they are least effected by fractionation processes during magma formation and emplacement into the oceanic crust, such as partial melting and fractional crystallization (Schilling, 1986). Incompatible element ratios are fairly representative of the mantle source they have been derived from, indicating whether a source is enriched or depleted.

Hotspots can play a significant role in the development of some mid-ocean ridge basalts. Hotspots are enriched mantle domains which are buoyant and rise as plumes that interact and mix with the large ion lithophile-depleted asthenosphere (Schilling, 1986). The plumes remain essentially fixed with respect to each other and to the lower mantle (Morgan, 1981, 1983) and have variable lifetimes with some extending up to several tens or even hundreds of millions of years. Because of the enrichment of the plume, at a constant temperature, it will begin melting sooner (deeper) than depleted large ion lithophile asthenosphere (Shilling, 1973a). If a hotspot is ridge-centered the increased melting can create thicker crust over the hotspot, with the excess plume material spreading laterally along the spreading axis. The sub-lithospheric flow of plume material along-axis is progressively diluted with large ion lithophile-depleted asthenospheric material, thus generating compositionally gradational lavas (Schilling, 1986). If the ridge is migrating away from the hotspot, it is hypothesized that the spreading ridge axis continues to act as a sink for the plume (Morgan, 1978; Schilling 1985, 1991; Schilling et al., 1985). A sub-lithospheric channel develops and extends with time between the hotspot and the migrating ridge thus producing a geochemical anomaly on the ridge crest nearest the hotspot.

My thesis is a part of a multi-disciplinary project involving the Amsterdam-Saint Paul Platform along the Southeast Indian Ridge. In the past three years the SEIR database has been vastly expanded with three Southeast Indian Ridge cruises on the R/V *Melville*: Westward 9 and 10 in 1994 - 1995 with PI's D. Christie, J. Cochran and J.C. Sempéré, and Boomerang 06 in 1996, with PI's K Johnson and D. Scheirer. The

combined geochemical and geophysical data sets encompass over 4000 km of the Southeast Indian Ridge, from just west of the Amsterdam-Saint Paul platform to the Australian-Antarctic Discordance, and include the major element chemistry of the glasses, high resolution bathymetry, and gravity and magnetics data. Trace element, helium, and isotope analyses are also underway.

The Southeast Indian Ridge region is intriguing for several reasons. 1) The Southeast Indian Ridge exhibits a gradient of characteristics generally associated with a changing spreading rate while maintaining a nearly constant spreading rate of 70 mm/yr. (Sempéré et al., 1995). 2) There is a mantle temperature gradient that results in warm mantle beneath the Amsterdam-Saint Paul platform and colder than normal mantle beneath the Australian-Antarctic Discordance (Forsyth et al, 1987; Marks et al, 1991). 3) A shift in morphology from an axial high in the west to axial valley in the east occurs (Cochran, 1991). 4) There are two near-ridge hotspots in this region, both of which may interact with the Southeast Indian Ridge, though to different degrees. The Amsterdam - Saint Paul hotspot is approximately 50-100 km southwest of the Southeast Indian Ridge, and the Kerguelen hotspot is almost 1100 km southwest of the Southeast Indian Ridge.

My thesis focuses on what we can learn about ridge-hotspot interaction through the effect that it has on the major and minor element compositions of basalt glasses from the ASP region.

Geochemical and Petrogenetic Effects of the Interaction of the Southeast Indian Ridge and the Amsterdam-Saint Paul Hotspot

Introduction

The interaction of a migrating mid-ocean ridge and a near-ridge hotspot has a significant effect on the geochemistry of the magmas produced at the ridge (e.g. Galapagos Spreading Center, Tristan da Cunha) (Schilling et al., 1985). The mantle-plume source / migrating-ridge sink model hypothesizes that flow from a hotspot is channeled along the base of the lithosphere to the ridge (Morgan, 1978; Schilling, 1985, 1991; Schilling et al., 1985). For nearly all near-ridge plumes studied to date, the initial condition is taken to be one in which the mantle plume is ridge-centered. Through time the ridge migrates away from the hotspot; although the ridge moves away, a thermal "pipeline" is established and maintained to distances as great as 1000 km (Schilling, 1991). During this period the ridge acts as a sink, drawing in LILE-rich (large-ion lithophile) plume material, and magmas are produced at the ridge with geochemical affinities to those of the nearby hotspot. For both a ridge-centered plume and a near-ridge plume, the along-axis trace element and isotope gradients are a result of mixing between the LILE-rich plume material and LILE-depleted mantle (Schilling, 1973). However, in the case of a near-ridge plume the gradients produced are not as long as those produced by a ridge-centered plume because the dispersion of plume material along the length of the ridge in question, to a first order varies inversely with the radial distance to the plume (Schilling et al., 1985).

The Southeast Indian Ridge (SEIR), extends over 5000 km, from the Rodriguez Triple Junction (25.5°S, 70.0°E) in the west, to the Macquarie Ridge Complex southeast of Australia (Figure 1). Important geologic features of the Indian Ocean include 90°E Ridge, Broken Ridge, the Amsterdam-Saint Paul (ASP) hotspot and platform, and the

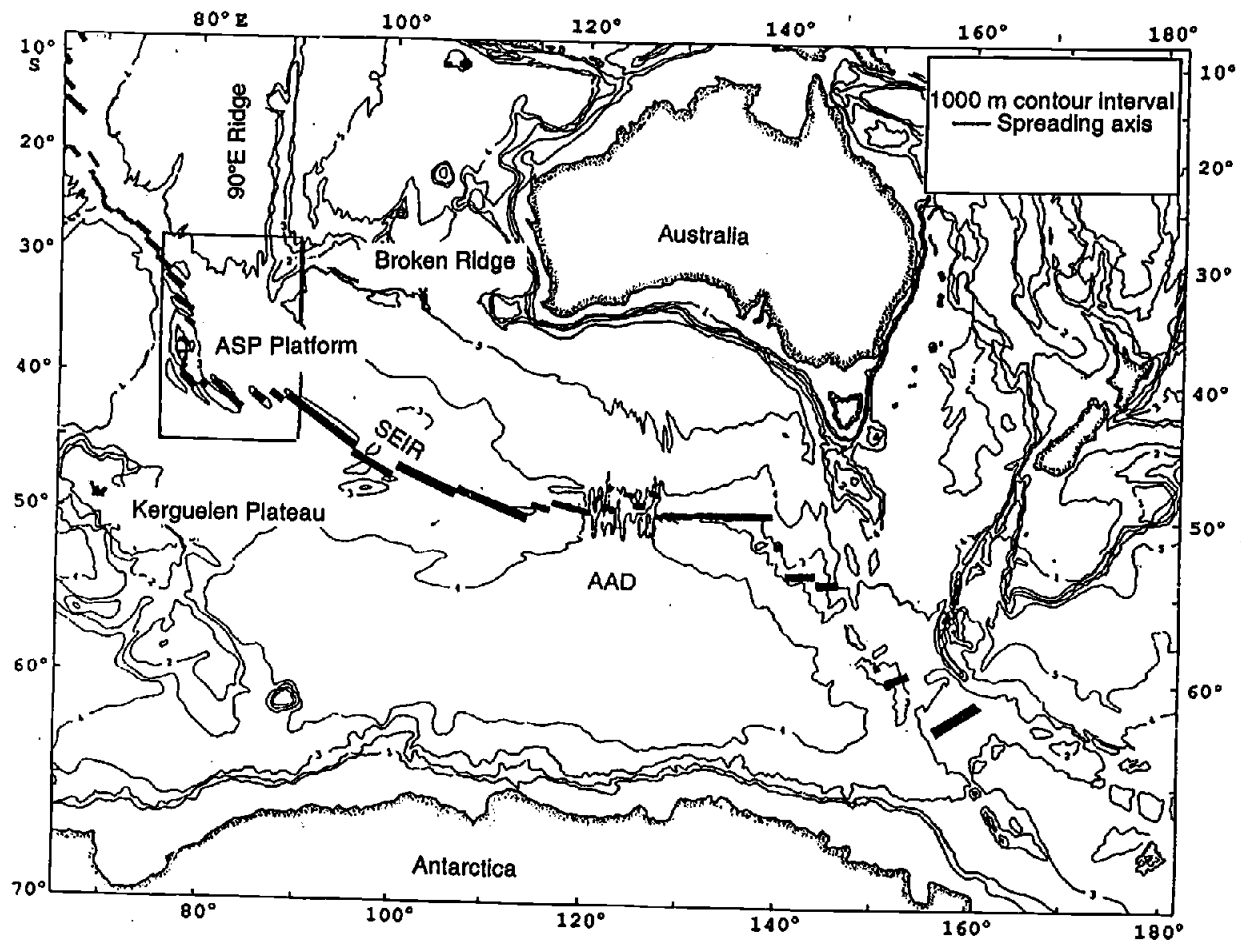


Figure 1: Regional bathymetry of the Southeast Indian Ocean. Modified from Pyle et al., 1992. Note the u-shaped deviation of the SEIR in the vicinity of the ASP platform.

Kerguelen hotspot and platform. The ASP hotspot lies approximately 50-100 km southwest of the SEIR while the Kerguelen hotspot lies almost 1100 km southwest of the SEIR. The locations of the ASP and Kerguelen hotspots relative to the SEIR provide the opportunity to study ridge-hotspot interaction at two different length-scales, and potentially, with varying degrees of influence at different times.

Prior to 1996, the SEIR in the area of the ASP platform was sparsely sampled, with only 20 reported geochemical analyses for the entire northern SEIR (excluding the Rodriguez Triple Junction). These geochemical data were generated from two French cruises on the R/V *Jean Charcot* and the R/V *Marion Dufresne*, in 1984 (Hamelin et al., 1986; Michard et al., 1986; Dosso et al., 1988). However, in early 1996 the Boomerang 06 expedition was undertaken aboard the R/V *Melville*. This was an integrated geochemical and geophysical investigation of the SEIR in the vicinity of the ASP platform. The field program carried out a high resolution bathymetric, sidescan sonar, dredging, glass-coring, gravity and magnetics study. This paper deals with the major element contents as well as the chlorine and sulfur contents, of the basalt glass samples collected. Our primary goal in studying the along-axis major element variations in this area is to understand the geochemical effects of the interaction between the SEIR and the ASP hotspot. Possible effects include variations in the nature of the melting processes beneath the SEIR, diversion of mantle flow from the SEIR to the ASP platform, and 'contamination' of the SEIR lavas by a plume component (s).

Regional Setting

Kerguelen Island and Plateau is the result of a major hotspot. This hotspot has an estimated volumetric flux of $3 \text{ km}^3/\text{yr.}$, the largest flow volume of all near-ridge hotspots (Schilling, 1991). For comparison, the flux of the Hawaiian plume, an intraplate hotspot, is $9\text{-}12 \text{ km}^3/\text{yr.}$ Storey et al. (1989) suggested that the Kerguelen mantle plume was responsible for "contaminating" the entire Indian Ocean asthenosphere, creating the unique isotopic composition of Indian Ocean MORB (Dupré and Allègre, 1983; Hamelin et al., 1986; Ito et al., 1987). Indian Ocean MORB are isotopically distinct from Pacific and Atlantic MORB, having higher $^{87}\text{Sr}/^{86}\text{Sr}$, $^{208}\text{Pb}/^{206}\text{Pb}$ and $^{207}\text{Pb}/^{206}\text{Pb}$ ratios. It is hypothesized that Indian Ocean mantle has remained at least partially isolated from the global system, preventing homogenization, and allowing the isotopic signature of the Indian Ocean to remain distinct (Hamelin et al., 1986).

Located today approximately 1100 km southwest of the SEIR and the ASP platform, the Kerguelen hotspot developed soon after the separation of India from E. Gondwana in the mid-Cretaceous (Royer and Coffin, 1992). As the Australian Plate moved northward, the trace of the Kerguelen plume was marked by the formation of 90°E Ridge, a >4,500 km-long aseismic ridge. The Kerguelen hotspot was also responsible for the construction of Broken Ridge which was attached to Kerguelen Plateau prior to 58 Ma. During the Eocene, the present SEIR formed and began spreading, splitting apart Kerguelen Plateau and Broken Ridge roughly at the site of the hotspot (Royer and Sandwell, 1989). Today Broken Ridge and Kerguelen Plateau are located to the north and south of the SEIR respectively, in roughly symmetrical positions with respect to the SEIR (Mutter and Cande, 1983). Because the Antarctic Plate is nearly fixed in the hotspot frame (Gripp and Gordon, 1990) and spreading has been roughly symmetric (Royer and Schlich, 1988), the SEIR is migrating to the

northeast in a fixed hotspot frame, at approximately half the rate (17 mm/yr.) of the Australian plate (35 mm/yr.). Since spreading began the SEIR has continuously moved northeast away from the Kerguelen hotspot.

ASP is a smaller volume hotspot than Kerguelen as inferred from a comparison of plateau areas, and Morgan (1978) hypothesized that ASP was a secondary hotspot created by channelized flow from Kerguelen to the ridge. More recent isotopic work has shown that ASP lavas have higher $^{206}\text{Pb}/^{204}\text{Pb}$ and $^{143}\text{Nd}/^{144}\text{Nd}$, and lower $^{87}\text{Sr}/^{86}\text{Sr}$ than Kerguelen lavas (White, 1982; Hamelin et al., 1986; Dosso et al., 1988), and the ASP hotspot therefore likely constitutes an independent plume. Although ASP is apparently a separate hotspot, Kerguelen may still influence the composition of the ridge, both through a wide-spread "background" contamination as suggested by Storey et al. (1989), and also possibly through some type of channelized flow, as suggested by a pronounced Kerguelen isotopic signature in MORB dredged off-axis near the St. Paul Fracture Zone (Dosso et al., 1988).

Initially the ASP hotspot lay under the Australian Plate but because the SEIR has continued to migrate northeastward during the last several million years, the hotspot today should lie beneath the Antarctic Plate approximately 50-100 km southwest of the ridge. The apparent trail of the ASP hotspot on the Australian Plate is marked by rough gravity anomalies, presumably corresponding to seamounts or aseismic ridges (Figure 2). This trail leads into a pronounced U-shaped southward deviation of the SEIR in the vicinity of the ASP platform (Figures 1 and 2). During the last several million years, as the SEIR approached the vicinity of the ASP hotspot, flow of hotter plume material may have been diverted towards the ridge axis, and increased melt production beneath the ridge probably contributed significantly to the construction of the ASP platform. Platform building continues today as evidenced by the young volcanic edifices and lava fields off-axis of the SEIR, atop the ASP platform. Now that the ridge has apparently migrated away from the plume, and the hotspot lies beneath the essentially stationary

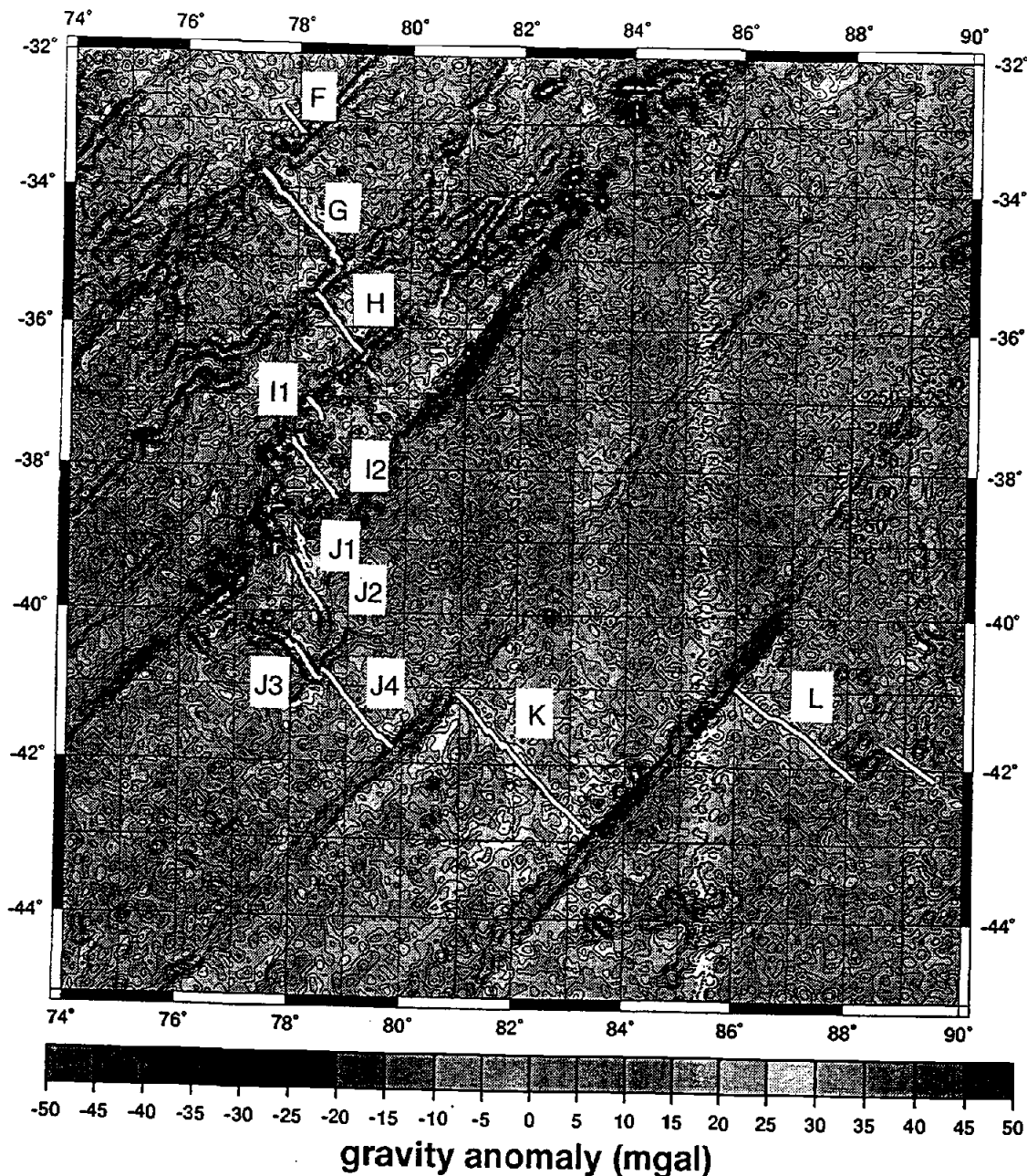


Figure 2: Satellite gravity map of the ASP platform and the surrounding area (Sandwell and Smith, 1992). In the vicinity of the ASP platform (77°E - 88°E) there are eleven ridge segments, labeled here as segments F through L, following Royer and Schlich (1988), four of which cross the ASP platform in stair-step fashion (segments I1 - J2). The segments range from 40 - 285 km in length with offsets of 10 - 300 km.

Antarctic Plate, island edifices and seamounts such as St. Paul and Amsterdam Islands, and St. Pierre and Boomerang Seamounts, are being built on non-zero age (< 6 Ma) seafloor. Asymmetries in seafloor spreading or changes in plate boundary geometry due to ridge-hotspot interaction are still poorly understood in this region. To the southeast of the platform, some minor ridge jumps have transferred material to the Australian Plate, but overall the shape of the ridge reflects the original shape at the time of the breakup between Kerguelen Plateau and Broken Ridge (Royer and Sandwell, 1989).

In the vicinity of the ASP platform (77°E - 88°E) the spreading axis has an intermediate spreading rate (62-77 mm/yr.) along eleven different ridge segments, four of which cross the ASP platform in stair-step fashion (Figure 2). The segments range from 40 to 285 km in length, deepen towards the segment ends, and offsets are 10 to 300 km. The depth of the ridge axis reaches its shallowest point at 1400 m atop the platform, and its deepest point at 3700 m on segment F (Figure 3). In general, the topographic expression of the spreading axis is a narrow (< 2 km) and shallow (< 100 m) valley, sometimes containing a small central ridge or a group of circular volcanic cones. In places, the center of the neovolcanic zone is topographically indistinct from the adjacent flanks and recent volcanism is distributed over a wide area. A large propagating rift is present at the southeast of segment J2. The southern tip of the J2 propagator has propagated at least twice to the south during the past million years, and the oceanic crust caught in the overlap region between segments J2 and J1 has been sheared and rotated progressively, resulting in a region of complex magnetic anomalies and diffuse seismicity. Atop the ASP platform, segments J1, I2, and I1 are organized as an echelon neovolcanic zones, with significant overlap and sinuous geometry. The magnetic anomalies in this area are generally coherent, but often they cannot be readily correlated with the expected magnetic reversal sequence (Scheirer et al., 1996).

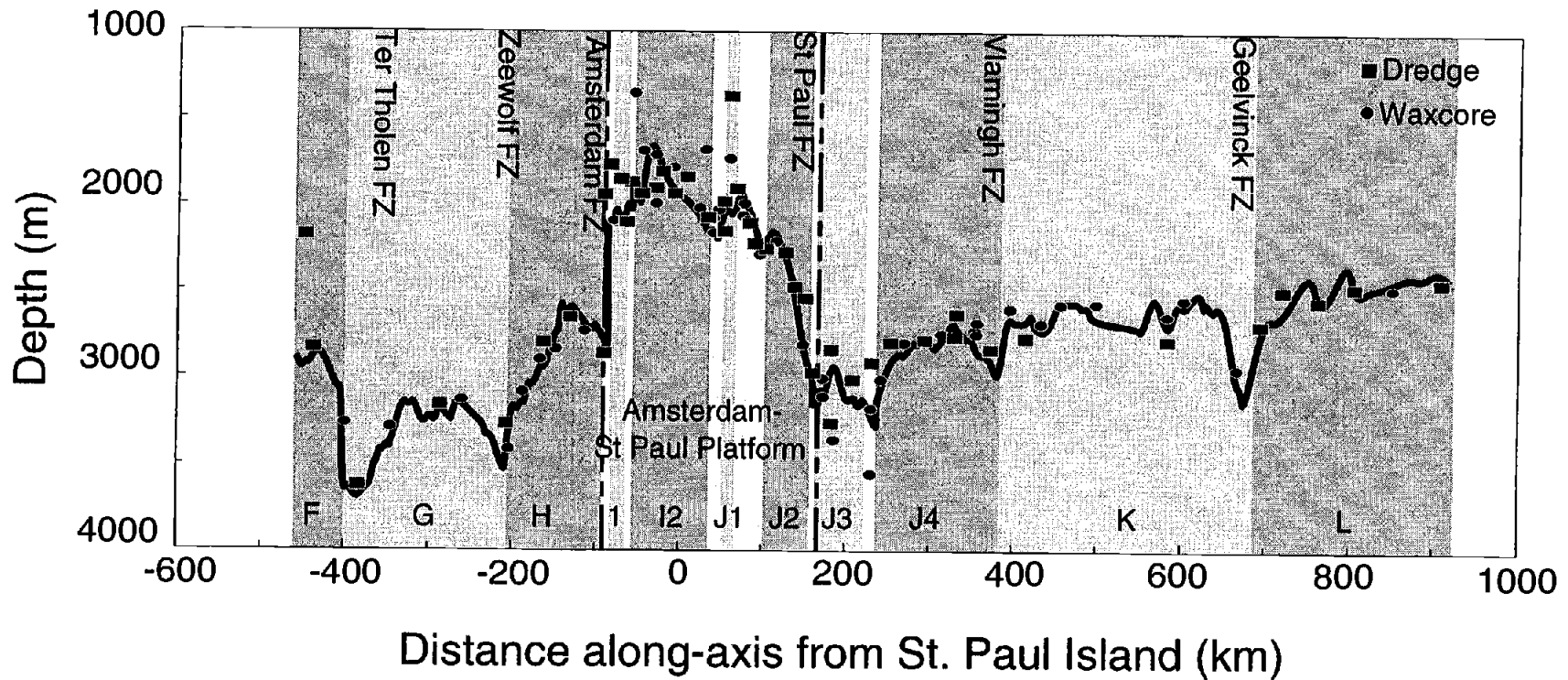


Figure 3: Distribution of sampling stations as a function of distance along-axis and depth. Alternating shades of gray indicate segmentation of the ridge. Segment designations are given at the base of the box and are from Royer and Schlich (1988), and fracture zones are labeled at the top of the box. The delineated area is the ASP platform. Dredge sites are indicated by squares and waxcores by circles. The sites lying significantly above the depth profile are off-axis and include a caldera and lava field atop the platform and a seamount on segment F.

Methods

Sampling Methods

During the Boomerang 06 expedition, samples were collected at 89 sites from a total of 99 deployments (48 dredges and 51 wax cores) (Figure 3 and Table 1).

Sampling efforts were concentrated on the ASP platform, where the average spacing was approximately 10 km between stations. Away from the platform stations had an average spacing of 14 km.

Once on board the ship, samples from each locality were washed in fresh water and then sorted into groups based on hand specimen characteristics, including lava flow morphology, crystallinity, mineralogy (e.g. presence or absence of olivine, plagioclase or clinopyroxene), and extent of weathering or alteration. Representative samples of each of the groups were assigned numbers. Glass was removed from these samples where present, and small chips were mounted in circular epoxy disks for electron microprobe analysis.

To increase the success rate of the wax core deployments, multiple (2 - 3) hits were made on the ocean bottom. After the bottom was initially impacted, the wax core was raised to 100 m off-bottom, allowed to stabilize, and then lowered again. In most cases three lowerings were made. This method of sampling increased sample recovery, but it also raised the possibility that more than one lava flow might be sampled, as the wax core might not land in exactly the same spot each time. To monitor any possible sample heterogeneity introduced by these methods, three glass chips, rather than one were selected from each wax core, and mounted for electron microprobe analysis.

Table 1: Sampling sites. Sampling was done during the Boomerang 06 expedition on the R/V Melville, in early 1996. Site locations were determined using satellite-navigated GPS and SeaBeam maps. The depth is the average of the on- and off-bottom depths. A segment designation of platform indicates a platform edifice or an off-axis lava field. A positive number in the distance column indicates sites to the southeast of St. Paul Island, and a negative number indicates sites to the northwest. The chemical group listing indicates which of the 126 chemical groups (shown in Table 2) is associated with a particular site.

Site	Segment	Latitude (°S)	Longitude (°E)	Depth (m)	Distance from St. Paul Island (km)	Chemical Groups
D33	L	42° 06.9'	88° 02.5'	2450	910	1
WC3	L	41° 46.2'	87° 31.5'	2485	853	2,3
D34	L	41° 31.0'	87° 05.6'	2480	807	4,5
D35	L	41° 19.3'	86° 37.9'	2560	764	6
D36	L	41° 05.9'	86° 13.8'	2500	722	7,8,9
D37	L/K	41° 00.4'	85° 55.5'	2700	696	10,11,12
WC4	K	42° 51.8'	83° 17.4'	2953	668	13
WC7	K	42° 21.1'	82° 33.1'	2645	585	14
D38	K	42° 21.2'	82° 33.7'	2790	586	15,16
WC8	K	41° 48.1'	82° 50.3'	2575	501	17,18
WC9	K	41° 32.0'	81° 28.3'	2579	458	19
WC10	K	41° 22.5'	81° 17.5'	2690	435	20
D39	K	41° 14.6'	81° 09.4'	2776	416	21,22
WC11	K	41° 06.9'	81° 00.3'	2605	398	23,24
D40	J4	41° 40.3'	79° 09.6'	2766	332	25,26
D41	J4	41° 46.3'	79° 45.2'	2840	375	27,28,29,30
WC12	J4	41° 39.1'	79° 34.3'	2730	355	31,32
WC14	J4	41° 44.9'	79° 29.4'	2753	358	33
D42	J4	41° 31.6'	79° 23.2'	2635	334	34
WC15	J4	41° 23.8'	79° 15.1'	2750	316	35
D43	J4	41° 15.1'	79° 06.3'	2785	296	36,37,38
WC16	J4	41° 04.9'	78° 54.8'	2800	272	39
D44	J4	40° 58.2'	78° 47.3'	2810	255	40

Table 1 continued.

Site	Segment	Latitude (°S)	Longitude (°E)	Depth (m)	Distance from St. Paul Island (km)	Chemical Groups
WC17	J4	40° 52.7'	78° 42.2'	3013	243	41
WC18	J4	40° 48.6'	78° 36.1'	3182	232	42
WC19	J3	40° 52.6'	78° 30.6'	3555	232	43,44
D46	J3	40° 45.1'	78° 19.5'	3014	210	45
WC20	J3	40° 37.7'	78° 13.2'	3130	194	46
D47	J3	40° 33.2'	78° 08.5'	2845	184	47
D48	J2	39° 48.7'	78° 23.7'	2479	140	48
D49	J2	39° 49.3'	78° 35.8'	2543	152	49,50
WC21	J2	39° 53.7'	78° 28.6'	2815	151	51
D50	J2	39° 58.9'	78° 33.0'	2973	162	52,53
WC23	J2	40° 05.3'	78° 35.7'	3007	174	54
D51	J2	40° 12.7'	78° 37.7'	3264	185	55
D52	J2	39° 44.3'	78° 18.5'	2278	128	56,57,58
WC25	J2	39° 39.1'	78° 14.5'	2211	118	59
D53	J2	39° 32.6'	78° 10.9'	2256	105	60
D54	J2	39° 27.0'	78° 05.5'	2225	91	61,62
WC29	J2	39° 19.4'	77° 59.6'	2060	82	63,64
D58	J1/J2	39° 12.8'	77° 53.0'	1370	61	119,120
WC26	J1	39° 25.2'	78° 13.3'	2289	98	65
D55	J1	39° 17.3'	78° 11.1'	2104	85	66,67
WC30	J1	39° 12.5'	78° 10.6'	1990	78	68
D59	J1	39° 07.4'	78° 08.6'	1903	70	69
WC31	J1	39° 01.1'	78° 08.3'	1730	61	70
D60	J1	38° 57.6'	78° 06.4'	1978	54	71,72,73
D61	J1	38° 56.8'	78° 08.1'	2153	55	74
WC32	J1	38° 54.0'	78° 04.5'	2026	48	75,76,77
WC33	J1	38° 50.2'	78° 03.2'	2080	41	78
WC35	I2	38° 26.0'	78° 35.3'	2163	41	79

Table 1 continued.

Site	Segment	Latitude (°S)	Longitude (°E)	Depth (m)	Distance from St. Paul Island (km)	Chemical Groups
D62	I2	38° 23.3'	78° 32.1'	2072	35	80
WC36	I2	38° 18.3'	78° 28.9'	2018	25	81
D63	I2	38° 11.9'	78° 22.0'	1838	9	82
WC37	I2	38° 05.4'	78° 15.2'	1780	-6	83
D64	I2	37° 58.9'	78° 09.8'	1805	-20	84,85
WC38	I2	37° 51.6'	78° 11.3'	1709	-28	86
D65	I2	37° 55.7'	78° 06.2'	1902	-28	87
WC39	I2	37° 58.1'	78° 03.9'	1990	-27	88
D66	I2	37° 48.1'	77° 59.5'	1935	-45	89
D67	I2	37° 34.7'	78° 05.5'	1865	-56	90
D68	I2	37° 25.6'	77° 52.2'	1766	-82	91
WC42	I2	37° 26.0'	77° 59.0'	2104	-75	92
D70	I1	37° 09.9'	78° 24.0'	1850	-70	93
WC43	I1	37° 07.2'	78° 19.5'	2092	-78	94,95
D71	I1	37° 03.3'	78° 14.4'	1940	-89	96,97
D72	H	36° 20.6'	79° 07.4'	2865	-89	98
WC46	H	36° 10.9'	78° 57.2'	2734	-112	99
D73	H	36° 04.0'	78° 49.5'	2659	-129	100, 101, 102
WC47	H	35° 56.3'	78° 42.5'	2840	-147	103, 104
D74	H	35° 50.2'	78° 36.7'	2800	-161	105, 106
WC48	H	35° 47.8'	78° 35.7'	2900	-165	107
WC49	H	35° 38.5'	78° 27.8'	3086	-186	108
WC50	H	35° 31.7'	78° 21.2'	3413	-202	109
D75	H/G	35° 17.0'	78° 35.7'	3269	-205	122, 123
D78	G	33° 54.3'	77° 32.1'	3624	-381	110
WC52	G	34° 09.3'	77° 49.4'	3290	-343	111
D79	G	34° 34.2'	78° 14.2'	3163	-284	112
WC53	G	34° 43.4'	78° 26.9'	3135	-258	113

Table 1 continued.

Site	Segment	Latitude (°S)	Longitude (°E)	Depth (m)	Distance from St. Paul Island (km)	Chemical Groups
D76	F	32° 45.8'	77° 53.2'	2178	-447	114, 115
D77	F	32° 56.7'	77° 48.9'	2835	-435	116
WC51	F	33° 10.0'	78° 09.0'	3266	-398	117
St. Paul Is.	platform	38° 42.6'	77° 33.0'	-	-	118
WC34	platform	38° 46.9'	77° 57.8'	1678	31	121
WC44	platform	37° 43.3'	77° 49.5'	875	-62	124
WC45	platform	37° 43.0'	77° 49.9'	647	-62	125, 126

Analytical Methods

Major elements

The major and minor elements of the basalt glasses were analyzed with Oregon State University's CAMECA SX-50 electron microprobe. Operating conditions consisted of an acceleration voltage of 15 kV and a beam current of 30 nA. A 10 μm -diameter defocused beam was utilized to limit Na-loss. Counting times were 10 seconds for Na, Ca, and Mn, 20 seconds for Mg, Al, Si, Ti, and Fe, 30 seconds for P and K, and 60 seconds for Cr. Na was analyzed first due to its susceptibility to beam damage (Nielsen et al., 1995). The natural basalt glass standard VG-A99 (USNM 113498) from Makaopuhi Lava Lake, Hawaii (Jarosewich, 1980) was included in all runs. In addition, an Indian Ocean basalt glass (USNM 113716) (Jarosewich, 1980), was analyzed concurrently to monitor the consistency between analyses on different days.

Three-point lines were set on each glass chip with a spacing of 40-60 μm between each point. In the case that using a transect wasn't possible, due to the presence of cracks or incipient crystals visible in back scatter images, three separate points were set with a spacing close to 40-60 μm . Analyses with totals < 98% or > 101%, or analyses with individual oxides outside the margin of error as determined by counting statistics were removed from the data set. After this screening, the three points from an individual sample were averaged together. A total of 312 glass samples were analyzed, and were divided into 126 chemical groups (Table 2, see Appendix 1 for the unaveraged data). To qualify as a chemical group, samples had to be both from the same sampling site as well as have the same major element composition within analytical error. The resulting chemical group composition was determined by averaging the compositions of such individual samples.

Table 2: Glass analyses. All analyses done with Oregon State University's electron microprobe. FeO* = total Fe as FeO. Typical standard deviations, based on the average of 50 standard deviations randomly selected from the data set are SiO₂ (0.12), TiO₂ (0.02), Al₂O₃ (0.06), FeO* (0.09), MnO (0.02), MgO (0.05), CaO (0.07), Na₂O (0.04), K₂O (0.01), P₂O₅ (0.02), and Cr₂O₃ (0.01). n = number of analyzed samples in each group. The phenocryst column lists those phenocrysts present in hand sample. Pl is for plagioclase, Ol is for olivine and Cpx is for clinopyroxene.

Chemical Group	Segment	Samples	n=	SiO ₂	TiO ₂	Al ₂ O ₃	FeO*	MnO	MgO	CaO	Na ₂ O	K ₂ O	P ₂ O ₅	Cr ₂ O ₃	Total	Phenocrysts
<i>On-axis samples</i>																
	L	d33:1,2,3	9	50.50	1.56	15.16	9.44	0.14	7.90	11.98	2.65	0.14	0.15	0.04	99.66	Pl-Ol
1	L	w3a	3	50.76	1.55	15.11	9.73	0.15	7.06	12.55	2.56	0.15	0.13	0.05	99.78	
2	L	w3b	3	50.23	1.49	14.80	9.67	0.16	7.89	12.34	2.48	0.15	0.12	0.06	99.38	
3	L	d34:1,2,3	9	51.09	1.91	13.93	11.08	0.20	6.70	10.86	2.96	0.20	0.18	0.01	99.12	Pl
4	L	d34-4	3	51.29	1.66	14.24	10.31	0.16	7.27	11.36	2.70	0.12	0.16	0.02	99.30	Pl
5	L	d35:1-4,8,9	22	51.16	1.60	14.31	10.04	0.16	7.30	11.64	2.66	0.18	0.15	0.03	99.23	Pl
6	L	d36-1	3	50.63	1.82	14.72	10.25	0.16	7.29	10.84	2.69	0.16	0.20	0.05	98.80	
7	L	d36-2	3	50.54	1.89	14.74	10.60	0.17	7.37	11.34	2.83	0.17	0.17	0.04	99.85	
8	L	d36-4	3	51.19	1.58	14.24	10.14	0.16	7.30	11.49	2.62	0.18	0.15	0.03	99.08	
9	K	w4a,b,c	9	51.10	1.48	14.90	9.55	0.16	7.79	11.33	2.49	0.09	0.14	0.05	99.09	
13	K	w7a,b,c	9	51.04	1.37	14.95	9.15	0.15	7.82	11.80	2.56	0.11	0.12	0.05	99.12	
14	K	d38-brlp a,b	6	51.03	1.34	14.98	9.12	0.16	7.93	11.77	2.56	0.10	0.13	0.05	99.18	Pl
15	K	d38-brlp c	3	51.10	1.34	15.12	9.21	0.15	7.99	12.22	2.53	0.09	0.11	0.06	99.93	Pl
16	K	w8a,b	6	50.47	1.55	14.68	10.73	0.17	7.39	11.43	2.70	0.12	0.13	0.04	99.42	
17	K	w8c,d	6	51.08	1.60	14.80	9.96	0.15	7.45	11.81	2.53	0.14	0.14	0.05	99.72	
18	K	w9a,b,c	9	50.80	1.38	14.88	9.87	0.19	7.86	12.04	2.47	0.09	0.11	0.05	99.73	Pl
19	K	w10a,b,c	9	50.56	1.52	14.64	10.31	0.18	7.45	11.89	2.40	0.14	0.13	0.05	99.27	Pl
20	K	d39:1,3	6	51.04	1.21	15.27	8.99	0.16	8.17	12.43	2.24	0.11	0.10	0.05	99.76	Pl-Ol
21	K	d39-2	3	50.13	1.41	15.10	10.20	0.20	7.77	11.89	2.32	0.08	0.11	0.04	99.25	Pl-Ol
22	K	w11a,c	6	50.99	1.79	14.31	10.83	0.20	7.03	11.39	2.46	0.14	0.16	0.04	99.34	Pl
23	K	w11b	2	50.07	1.79	14.22	10.15	0.17	7.33	11.41	2.57	0.15	0.16	0.05	98.07	Pl
24	J4	d41-1	3	50.34	1.24	15.11	9.14	0.14	8.03	12.08	2.49	0.09	0.10	0.03	98.80	Pl
27	J4	d41-2	3	49.72	1.38	15.23	9.13	0.13	8.11	11.98	2.81	0.07	0.09	0.05	98.68	Pl

Table 2 continued.

Chemical Group	Segment	Samples	n=	SiO ₂	TiO ₂	Al ₂ O ₃	FeO*	MnO	MgO	CaO	Na ₂ O	K ₂ O	P ₂ O ₅	Cr ₂ O ₃	Total	Phenocrysts
	J4	d41:3,4	6	49.96	1.32	15.46	9.54	0.16	7.83	12.07	2.66	0.07	0.11	0.05	99.23	PI
	J4	d41-5	3	50.78	1.53	14.81	10.18	0.18	7.45	11.73	2.62	0.10	0.15	0.04	99.58	
	J4	w12a,b	6	50.46	1.06	14.96	9.51	0.16	8.37	12.46	2.09	0.05	0.09	0.04	99.25	
	J4	w12c	3	50.49	1.31	14.49	9.88	0.14	7.48	12.22	2.43	0.09	0.14	0.05	98.72	
	J4	d42-1,2	6	50.73	1.58	14.48	10.35	0.20	7.21	11.83	2.55	0.10	0.13	0.04	99.20	PI
	J4	w15a,b,c	9	50.91	1.51	14.39	10.35	0.18	7.60	11.85	2.42	0.07	0.12	0.04	99.43	
	J4	d43:1-3	9	50.58	1.37	15.56	9.14	0.15	8.36	11.99	2.59	0.06	0.12	0.05	99.97	PI
	J4	d43-4	3	50.85	1.27	15.35	9.34	0.17	8.47	12.07	2.44	0.06	0.11	0.04	100.18	PI
	J4	d43-6	3	50.86	1.52	15.00	9.83	0.19	8.04	11.87	2.46	0.06	0.13	0.03	99.98	PI
	J4	w16a,b	6	51.35	1.60	14.59	10.01	0.19	7.69	11.89	2.51	0.07	0.14	0.04	100.08	
	J4	d44:1-6	18	50.71	1.42	14.43	10.19	0.18	7.65	12.17	2.54	0.10	0.12	0.05	99.57	PI
	J4	w17a-c	9	51.24	1.58	14.27	10.41	0.17	7.61	11.76	2.36	0.07	0.13	0.03	99.62	
	J4	w18a-c	9	51.07	1.37	14.47	9.74	0.16	7.94	12.35	2.32	0.06	0.10	0.05	99.62	PI
	J3	w19a	3	51.14	1.34	14.50	9.67	0.18	7.96	12.31	2.31	0.06	0.12	0.05	99.66	PI
	J3	w19b-c	6	50.42	1.19	15.08	9.62	0.15	8.16	12.12	2.19	0.09	0.09	0.04	99.16	PI
	J3	d46:1,2	6	51.73	1.06	14.69	9.11	0.16	8.18	12.62	2.12	0.06	0.08	0.05	99.87	PI-OI
	J3	w20a-c	9	50.46	1.13	15.39	9.64	0.15	8.19	12.03	2.24	0.08	0.09	0.05	99.42	
	J3	d47:1-6	18	50.29	1.12	15.48	9.16	0.15	8.41	12.44	2.35	0.13	0.10	0.05	99.67	PI
	J2	d48:1-4	12	49.82	1.26	15.87	9.87	0.16	8.30	11.54	2.38	0.15	0.11	0.04	99.49	PI-OI
	J2	w21a-c	9	50.97	1.69	14.20	10.94	0.21	6.76	11.14	2.58	0.26	0.18	0.04	98.97	PI
	J2	d50-brlp a,c	6	51.10	1.55	14.90	10.28	0.16	7.52	11.35	2.50	0.27	0.16	0.04	99.84	
	J2	d50-brlp b	3	51.46	1.65	14.79	10.74	0.19	7.13	11.33	2.63	0.30	0.16	0.03	100.43	
	J2	w23a-c	15	50.99	1.23	14.79	9.58	0.17	7.77	12.25	2.39	0.16	0.13	0.06	99.52	PI
	J2	d51:1,a-c	12	51.35	1.77	14.10	11.08	0.19	6.48	10.87	2.65	0.30	0.18	0.02	98.99	PI-OI
	J2	d52-brlp a	3	50.44	0.97	15.32	8.87	0.14	8.86	12.85	2.09	0.14	0.10	0.05	99.83	PI
	J2	d52-brlp b	3	50.29	1.11	15.52	9.60	0.17	8.56	12.20	2.18	0.17	0.11	0.02	99.94	PI
	J2	w25a-c	9	50.80	2.06	14.65	10.91	0.18	6.12	10.34	2.89	0.50	0.23	0.04	98.72	
	J2	d52-brlp c	3	50.39	1.17	15.08	9.64	0.17	8.27	12.04	2.39	0.15	0.12	0.03	99.46	PI

Table 2 continued.

Chemical Group	Segment	Samples	n=	SiO ₂	TiO ₂	Al ₂ O ₃	FeO*	MnO	MgO	CaO	Na ₂ O	K ₂ O	P ₂ O ₅	Cr ₂ O ₃	Total	Phenocrysts
60	J2	d53-1	5	51.42	1.81	14.26	11.25	0.19	6.65	11.18	2.73	0.33	0.18	0.03	100.04	PI
61	J2	d54:1,4	6	51.09	1.96	13.68	12.39	0.19	5.99	10.27	2.82	0.30	0.18	0.01	98.88	
62	J2	d54:2,3,5,6	12	51.30	1.79	14.42	10.85	0.17	6.44	10.79	2.72	0.34	0.19	0.01	99.03	
63	J2	w29a	3	51.07	2.18	13.66	12.39	0.22	5.72	10.20	2.76	0.38	0.25	0.03	98.85	
64	J2	w29b,c	5	51.24	2.28	13.44	12.76	0.20	5.52	9.84	2.80	0.39	0.24	0.02	98.73	
65	J1	w26a-c	9	51.55	1.70	14.52	10.41	0.19	6.84	10.86	2.71	0.30	0.17	0.04	99.28	PI
66	J1	d55-1	3	51.27	1.38	14.74	9.69	0.17	7.46	11.75	2.49	0.28	0.13	0.04	99.40	PI-OI
67	J1	d55-2	3	51.31	1.80	14.18	10.90	0.18	6.52	10.78	2.69	0.35	0.20	0.02	98.93	PI-OI
68	J1	w30a-c	9	51.13	1.77	14.47	10.37	0.17	6.78	11.18	2.65	0.37	0.20	0.02	99.12	PI
69	J1	d59:1-7	21	51.15	1.71	14.82	9.97	0.17	7.11	11.53	2.55	0.41	0.20	0.04	99.65	PI
70	J1	w31a-c	9	50.90	1.91	14.69	10.71	0.19	6.59	10.81	2.76	0.43	0.22	0.02	99.23	
71	J1	d60-1	3	51.14	1.36	15.03	10.06	0.16	7.50	11.84	2.42	0.26	0.13	0.03	99.94	PI
72	J1	d60-2	3	51.19	1.35	15.30	9.90	0.18	6.86	11.76	2.48	0.27	0.14	0.03	99.48	PI
73	J1	d60:3,4	6	51.18	1.54	14.47	10.78	0.19	6.72	11.47	2.52	0.29	0.14	0.02	99.34	PI
74	J1	d61:1-4	12	51.38	1.68	14.93	10.27	0.16	7.13	11.22	2.57	0.33	0.19	0.04	99.88	PI-OI
75	J1	w32a	3	50.89	1.47	15.09	10.06	0.20	8.04	10.91	2.49	0.27	0.17	0.04	99.63	
76	J1	w32b,d,e	9	51.28	1.51	15.19	10.36	0.17	7.69	11.08	2.60	0.28	0.16	0.04	100.36	
77	J1	w32c	2	51.04	1.52	15.31	10.21	0.15	7.38	11.21	2.60	0.27	0.16	0.04	99.89	
78	J1	w33a-c	9	50.58	1.76	14.99	11.31	0.19	6.95	10.69	2.68	0.29	0.17	0.03	99.64	
79	I2	w35a-c	9	51.34	1.62	14.30	10.69	0.17	6.76	11.19	2.47	0.38	0.20	0.02	99.15	
80	I2	d62-brlp a,b	6	51.69	1.99	14.09	11.33	0.18	5.87	10.28	2.60	0.58	0.26	0.01	98.89	
81	I2	w36a-c	9	51.32	2.04	14.27	10.98	0.18	6.07	10.52	2.67	0.59	0.27	0.02	98.92	
82	I2	d63:1-5	15	51.15	1.65	14.61	10.29	0.16	6.99	11.48	2.38	0.42	0.20	0.02	99.36	
83	I2	w37a-c	9	51.88	1.84	14.52	10.63	0.17	6.14	10.62	2.64	0.55	0.22	0.03	99.24	
84	I2	d64:1,3,6-10	21	51.78	1.84	14.74	10.30	0.17	6.08	10.61	2.66	0.65	0.25	0.01	99.09	
85	I2	d64:2,4,5,11	12	53.43	1.88	14.54	10.54	0.17	5.06	9.25	2.95	0.81	0.30	0.01	98.95	
86	I2	w38a-c	9	50.40	1.51	14.80	9.92	0.17	7.55	12.02	2.35	0.28	0.16	0.04	99.21	PI
87	I2	d65-brlp a-c	8	52.16	2.16	14.16	11.14	0.18	5.11	9.42	2.89	0.76	0.28	0.01	98.27	

Table 2 continued.

Chemical Group	Segment	Samples	n=	SiO ₂	TiO ₂	Al ₂ O ₃	FeO*	MnO	MgO	CaO	Na ₂ O	K ₂ O	P ₂ O ₅	Cr ₂ O ₃	Total	Phenocrysts
89	I2	d66:1-4	12	50.17	1.74	15.14	10.04	0.17	7.23	11.62	2.44	0.41	0.20	0.03	99.19	
90	I2	d67:1-3	9	51.38	2.15	14.48	11.08	0.19	5.93	10.37	2.73	0.52	0.26	0.02	99.13	PI-OI
93	I1	d70:1-5,a	18	50.94	1.28	15.14	9.18	0.16	7.92	12.51	2.17	0.24	0.13	0.04	99.71	PI-OI
94	I1	w43a	3	51.25	1.38	14.90	9.65	0.17	7.68	11.87	2.37	0.24	0.15	0.02	99.68	PI
95	I1	w43b,c	6	51.36	1.40	14.97	9.68	0.17	7.32	11.90	2.39	0.25	0.14	0.03	99.61	PI
96	I1	d71:1,2	6	51.33	1.85	13.87	11.63	0.20	6.06	10.73	2.66	0.30	0.17	0.02	98.80	PI-OI
97	I1	d71:3-5	9	51.27	1.73	14.09	11.32	0.20	6.45	11.02	2.58	0.28	0.18	0.03	99.15	PI-OI
98	H	d72-brlp a-c	9	51.57	1.03	14.56	9.63	0.17	8.03	12.74	2.07	0.06	0.08	0.04	99.98	
99	H	w46a-c	9	50.45	1.07	16.18	8.42	0.16	8.10	12.33	2.38	0.40	0.16	0.05	99.69	PI-OI
100	H	d73:1-3	9	49.93	1.31	15.93	9.46	0.18	7.83	11.63	2.48	0.44	0.18	0.04	99.41	
101	H	d73:4,5	6	50.79	0.76	15.70	8.53	0.16	9.25	13.41	1.75	0.03	0.05	0.07	100.49	
102	H	d73-6	3	50.73	1.02	15.79	8.10	0.17	8.57	12.73	2.15	0.27	0.12	0.05	99.70	
103	H	w47a,b,e,f,g	15	49.53	1.29	16.30	8.59	0.14	7.84	11.95	2.70	0.70	0.19	0.04	99.29	
104	H	w47c,d	6	50.58	1.15	14.76	9.62	0.14	8.45	11.81	2.14	0.23	0.10	0.05	99.03	
105	H	d74-brlp a,c	6	49.92	0.98	16.26	9.45	0.16	8.85	12.34	2.16	0.08	0.06	0.05	100.33	
106	H	d74-brlp b	3	50.57	1.22	16.18	8.57	0.16	8.00	11.80	2.39	0.47	0.15	0.04	99.57	
107	H	w48a-c	9	51.11	0.98	15.40	9.24	0.18	8.39	12.85	2.08	0.14	0.09	0.06	100.51	PI-OI
108	H	w49a,b	6	51.55	1.16	14.80	9.59	0.15	7.96	12.35	2.15	0.21	0.13	0.04	100.09	PI-OI
109	H	w50a-c	9	49.64	1.04	15.38	10.64	0.16	8.72	11.88	1.94	0.10	0.09	0.04	99.64	
122	H/G	d75:1,2,4-6	15	50.04	1.19	15.09	9.49	0.16	8.42	12.69	2.31	0.07	0.12	0.05	99.63	PI
123	H/G	d75-3	3	50.87	1.35	14.42	10.05	0.17	7.97	12.49	2.43	0.04	0.10	0.03	99.91	PI
110	G	d78-brlp a-c	9	51.10	1.32	15.31	9.09	0.16	8.55	11.84	2.46	0.07	0.11	0.04	100.07	
111	G	w52a-c	9	50.98	1.17	15.42	8.67	0.15	8.24	12.39	2.44	0.16	0.12	0.05	99.76	PI
112	G	d79:1a,1b	6	50.87	1.07	14.99	8.92	0.15	8.33	12.80	2.26	0.10	0.10	0.06	99.65	PI
113	G	w53a-c	9	50.96	1.36	14.81	9.42	0.17	7.73	12.27	2.63	0.12	0.12	0.04	99.62	PI
116	F	d77:1-4	12	50.41	1.54	15.43	9.66	0.17	7.95	11.69	2.70	0.14	0.15	0.04	99.87	PI
117	F	w51a-c	9	49.35	1.34	16.26	9.89	0.15	8.26	11.37	2.68	0.14	0.14	0.04	99.62	PI

Table 2 continued.

Chemical Group	Segment	Samples	n=	SiO ₂	TiO ₂	Al ₂ O ₃	FeO*	MnO	MgO	CaO	Na ₂ O	K ₂ O	P ₂ O ₅	Cr ₂ O ₃	Total	Phenocrysts
<i>Off-axis samples</i>																
	L/K	d37-1a,b,c	12	50.65	2.39	13.76	11.34	0.17	6.56	10.49	2.82	0.17	0.26	0.02	98.64	
	L/K	d37-2a,2b	8	50.23	2.23	14.19	11.09	0.18	7.04	10.55	2.69	0.18	0.23	0.03	98.64	
	L/K	d37-3a,3b	6	50.55	1.68	14.33	10.32	0.15	7.52	11.39	2.45	0.12	0.16	0.04	98.71	
	J4	d40:1,2,5	10	50.32	1.24	15.23	8.59	0.18	8.24	12.26	2.71	0.08	0.11	0.05	99.02	
	J4	d40:3,4	6	50.10	1.21	15.39	8.95	0.15	7.91	12.16	2.55	0.08	0.10	0.06	98.67	
	J4	w14a,b,c	9	48.25	1.34	16.96	10.06	0.15	8.77	10.38	3.21	0.04	0.09	0.04	99.28	
	J2	d49-1	3	51.39	1.79	14.06	11.12	0.17	6.31	10.59	2.75	0.30	0.19	0.02	98.69	Pl-OI-Cpx
	J2	d49-3	5	51.89	2.97	12.22	16.22	0.25	3.89	8.17	3.11	0.54	0.34	0.01	99.61	Pl-OI-Cpx
	J1/J2	d58:1-3	11	48.21	1.13	17.25	11.02	0.17	8.89	10.99	2.59	0.06	0.07	0.03	100.41	OI
	J1/J2	d58-4	3	48.49	1.27	16.59	11.31	0.17	8.35	11.23	2.64	0.06	0.06	0.04	100.21	OI
	I2	w39a-c	9	50.59	2.52	13.56	13.08	0.21	4.93	9.46	3.04	0.67	0.30	0.00	98.36	Pl
	I2	d68:1,2,a,b	12	50.95	2.40	14.03	12.53	0.21	5.25	9.81	3.01	0.59	0.26	0.01	99.05	
	I2	w42a-c	8	51.15	2.60	13.70	12.91	0.21	4.84	9.27	3.00	0.60	0.29	0.00	98.56	
	SP Island	SP-1a,5b	6	50.46	3.26	13.35	14.05	0.23	4.47	8.85	3.19	0.98	0.43	0.00	99.26	
	platform	w34a-c	9	51.14	1.87	15.59	10.22	0.15	6.73	9.84	2.94	0.38	0.21	0.03	99.10	
	platform	w44a-c	9	50.92	2.64	13.55	13.16	0.22	4.65	9.29	3.05	0.77	0.31	0.01	98.57	OI
	platform	w45a,b,d,f,h	15	50.66	2.13	14.13	11.81	0.20	5.85	10.56	2.86	0.62	0.25	0.01	99.07	
	platform	w45c,e,g	9	50.80	2.54	13.70	13.23	0.21	4.79	9.33	3.13	0.75	0.30	0.01	98.80	
	F	d76:1-5	15	49.02	1.24	17.10	9.26	0.15	8.25	11.58	2.99	0.18	0.13	0.03	99.93	
	F	d76-6	3	48.95	1.31	16.63	9.76	0.17	7.95	11.61	3.11	0.20	0.14	0.04	99.87	
	I2	md37.d2-3		50.75	1.76	14.19	10.77	0.19	6.65	11.05	2.69	0.34	0.18	0.06	98.64	
	I2	md37.d3-3		51.99	1.63	14.64	10.23	0.15	6.73	10.45	2.78	0.40	0.18	0.04	99.22	

Chlorine and Sulfur

Following establishment of the 126 chemical groups a subset of samples were analyzed for Cl and S using the electron microprobe at Oregon State University. A beam current of 30 nA, an acceleration voltage of 15 kV, and a 40 μm defocused beam were used. Counting times were 10-20 seconds for most major elements, 60 seconds for S, K, P and Cr, and 1000 seconds for Cl. Two points were analyzed on each sample, then averaged together to represent the Cl and S content of one of the 126 chemical groups (Table 3, see Appendix 4 for unaveraged data). The exception to this was in the first run in which 3 points rather than two were analyzed, and the counting times were 20 seconds for S and 500 seconds for Cl. Chalcopyrite and tugtapite, both from Astimex Scientific, were used as sulfur and chlorine standards, respectively. The Cl content of the tugtapite was cross-referenced to a scapolite standard (USNM R6600-1) (Jarosewich, 1980). From the 126 distinct chemical groups, a primitive and an evolved lava (based on MgO content) from each of the 11 segments were chosen for Cl analysis. By analyzing the range of MgO values covered by a sample suite, a liquid line of descent (LLD) can be defined in an attempt to discern whether or not there is excess Cl in the basalt glass relative to other MORB glasses.

Background Cl level was determined by analyzing an augite standard (USNM 122142) from Kakanui, New Zealand (Jarosewich, 1980) several times over the course of a daily run. Because the augite contains no detectable Cl, any measured Cl represents the background level of Cl present during the time of analysis. The average measurement over the four daily runs of this background Cl level was then subtracted from each of the sample analyses. This correction was 15 ppm Cl with a range of 13-19 ppm over the four runs. The exception to this was during the second half of the fourth daily run, in which the Cl background level was significantly higher than normal with an average of 42 ppm. Samples measured during this period were corrected for a

Table 3: Chlorine and sulfur analyses. All analyses done with Oregon State University's electron microprobe. Typical standard deviations are Cl < 500 ppm (7 ppm), Cl > 500 ppm (18 ppm), and S (42 ppm).

Chemical Group	Segment	S (ppm)	Cl (ppm)	K ₂ O/TiO ₂	K wt. %	Cl/K (ppm/ppm)	
<i>On-axis samples</i>							
	1	L	1062	131	0.09	0.12	0.11
	4	L	1362	37	0.11	0.17	0.022
	20	K	1322	89	0.09	0.12	0.076
	21	K	1064	81	0.09	0.09	0.09
	36	J4	1143	8	0.04	0.05	0.02
	40	J4	1192	39	0.07	0.08	0.05
	47	J3	893	41	0.11	0.10	0.039
	48	J2	1004	123	0.12	0.12	0.10
	66	J1	994	71	0.20	0.23	0.031
	68	J1	1214	134	0.21	0.31	0.043
	75	J1	1080	105	0.18	0.22	0.047
	84	I2	1081	685	0.35	0.54	0.13
	85	I2	1257	1214	0.43	0.68	0.18
	86	I2	1185	233	0.19	0.24	0.098
	93	I1	1008	123	0.19	0.20	0.062
	96	I1	1406	179	0.16	0.25	0.073
	97	I1	1339	205	0.16	0.23	0.088
	100	H	943	226	0.33	0.36	0.062
	101	H	852	18	0.03	0.02	0.08
	102	H	902	146	0.27	0.23	0.064
	103	H	929	384	0.54	0.58	0.066
	107	H	1017	74	0.14	0.11	0.065
	112	G	1031	43	0.10	0.09	0.05
	113	G	1112	49	0.09	0.10	0.051
	116	F	1362	69	0.09	0.11	0.061
<i>Off-axis samples</i>							
	49	J2	1256	274	0.17	0.25	0.11
	50	J2	1989	1498	0.18	0.44	0.34
	119	J1/J2	1139	26	0.05	0.05	0.05
	120	J1/J2	1322	25	0.04	0.05	0.05
	124	platform	1267	753	0.29	0.64	0.12
	125	platform	1243	605	0.29	0.51	0.12
	114	F	1062	110	0.15	0.15	0.073
	201	I2	1224	125	0.19	0.28	0.044
	202	I2	1114	190	0.24	0.33	0.057

background level of 42 ppm instead of 15 ppm. In addition to augite, the Cl content of the VG-A99 glass standard was also monitored between runs to track the level of change, if any, in Cl measurement. During the second half of the fourth run, the measured Cl content of VG-A99 increased from 199 ppm in the first part of the run to 226 ppm and 221 ppm in the second portion, consistent with the measured background increase of Cl.

Compositional Variation of the Basalt Glasses

Samples collected on the Boomerang 06 expedition include normal MORB (N-MORB), enriched MORB (E-MORB) and over-enriched MORB (OE-MORB). Glasses are mainly tholeiitic basalts, with two occurrences of basaltic andesite on the ASP platform, and ten FeTi basalt samples ($\text{FeO}^* > 12 \text{ wt. } \%$, $\text{TiO}_2 > 2 \text{ wt. } \%$, Melson, 1976). All of the FeTi basalts are found on the ASP platform, and seven of these are off-axis samples. SiO_2 values are between 48.2 and 53.4 wt. % and MgO values between 3.9 and 9.3 wt. % (Figure 4). In general, lavas from atop the platform are more enriched (e.g., in minor elements such as K_2O and P_2O_5) and more evolved (higher FeO/MgO) than lavas from off the platform. The N-MORB and the majority of the E-MORB data define coherent trends on MgO variation diagrams suggesting that crystal fractionation is the dominant mechanism responsible for the composition of these lavas. In contrast, segments H and I2 are not explainable by crystal fractionation alone.

The majority of higher FeO^* samples have correspondingly high TiO_2 , and are FeTi basalts (Figure 5). Some of these more evolved samples are associated with segment J2 and the propagating rift tip at its southeastern end. Note the trend of segment I2 on the MgO vs. FeO^* diagram. Most of the individual segments follow a trend of increasing FeO^* with decreasing MgO as shown by the arrow. Segment I2 on the other hand, is distinct and displays much more constant FeO^* values with decreasing MgO values, resulting in a flatter trend.

Regional-Scale Variations

MgO and CaO mirror one another's behavior along-axis (Figure 6). Both show a wider range of values adjacent to, and atop the platform. Away from the platform the

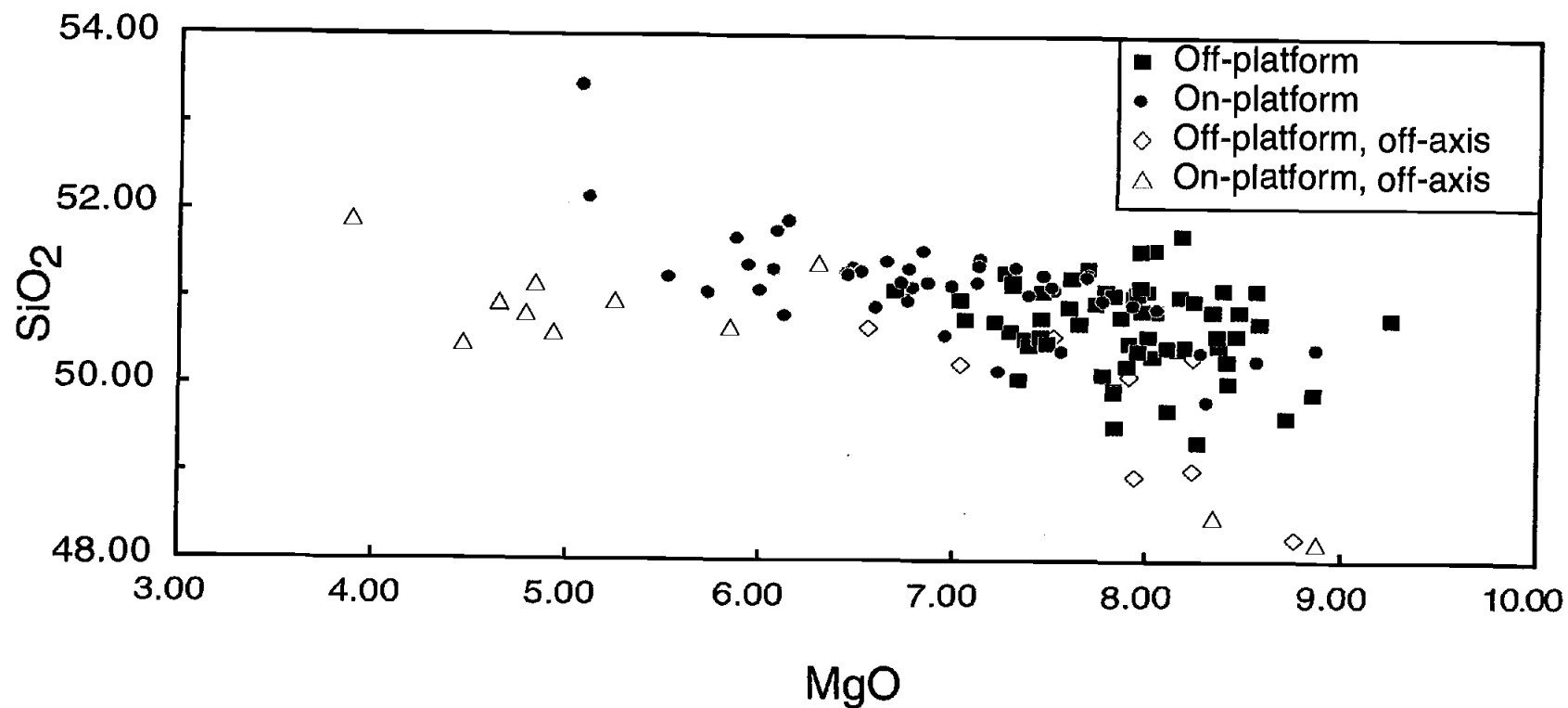


Figure 4: Variation of SiO₂ as a function of MgO. Samples are mainly tholeiitic. Samples located on the ASP platform are shown by filled circles, and samples located on segments away from the platform by filled squares. Off-axis samples on the ASP platform are indicated by unfilled triangles, while those off-axis samples away from the platform are shown by unfilled diamonds.

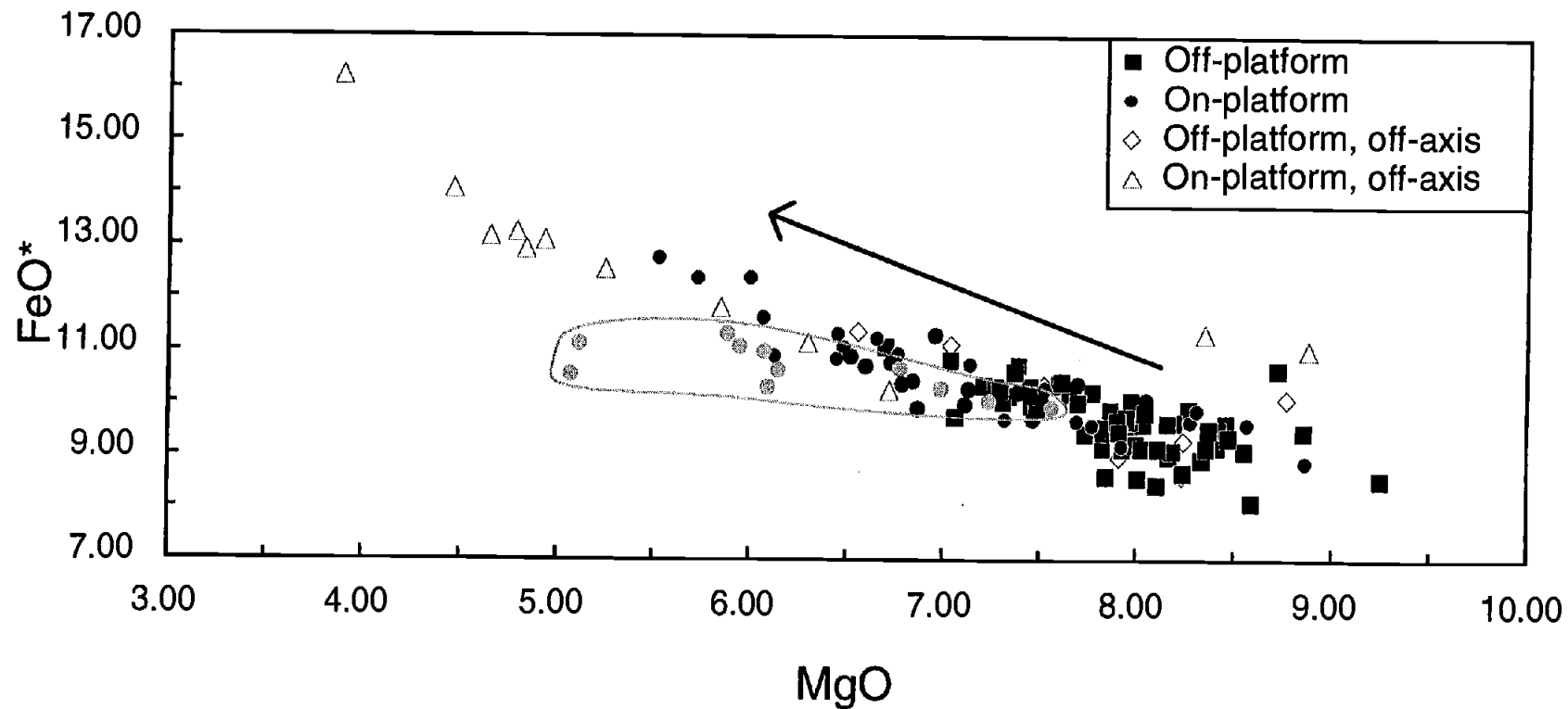


Figure 5: Variation of FeO^* (total Fe as FeO) as a function of MgO . Most of the individual segments follow a trend of increasing FeO^* with decreasing MgO , as shown by the arrow. Segment I2 (circled) however remains at a much more constant FeO^* value with decreasing MgO values.

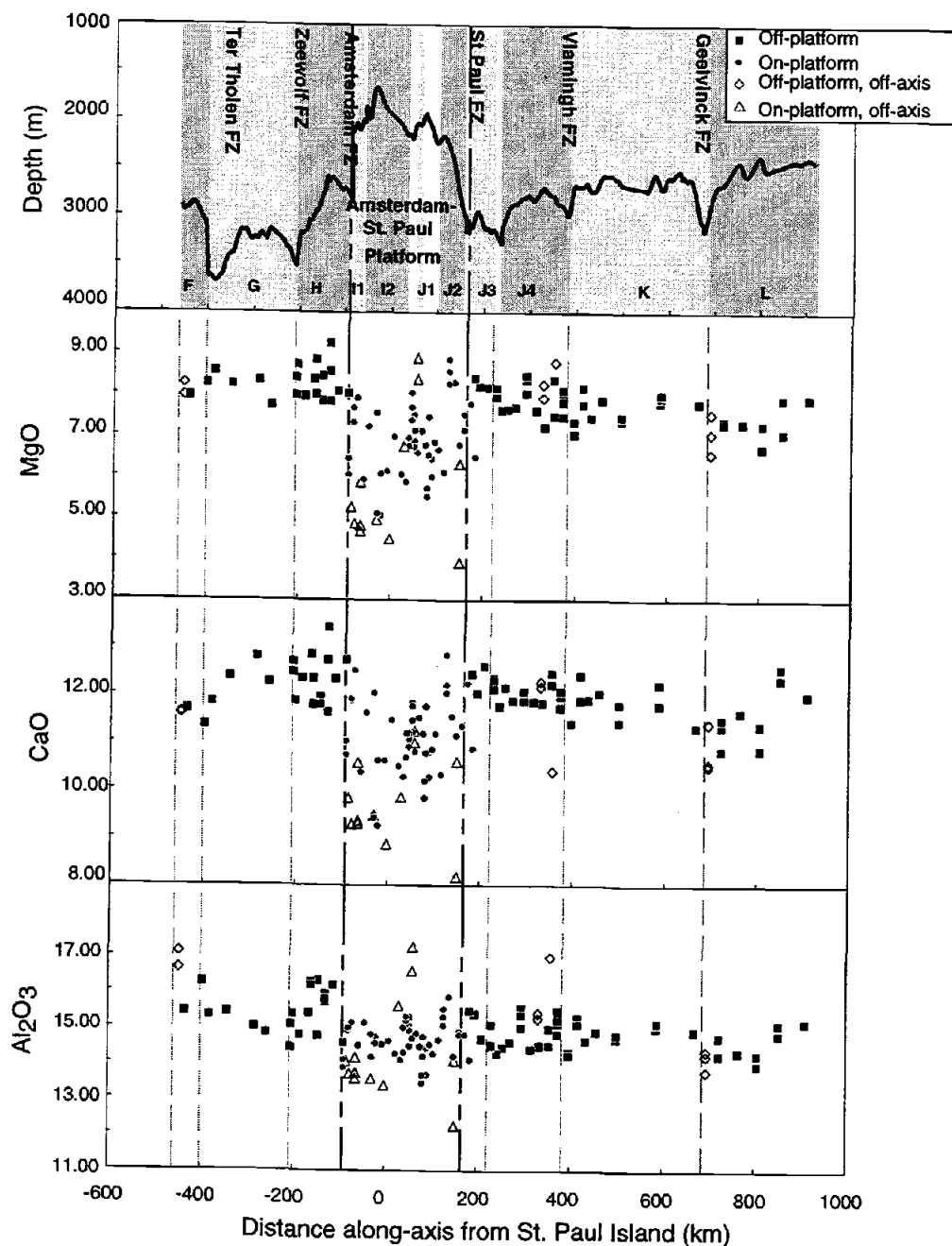


Figure 6: Along-axis chemical variations in the 126 different chemical groups of the study area. The distance along-axis is projected from the pole of rotation and is given relative to St. Paul Island. The alternating shades of gray on the depth profile indicate segmentation of the ridge. The area delineated with alternating dashes is the ASP platform, and the even dashed areas are individual segments. Segment designations given at the base of the depth profile are from Royer and Schlich (1988), and fracture zones are labeled at the top of the profile. On the K_2O/TiO_2 diagram the line shown is a five point running average of the on-axis samples with the shaded envelope representing ± 1 standard deviation.

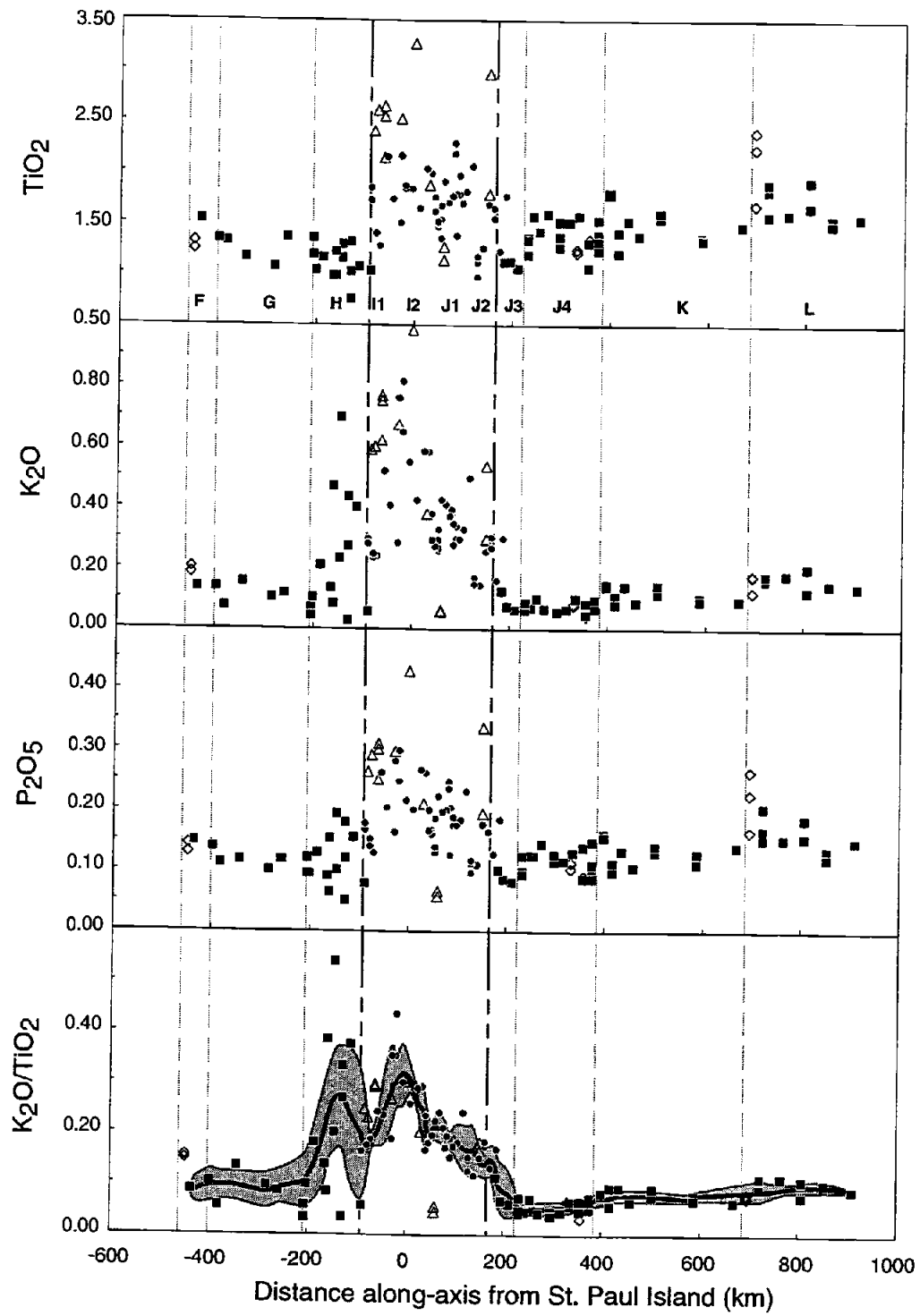


Figure 6 continued.

range in CaO and MgO values diminish, both within and between individual ridge segments. The most primitive compositions, based on MgO content, are found at the margins of the ASP platform; on segment J2 at the southeast end of the platform; and along segment H adjacent to the northwest of the platform. In addition, two equally primitive samples were collected off-axis at the northwest end of segment J2.

A local enrichment of TiO₂ can be seen along-axis atop the platform (Figure 6). Many of the Ti-rich samples were collected off-axis however, there is also a Ti enrichment in the on-axis samples. There are several high TiO₂ (and FeO*) samples between segments L and K, which occur in this locality as volcanic breccia. These latter samples were collected from a ridge which parallels the Geelvinck Fracture Zone, separating segments L and K. Similarly, the sample with the highest TiO₂ on segment J2, as well as a number of other ASP platform samples with high TiO₂, are FeTi basalts. Elevated K₂O concentrations are also observed approaching the ASP platform. This K₂O enrichment extends beyond the platform to include segment H to the northwest. Similarly, P₂O₅ concentrations increase as the platform is approached although the relative enrichment is slightly less than for K₂O. The high P₂O₅ samples between segments L and K are the high FeO* and TiO₂ basalt volcanic breccia noted above.

Segment-Scale Variations

There are systematic variations in TiO₂, K₂O and P₂O₅ with MgO for the data set as whole, but segments also show individual differences, especially for K₂O (Figure 7). The ridge segments southeast of the platform, L, K and J4, form the lower boundary of the K₂O-MgO covariation. Segment H, which is northwest of the ASP platform, trends steeply upwards showing strong K₂O enrichment with only a small decrease in

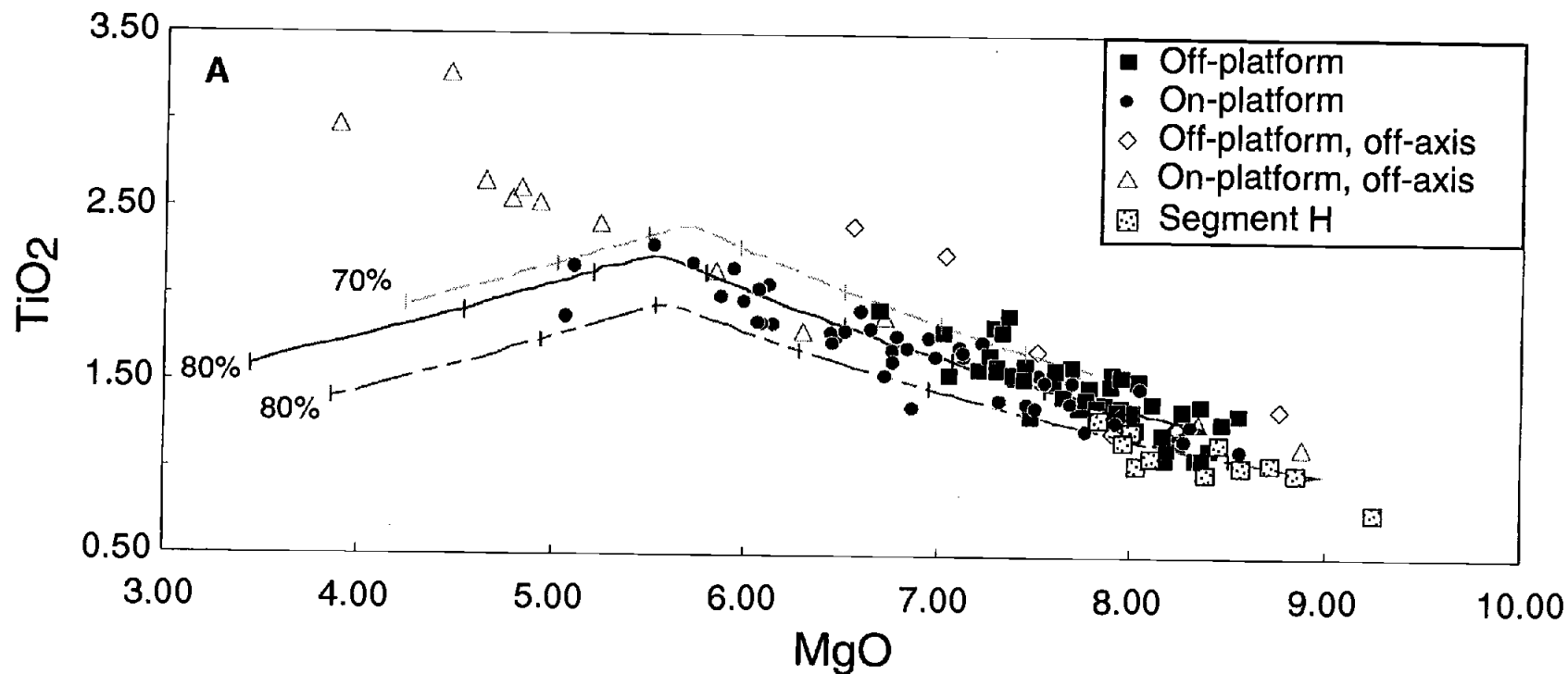


Figure 7: A) TiO_2 , B) K_2O , and C) $\text{K}_2\text{O}/\text{TiO}_2$ as a function of MgO . The lines on the diagrams represent fractional crystallization liquid lines of descent (LLD) at 1-atmosphere and the FMQ buffer (Ariskin et al., 1993). Three starting compositions were used, one composition from segment K (solid line), one composition from segment J2 (even dash line) and one composition from segment J2 (alternating dash line). The segment K and J2 models are for 80% crystallization and the J2 model for 70% crystallization. The tick marks on the LLD are each for 10% crystallization. Symbols as in Figure 4 with one exception; samples from segment H are shown as dotted boxes in A and B.

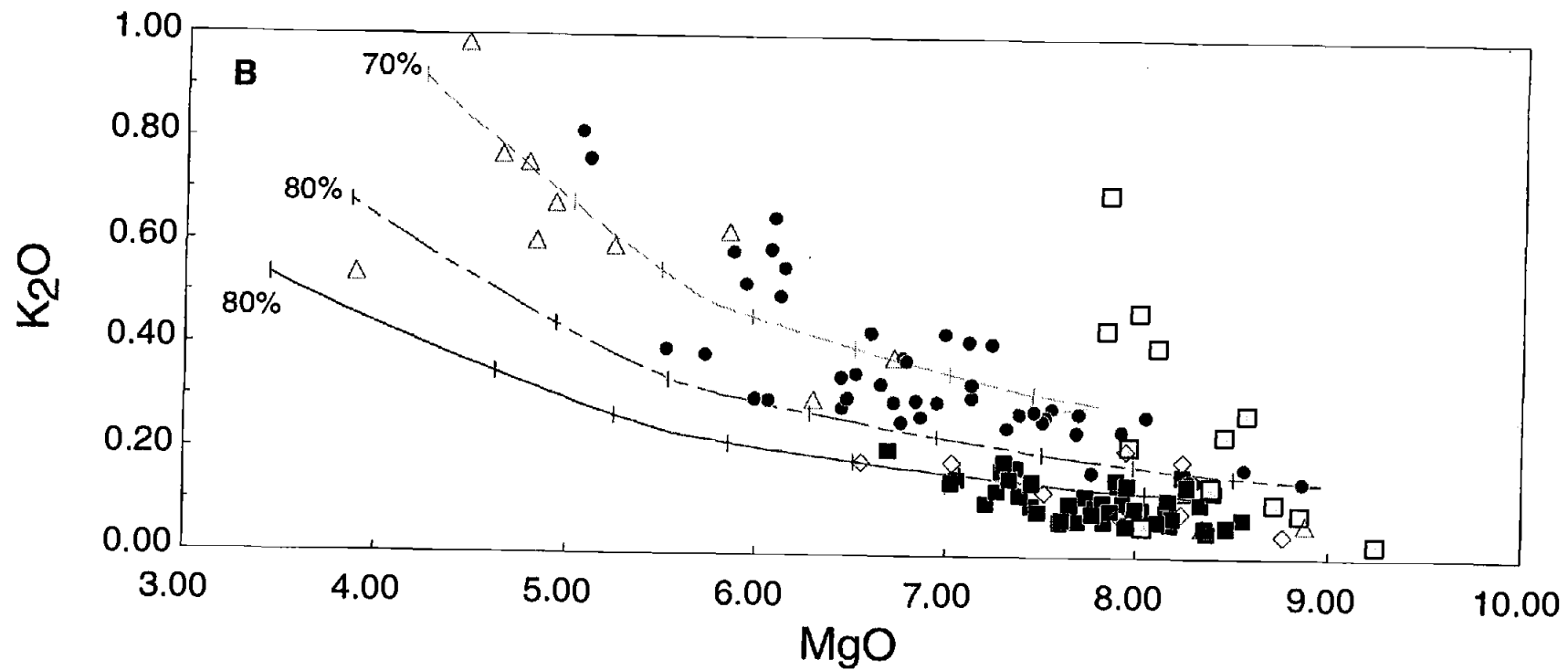


Figure 7 continued.

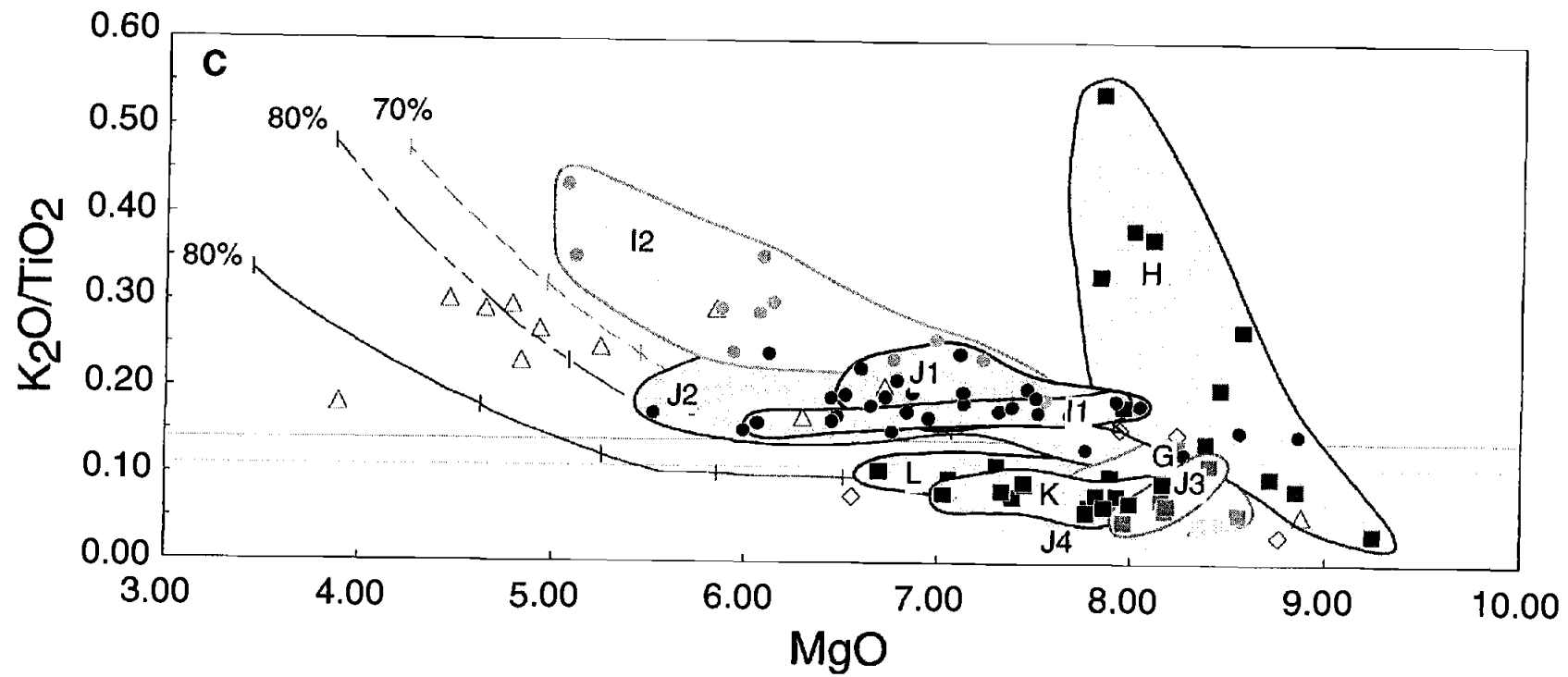


Figure 7 continued.

MgO. The platform lavas show a range of intermediate behavior in their K_2O -MgO relationships, with levels of K_2O enrichment which cannot be easily explained by simple fractional crystallization models, illustrated by the model lines in Figure 7.

Overall three qualitative groupings in K_2O and K_2O/TiO_2 behavior as a function of MgO are evident. These groupings can be attributed mainly to variations in K_2O and not TiO_2 (as seen in Figure 7). Segment H forms one group with a high K_2O/TiO_2 trend; ASP platform lavas form a second group with an intermediate trend and less K_2O/TiO_2 enrichment than H; and lavas from segments more distant from the platform form a third group, with trends resembling the effects of crystal fractionation and little or no K_2O or K_2O/TiO_2 enrichment.

P_2O_5 and TiO_2 both covary with K_2O , but neither of them are highly correlated with K_2O (Figure 8). If P_2O_5 and TiO_2 were perfectly correlated with K_2O the data trends would intersect the origin. Instead the data trends intersect at positive values of both P_2O_5 and TiO_2 , suggesting that P and Ti are slightly more compatible than K when the total sample suite is considered. P and Ti are more similar to one another than to K. Ti appears to behave slightly more compatibly than P for the sample suite overall.

E-MORB and N-MORB in this region can be distinguished using the MgO vs. K_2O/TiO_2 diagram (Figure 7). There is a solid grouping of data beneath a K_2O/TiO_2 value of 0.11, and a solid grouping of data above a K_2O/TiO_2 value of 0.14. Between these two definite groupings lie a few samples which show no clear relation to either the low or the high K_2O/TiO_2 samples. Based on the groupings, a maximum K_2O/TiO_2 value for N-MORB in this region is 0.11, and a minimum K_2O/TiO_2 value for E-MORB is 0.14. Samples falling between $K_2O/TiO_2 = 0.11 - 0.14$ are classified as transitional. Following this reasoning, the majority of basalts from segments J2, J1 and I1 may be classified as E-MORB. Segments G and F are a combination of N-MORB,

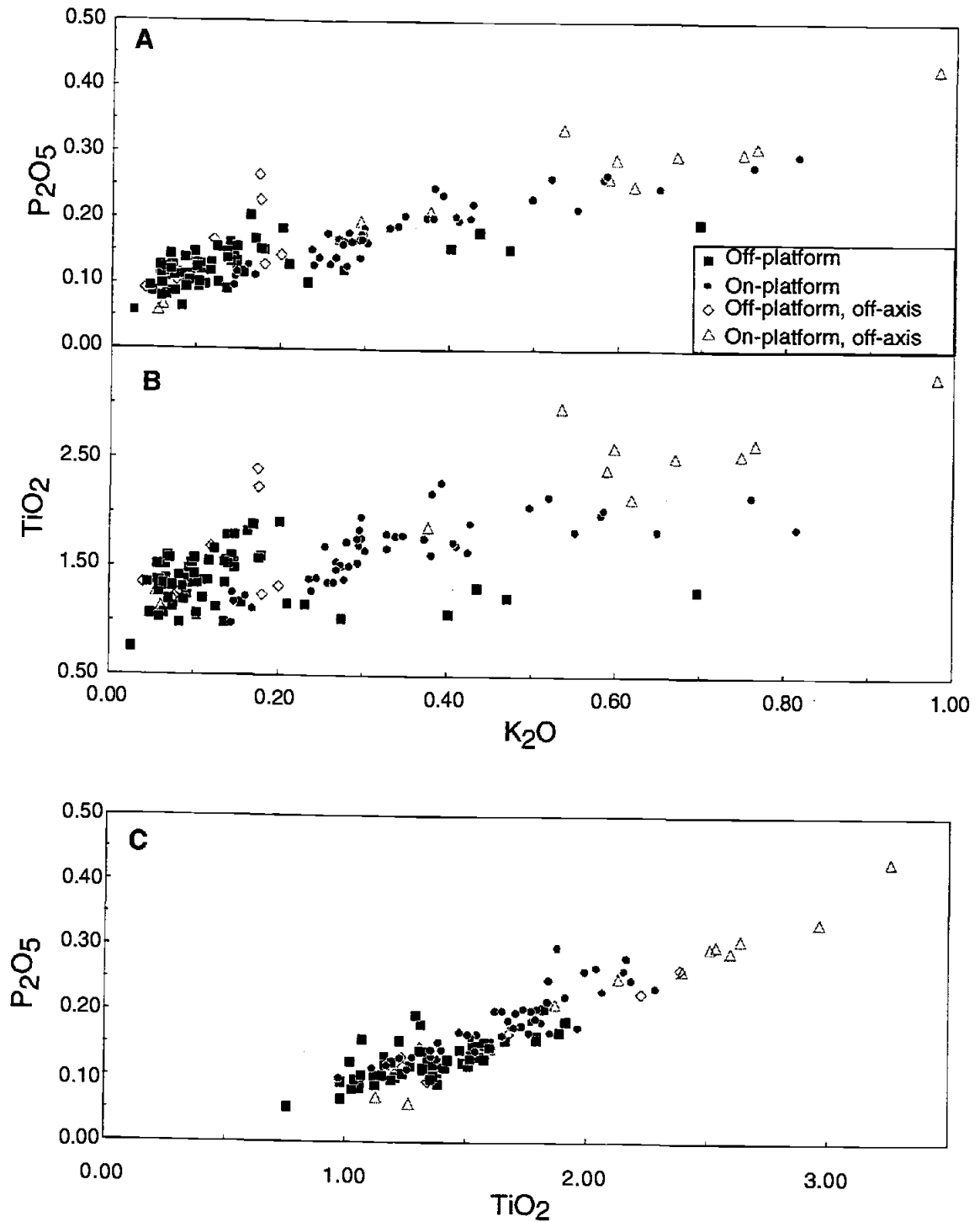


Figure 8: Variations of P_2O_5 , TiO_2 and K_2O . A) P_2O_5 and B) TiO_2 vs. K_2O . C) P_2O_5 vs. TiO_2 .

E-MORB and a few transitional lavas. The remaining ridge segments away from the ASP platform are dominated by N-MORB, with the notable exception of segment H, immediately to the northwest of the platform. The variation of K_2O/TiO_2 values for segment H lavas, from 0.06 - 0.54, requires a separate grouping. Segment H has a near-vertical trend on the MgO vs. K_2O/TiO_2 diagram which cannot be simply described as depleted or enriched, and is referred to here as over-enriched.

Of key importance on the K_2O/TiO_2 vs. TiO_2 and P_2O_5/TiO_2 vs. TiO_2 diagrams of Figure 9 is the direction of the trend displayed by each individual ridge segment. Many of the segments show a horizontal trend, consistent with crystal fractionation. Segment H lavas again show a near-vertical trend. Segment I2 lavas deviate upward from a horizontal trend but to a lesser degree than segment H, suggesting the possibility that both crystal fractionation and some type of an over-enrichment process may be important in determining the composition of these glasses.

Variations in CaO/Al_2O_3 and Fractionation-Corrected Na_2O and FeO^*

Na_2O and FeO^* have been corrected for shallow level crystal fractionation to a value of 8 wt. % MgO following methods similar to those developed by Klein and Langmuir (1987). A second order polynomial fit to the respective oxide variations as a function of MgO was made on a segment by segment basis (see Appendix 6 for fits). This second order polynomial approach simulates the liquid line of descent somewhat better than a linear fit (E. Klein, pers. comm.), especially when MgO is greater than 8 wt. %. The eight values were then calculated using individual polynomial equations for each segment. The segment by segment approach differs from Klein and Langmuir's approach in which a linear fit was made to the global data set as a whole.

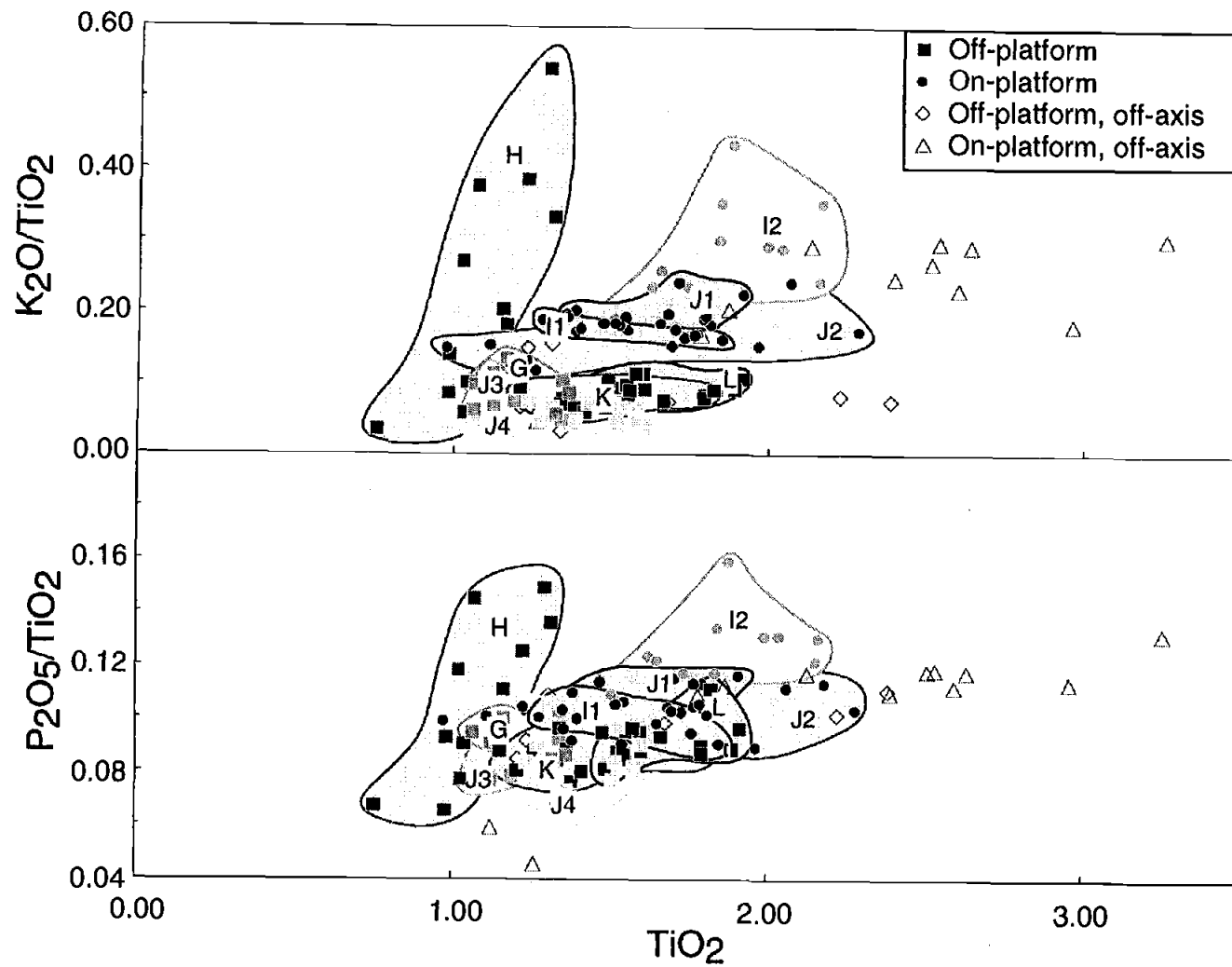


Figure 9: TiO_2 vs. K_2O/TiO_2 and P_2O_5/TiO_2 . Each segment's field has been outlined.

There appears to be a long wavelength decrease in Na_8 towards the ASP platform from both the northwest and southeast, perhaps reflecting larger extents of melting beneath the platform area (Figure 10). Near the edges of the ASP platform and at the I2/J1 offset atop the platform, there are shorter length scale increases in Na_8 . To the northwest of, and atop the ASP platform, the along-axis variations in Na_8 and Fe_8 have similar wavelengths, and Fe_8 shows a positive covariation with Na_8 atop the ASP platform. However, away from the ASP platform to the southeast this similarity disappears, and Na_8 shows a regional increase to the southeast while Fe_8 shows a decrease. Overall, Na_8 and Fe_8 do not correlate with axial depth.

The $\text{CaO}/\text{Al}_2\text{O}_3$ ratio shows both long and short wavelength variations along-axis as well, with a marked decrease atop the ASP platform. Most notably, the $\text{CaO}/\text{Al}_2\text{O}_3$ ratio shows a striking negative covariation with axial depth. The low $\text{CaO}/\text{Al}_2\text{O}_3$ ratios atop the ASP platform, and the positive covariation of Na_8 with Fe_8 in that area qualitatively suggests the possibility of fractionation of high-pressure clinopyroxene beneath the platform region. Sodium behaves as a moderately incompatible element with respect to clinopyroxene, and the $\text{CaO}/\text{Al}_2\text{O}_3$ ratio in clinopyroxene is high. Because clinopyroxene has less FeO^* than the magma from which it crystallizes, clinopyroxene fractionation will increase FeO^* . The end result is that clinopyroxene fractionation will lower the $\text{CaO}/\text{Al}_2\text{O}_3$ ratio, and produce a positive correlation between Na_8 and Fe_8 .

When a segment by segment comparison is made, there are no obviously consistent relationships between Na_8 , Fe_8 or $\text{CaO}/\text{Al}_2\text{O}_3$ ratio. One group of segments, comprised of about one-third of those studied (J4, J2 and I2), increases in Na_8 toward the center of each segment. A different group, also made up of about one-third of the segments (L, J3 and J1), shows an increase in Fe_8 at the northwest end of each segment.

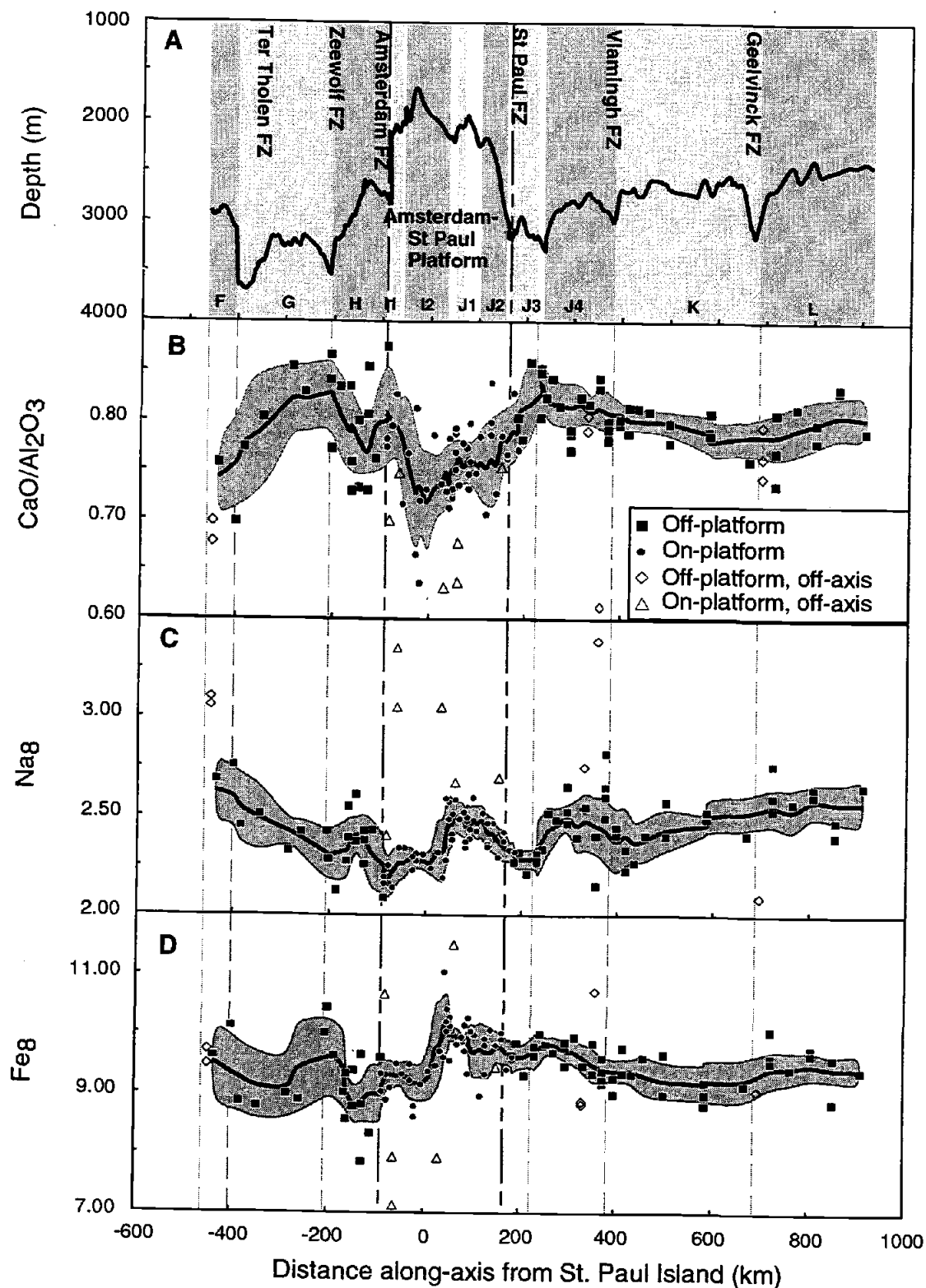


Figure 10: Along-axis variations in fractionation-corrected oxides. A) Along-axis depth profile. B) CaO/Al₂O₃, C) Na₈ and D) Fe₈ vs. along-axis distance. The lines shown on B, C and D are five point running averages of the on-axis samples with the shaded envelope representing ± 1 standard deviation.

Chlorine and Sulfur Variations

Chlorine

Samples were analyzed for chlorine to determine if shallow-level crustal assimilation had occurred, and whether any of the minor element over-enrichment outlined above (i.e. the high K_2O/TiO_2 on segments H and I2) could be explained by assimilation. To determine if a magma has been affected by assimilation, a MgO vs. Cl diagram, with a low pressure fractional crystallization model, allows an initial level of Cl enrichment to be established (Figure 11). This needs to be followed by the examination of a plot of MgO vs. Cl/K (Figure 11). Chlorine has a large ionic radius and a -1 charge that causes it to behave incompatibly during mantle melting and basalt crystallization (Schilling et al., 1980). The fact that the Cl content of a liquid will increase during fractional crystallization makes it necessary to account for the effects of both variable melting and the degree of crystallization when modeling assimilation. This can be accomplished by considering Cl/K (Michael and Cornell, 1998 in press). Because of its relatively higher concentration in MORB, K is much less susceptible to assimilation than Cl and it is easily measured by electron microprobe. The Cl/K ratio should remain approximately constant during crystallization and during mantle melting that exceeds 1%. In contrast the Cl/K ratio will increase with the assimilation of altered material, making it a better measure of assimilation than Cl abundance alone. Recent work by Michael and Cornell (1998 in press) suggests a maximum Cl/K ratio for the MORB mantle of 0.08; values of Cl/K > 0.08 generally indicate that some assimilation has occurred.

On average, the chlorine contents of the evolved lavas are higher than those of the more primitive samples, and Cl steeply increases with decreasing MgO (Figure 11). Some of the studied samples have Cl/K ratios higher than the estimated mantle value of

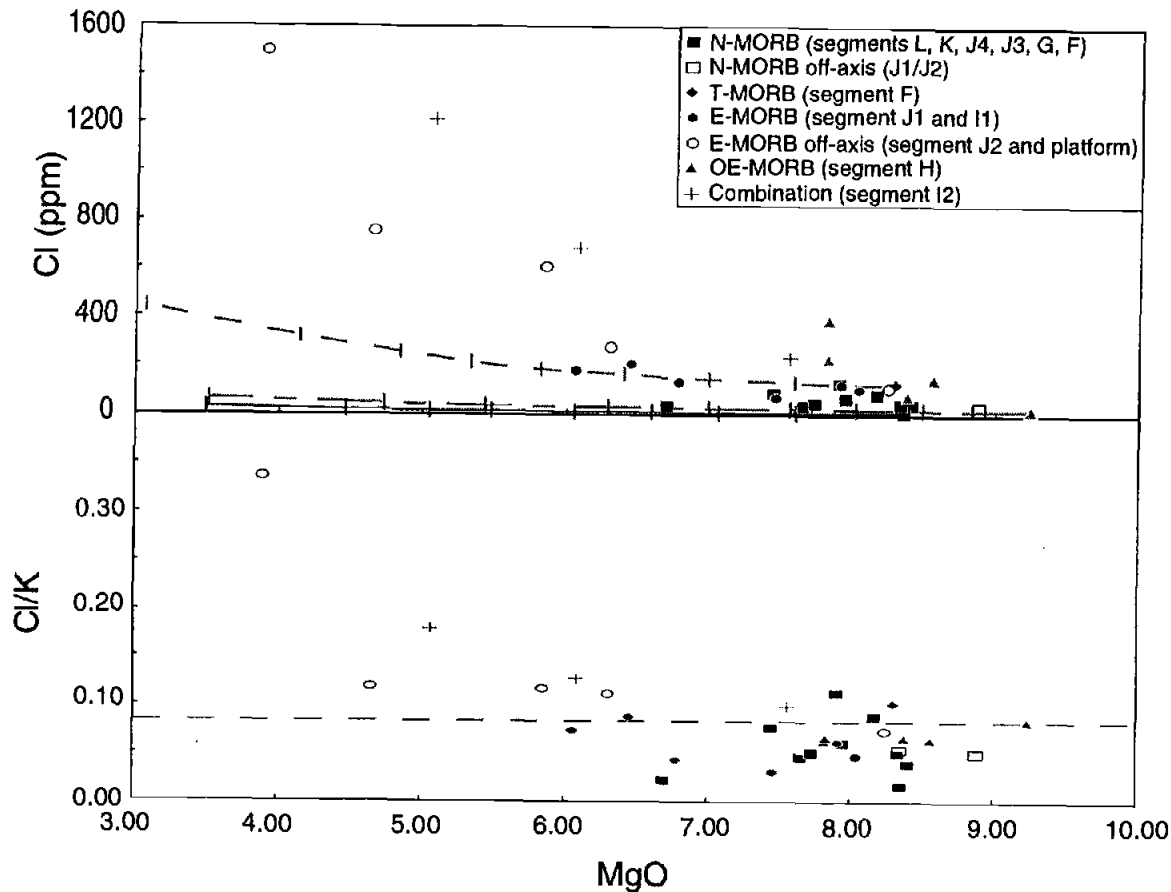


Figure 11: Cl and Cl/K as a function of MgO. N-MORB are filled squares, T-MORB (transitional) filled diamonds, E-MORB filled circles, OE-MORB filled triangles, those lavas that appear to be the result of a combination of processes (over-enrichment and fractional crystallization) are crosses, off-axis E-MORB unfilled circles, and off-axis N-MORB unfilled squares. The lines on the MgO vs. Cl represent a 1-atmosphere fractional crystallization model (Ariskin et al., 1993). Three different starting compositions were used: a N-MORB (solid line), an E-MORB (even dashes) and an OE-MORB (alternating dashes). The models are each for 80% crystallization and have tick marks for every 10% crystallization. Note that many samples exhibit much higher Cl content than that which is explainable by fractional crystallization.

0.08. Samples from segments J2, I2 and Boomerang Caldera, and possibly also from segments L and K have Cl/K values suggesting contamination. The chlorine contents of the glasses increase towards the ASP platform, and the highest Cl value occurs in the most evolved sample studied (d49-3), from the propagating rift tip on segment J2 (Figure 13). The Cl/K ratio also peaks on segment J2 (Figure 13). This observation is consistent with Michael and Schilling's (1989) finding that excess Cl is commonly found along propagating or overlapping rifts (e.g. Galapagos Spreading Center) where protracted magma storage in the crust may lead to interactions with the surrounding crust.

The minor elements K₂O, TiO₂ and P₂O₅, show similar behavior with respect to Cl, and are positively correlated with Cl (Figure 12). The increasing order of incompatibility for the minor elements is TiO₂, P₂O₅, K₂O, and Cl. When Cl is compared to these three elements, the data in all three cases intersects at positive values of P₂O₅, K₂O or TiO₂, indicating Cl is the least compatible of the four elements.

Excluding samples with Cl/K > 0.08 - 0.10, of those segments remaining, H has the largest range of Cl contents. Segment H has a wide range of K₂O/TiO₂ and yet it has a near constant Cl/K value of 0.07-0.08 (Figures 13 and 14). Segment H also appears to exhibit the strongest hotspot signal based on trace and minor elements (Johnson et al., 1996) and ³He/⁴He ratios, up to 14 R_A (Graham et al., in prep.). Because the Cl/K ratio remains essentially constant on segment H, indicating an absence of assimilation, perhaps the Cl/K ratio of the segment H lavas is equivalent to the mantle source ratio. In contrast N-MORB from segments L, K and J4 have lower Cl/K values, with the lowest Cl/K (0.02) values of the region occurring on segments J4 and L. Of those segments classified as E-MORB (segments I1, I2, J1, J2) the lowest Cl/K values observed are 0.03. With the limited chlorine data collected in this region thus far, it is difficult to unequivocally distinguish between Cl/K ratios for the E-MORB

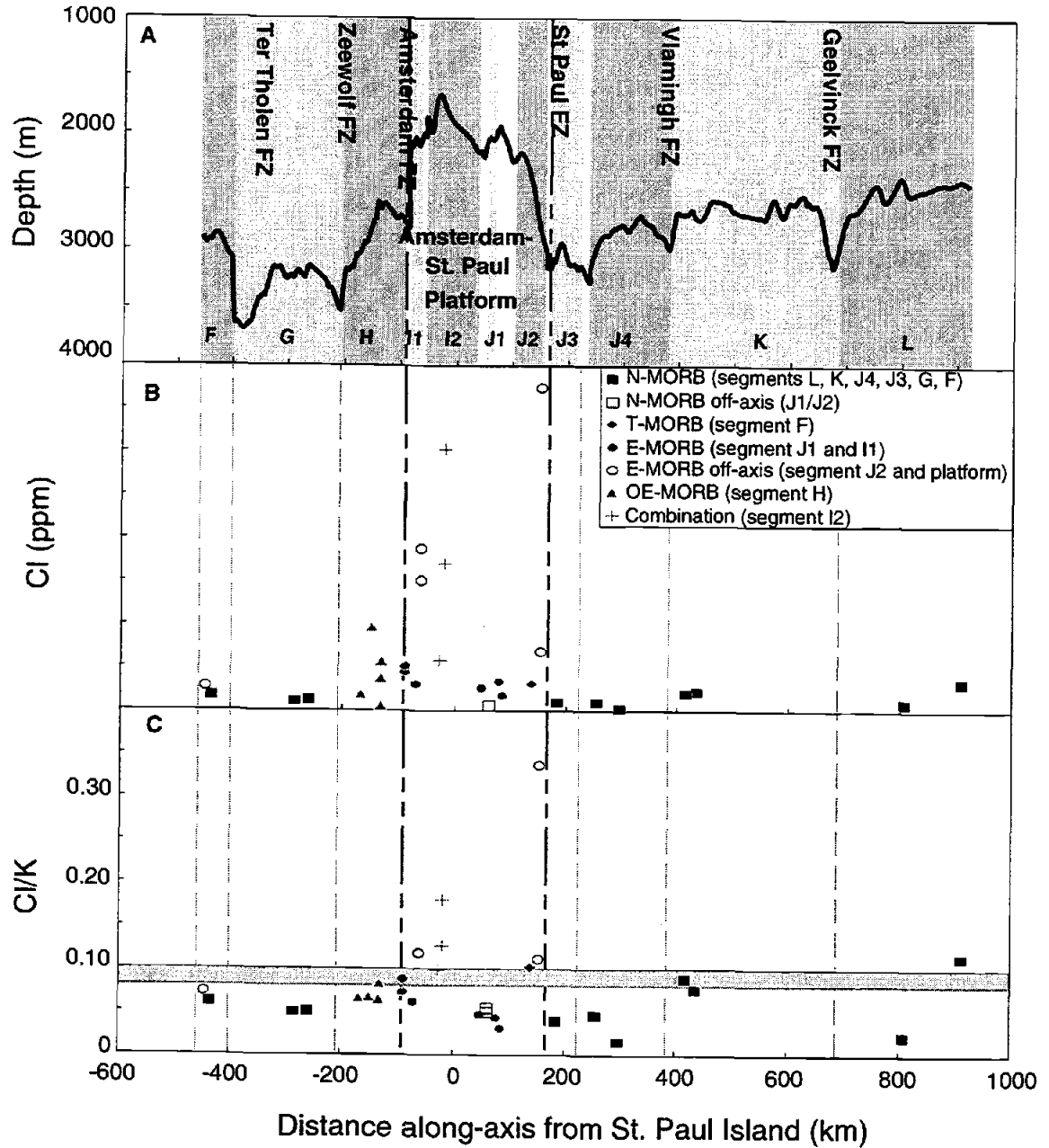


Figure 12: Variations in Cl and Cl/K along-axis. A) Depth profile, B) Cl and C) Cl/K vs. along-axis distance. In B the Cl/K ratio is the elemental weight ratio. The gray box in C is the cut-off used to infer whether assimilation has occurred. The Cl and Cl/K values show a general increase towards the platform. If those samples thought to be contaminated ($Cl/K > 0.08 - 0.10$) are excluded, the overenriched lavas have the largest range in Cl content, but a near constant Cl/K value of 0.06 - 0.08.

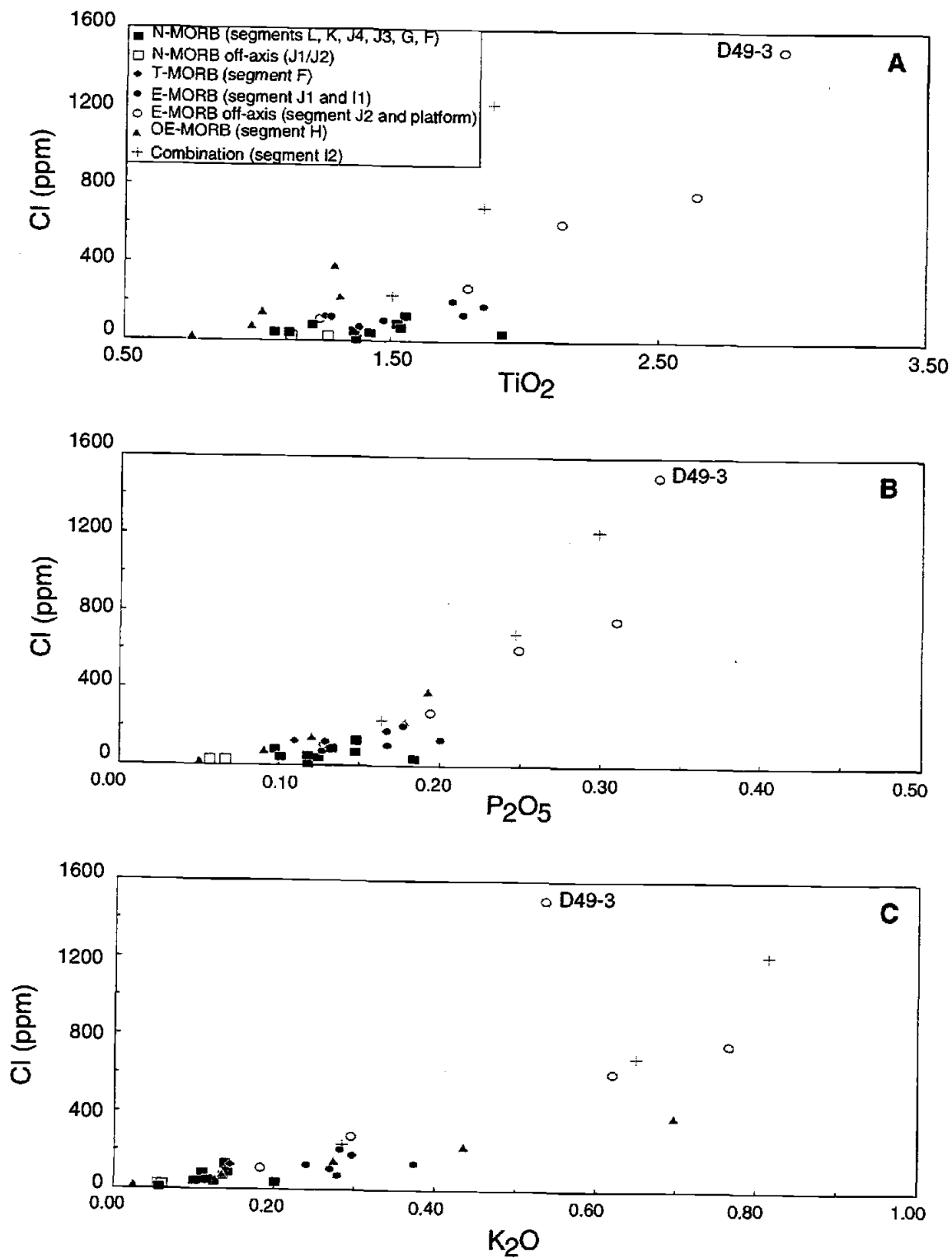


Figure 13: A) TiO₂, B) P₂O₅ and C) K₂O as a function of Cl.

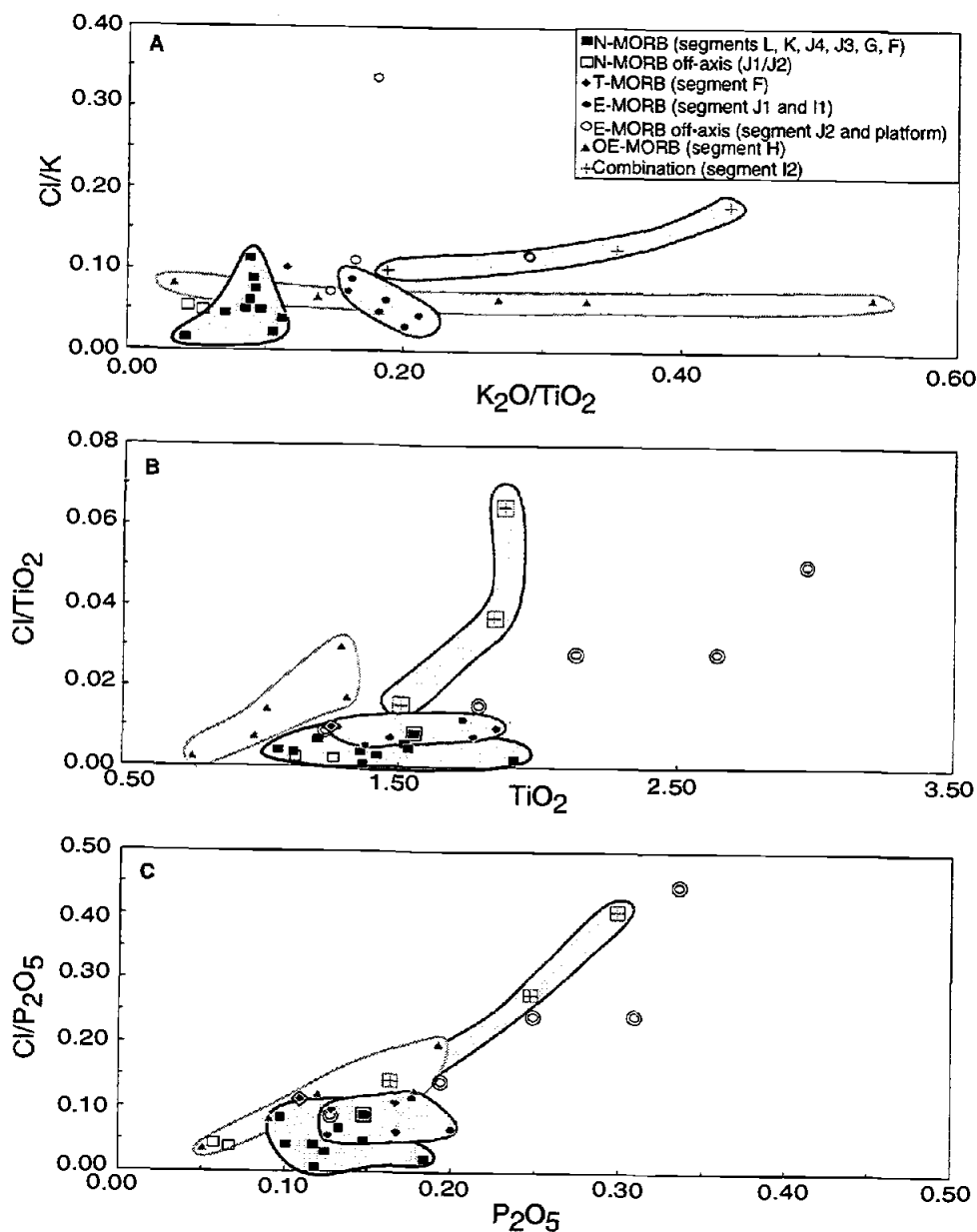


Figure 14: A) K_2O/TiO_2 vs. Cl/K , B) TiO_2 vs. Cl/TiO_2 and C) P_2O_5 vs. Cl/P_2O_5 . Symbols as in Figure 11, but in addition, those symbols which have been circled or boxed are "contaminated" lavas, as defined by the Cl/K ratio. On all three diagrams there are distinct separations between the behavior of the groupings, illustrating that several processes are affecting the lavas in this region. On the TiO_2 vs. Cl/TiO_2 diagram if those samples affected by assimilation are excluded then N-MORB and E-MORB each show tight horizontal groups of Cl/TiO_2 , with the E-MORB values perhaps being slightly higher than the N-MORB. The E-MORB samples which have been "contaminated" trend diagonally, showing a positive correlation between TiO_2 and Cl/TiO_2 . The OE-MORB of segment H trend upwards again, and samples from I2 fall in between the OE-MORB and the contaminated E-MORB samples.

and the N-MORB mantle sources. It does appear that the ASP hotspot source may have somewhat higher Cl/K ratios, based on the segment H values. However, with the uncertainties associated with these low Cl concentrations these differences may be seen as arguable without further analyses. Overall, the SEIR results agree with the variations seen on a global scale where the proposed mantle Cl/K increases from values which are below detection (≈ 0.01) for N-MORB to about 0.05-0.08 in E-MORB (Michael and Cornell, 1998 in press).

The separation of data on the diagram of TiO_2 vs. Cl/TiO_2 (Figure 14), which is comparable to the diagrams of TiO_2 vs. $\text{K}_2\text{O/TiO}_2$ and TiO_2 vs. $\text{P}_2\text{O}_5/\text{TiO}_2$ (Figure 9), illustrates that several processes must affect basalt compositions in this region. Fractional crystallization will only spread lava compositions in a horizontal direction on this diagram. If those samples with a Cl/K ratio $> 0.08 - 0.10$ (those probably affected by assimilation) are excluded, then N-MORB and E-MORB each show tight horizontal groups of Cl/TiO_2 , explainable by fractional crystallization. The E-MORB Cl/TiO_2 values may be slightly higher than the N-MORB. E-MORB samples that have been contaminated trend diagonally, showing a positive correlation between TiO_2 and Cl/TiO_2 . The trend of segment H lavas necessitates a process other than fractional crystallization, and the trend of the I2 lavas suggests a combination of assimilation and over-enrichment. The diagram of P_2O_5 vs. $\text{Cl/P}_2\text{O}_5$ is very similar to the TiO_2 vs. Cl/TiO_2 diagram, with the exception that the samples from H and the samples from I2 fall along an almost continuous line rather than showing any separation. This may be a result of crystallization: the samples are at different levels of evolution (based on MgO) and this may be reflected in the TiO_2 .

Sulfur

Sulfur concentrations of basalt glasses provide insight about the volatile content of MORB. Water and carbon dioxide are generally the most abundant volatiles in a magma but the presence of other volatile species is also important. Vapor saturation of a magma occurs when the sum of all of the vapor pressures of individual species exceed the total pressure, and saturation can occur even though the solubility of no individual species has been exceeded (Carroll and Webster, 1994). This makes it necessary to understand as much as possible about the behavior of all volatile species present if the behavior of one is to be completely understood. Sulfur solubility in a silicate liquid is dependent on temperature, pressure, bulk composition, and the fugacities of oxygen and sulfur (Haughton et al., 1974; Luhr, 1990). Sulfur correlates well with FeO concentrations in basaltic magmas (Wallace and Carmichael, 1992). The most common S species in basaltic liquids are sulfide (S^{2-}) and sulfate (SO_4^{2-}). At fO_2 near and less than the FMQ buffer, S occurs mainly as sulfide (>80%) (Nagashima and Katsura, 1973; Katsura and Nagashima, 1974; Carroll and Rutherford, 1988; Wallace and Carmichael, 1992).

The sulfur content of a melt increases during crystal fractionation as long as the magma is under-saturated with respect to sulfur. Even if a magma is saturated, the sulfur content may still increase during fractionation because sulfur solubility may increase in the residual liquid (Wallace and Carmichael, 1992). Prior to eruption mid-ocean ridge lavas are thought to be sulfide-saturated because glassy pillow rinds of MORB have been noted to have much higher S contents than pillow interiors or subaerially erupted lavas (Moore and Fabbi, 1971; Mathez, 1976). During submarine eruption MORB lavas are rapidly quenched and many of their volatile constituents are

retained in the glass (Mathez, 1976; Czamanske and Moore, 1977; Wallace and Carmichael, 1992).

Sulfur was measured in the same SEIR glasses analyzed for Cl. The range of sulfur concentrations is 900-2000 ppm, but excluding FeTi basalt sample d49-3, the range is only 900-1400 ppm and the increase in sulfur is very gentle, with the steepest increase occurring at the highest MgO values (Figure 15).

The range of sulfur along-axis is relatively constant with no real separation between the on- and off-platform segments (Figure 16). Segment H has the lowest sulfur values (900 ppm). The SEIR data form a tight positive array on a plot of FeO^* vs. S, with the exception of the FeTi basalt from dredge 49 (d49-3), mentioned above (Figure 15). This covariance between FeO and S is indicative of the complexation of FeS in the liquid (Mathez, 1976), and represents the saturation surface for the immiscible Fe-S-O liquid (Wallace and Carmichael, 1992). When compared to the FeO^* vs. S diagram of Figure 2 in Wallace and Carmichael (1992) in which both experimental glasses, and a global set of natural glasses are plotted, the values of the ASP lavas fall between the natural and experimental glasses. The FeO^* vs. S diagram shows more clearly than the MgO vs. S diagram that as the magma evolves, S content increases. This is also true of the TiO_2 vs. S diagram (Figure 15).

There is no correlation between Cl and S (not shown), which precludes crustal interaction as an influence on the S content of these lavas. To investigate the possible relationships between the S content of the lavas and the degree of over-enrichment or strength of a hotspot signature, S vs. $\text{K}_2\text{O}/\text{TiO}_2$ is plotted in Figure 17. There is a wide range of $\text{K}_2\text{O}/\text{TiO}_2$ and a small range for S. A lack of a correlation between S and $\text{K}_2\text{O}/\text{TiO}_2$ indicates that there is no discernible S enrichment associated with the hotspot.

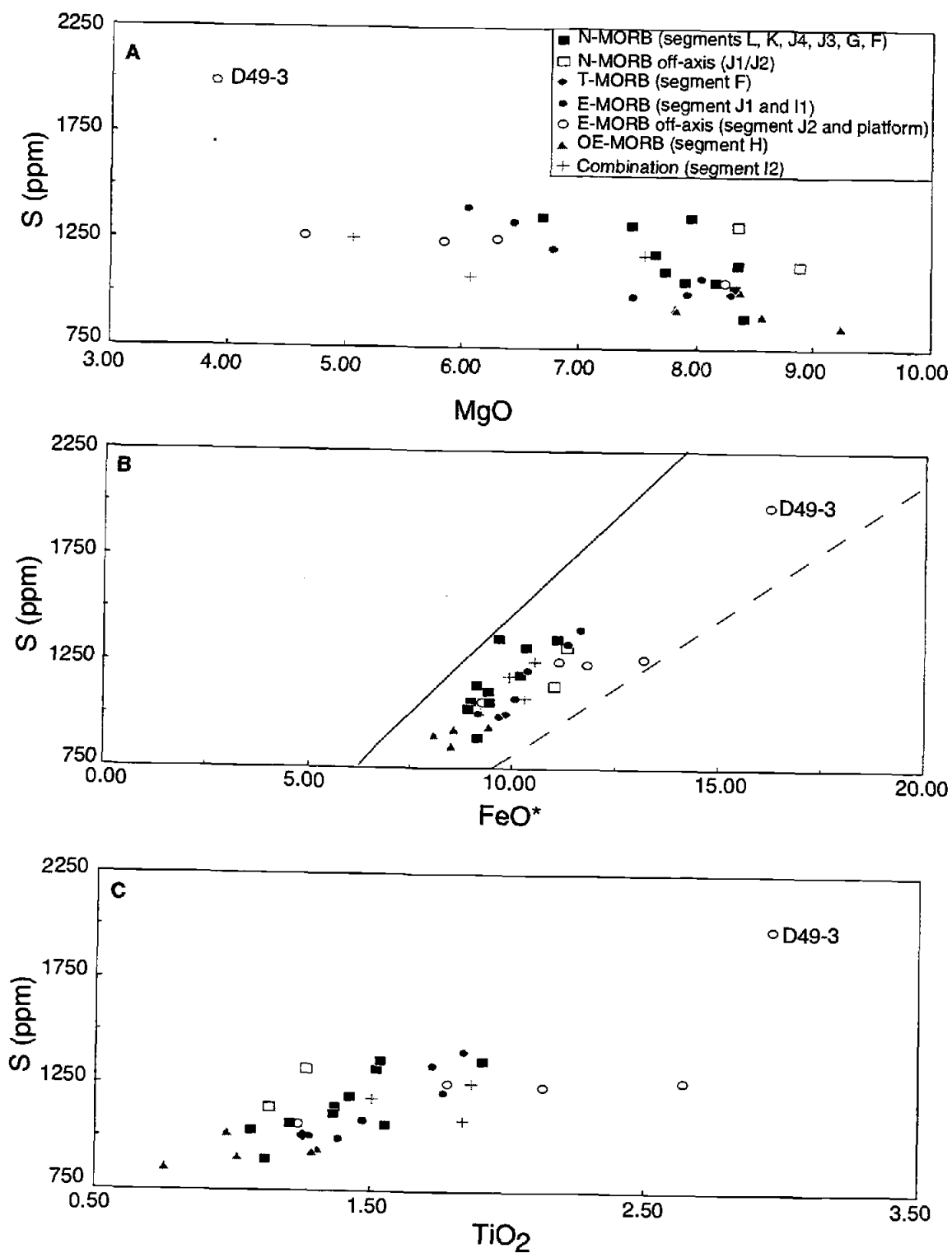


Figure 15: A) MgO, B) FeO*, and C) TiO₂ vs. S. Lines in B are taken from Wallace and Carmichael (1992) to represent the trends of both experimental (dashed line) and the global set of natural glasses (solid line).

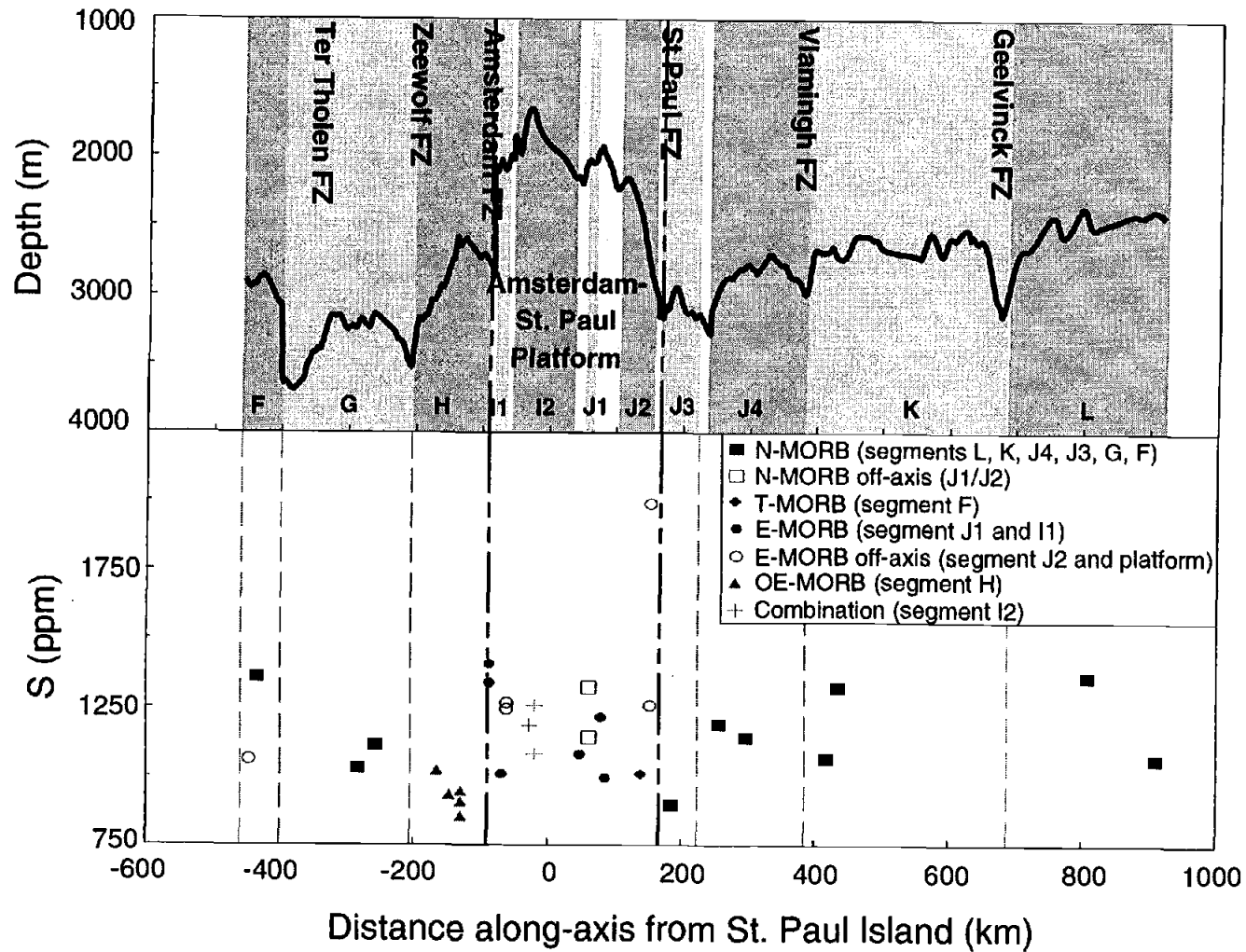


Figure 16: Variation of S as a function of distance along-axis.

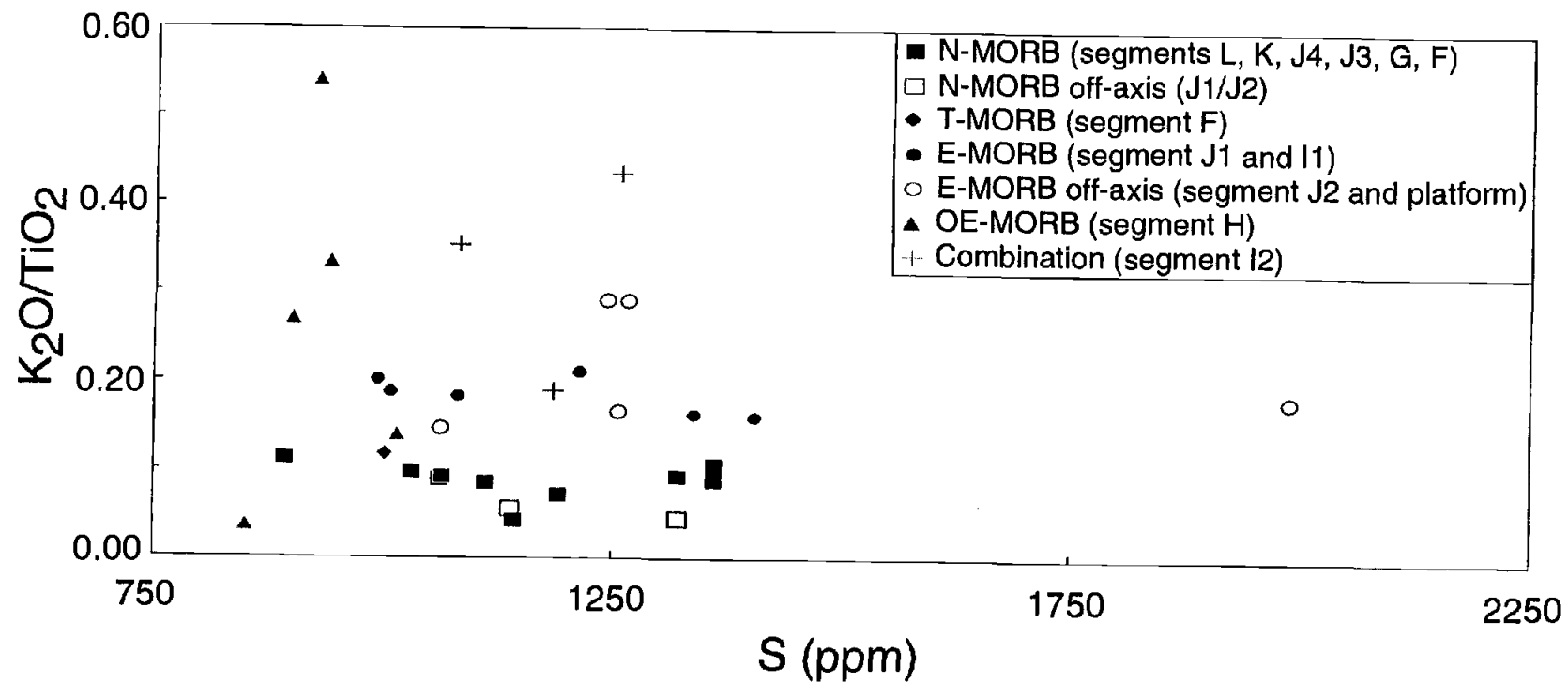


Figure 17: S versus K_2O/TiO_2 .

Discussion

Implications of Assimilation

Understanding the extent to which a magma has been modified during its ascent and eruption is fundamental to the study of the chemical systematics of mid-ocean ridges. If the chemistry of MORB is to tell us about mantle processes and composition, then it is necessary to understand the entire path of a magma after it has separated from the mantle and journeys to the surface. One modification process that can potentially occur in the crust before a lava is erupted at a mid-ocean ridge is the assimilation of solid or fluid materials (such as altered oceanic crust) into the magma. Hydrothermal vents along mid-ocean ridge systems attest to the transfer of heat and material from hot rock or magma into sea water, but the extent to which transfer occurs happens in the reverse direction is uncertain (Michael and Schilling, 1989). Evidence for assimilation along the mid-ocean ridges is provided by elevated chlorine levels in zero-age MORB glasses from areas such as the East Pacific Rise and the Juan de Fuca Ridge (Michael and Schilling, 1989; Michael and Cornell, 1998 in press). Assessing whether a magma has assimilated crustal material can be difficult, because the crust surrounding a magma chamber or through which a MORB magma ascends is very similar in composition. Consequently, the major element chemistry of the MORB magma following assimilation will not be noticeably different (Fisk et al, 1995; Michael and Cornell, 1998 in press). However, because chlorine concentrations are low in primary magmas (20-50 ppm), and high in sea water and hydrothermally altered material, the chlorine content of basalt glass is a sensitive indicator of assimilation (Michael and Schilling, 1989).

It is hypothesized that the low $^3\text{He}/^4\text{He}$ isotopic signatures of some basalts near ridge offsets are a result of gas loss and assimilation of altered oceanic crust (Graham and Lupton, 1992). Results of an experimental study of the effects of assimilation on magma composition by Fisk et al. (1995) indicate that the assimilation of partial melts of altered oceanic crust into a magma chamber may explain local variability of MORB not readily explainable by fractional crystallization or partial melting. Altered dike basalts from Hole 504B were partially melted at 1150°C and 1180°C to determine the effect on melt composition if oceanic Layer 2C material is incorporated into a magma chamber. The chemistry of the partial melts was controlled by the composition of the secondary minerals present and by the temperature of melting. Assimilation of a partial melt of altered oceanic crust can lower La/Sm, increase Ti, Y, Yb and Zr, and produce a REE pattern in the contaminated basalt that will cross the REE pattern of an evolved, uncontaminated basalt (Fisk et al., 1995). There are other possible explanations for crossing REE patterns such as variable degrees of dynamic melting (Langmuir et al., 1977). In combination however, high Cl contents, low $^3\text{He}/^4\text{He}$ ratios, and crossing REE patterns are a strong argument for assimilation (Fisk et al., 1995).

Chlorine concentrations in fresh MORB glasses vary widely when compared to other trace and major elements (Michael and Schilling, 1989). Relatively primitive, incompatible element-depleted glasses typically have 10-40 ppm Cl (Schilling et al, 1980; Byers et al, 1984). In contrast, Cl values as high as 1000 ppm and 8000 ppm have been measured in FeTi basalts and rhyodacites, respectively (Byers et al., 1983, 1984). The size, depth, crystal content and lifetime of a magma chamber or magma lens differs between fast- and slow-spreading ridges (Sinton and Detrick, 1992). Fast-spreading ridges appear to be underlain by thin magma lenses at 1-3 km depth, while seismic velocities beneath slow-spreading ridges do not reveal a magma lens but instead suggest a small mush zone several kilometers within the crust (Toomey et al., 1988). The presence or absence of a magma chamber will result in the eruption of different

suites of lava (Sinton and Detrick, 1992). MORB from fast-spreading ridges define LLD that are consistent with simple fractional crystallization at shallow levels (0-2 kb) (Grove et al, 1992; Michael and Cornell, 1998 in press) and often have higher chlorine contents than can be accounted for by simple fractionation (Michael and Schilling, 1989; Jambon et al., 1995). This excess Cl suggests that a magma has crystallized at a level in the crust sufficiently shallow to assimilate high Cl material (Michael and Cornell, 1998 in press) such as high Cl amphibole, Cl-rich brine or some portion of altered crust (Michael and Schilling, 1988; Magenheim et al, 1995). MORB from slow-spreading ridges generally define LLD that are consistent with higher pressure crystallization (3-6 kb) (Grove et al, 1992; Michael and Cornell, 1998 in press) and frequently have low Cl contents (Michael and Schilling, 1989). The lower magma flux, and colder crust and lithosphere of slow-spreading ridges cause magmas to crystallize at deeper levels. They must therefore ascend rapidly in order to be erupted, resulting in a signature of higher pressure crystallization. These magmas do not assimilate shallow crustal material to any significant degree, and they maintain a mantle-like Cl/K ratio. MORB suites crystallizing at low pressures reside for longer times in the crust, and have higher Cl/K as a result of more intense interaction with the crust.

The increase of Cl content in some ASP lavas is not explainable by fractional crystallization alone and another process, such as assimilation, must be invoked to explain the data. Because the Cl/K ratio of segment H is relatively constant the Cl over-enrichment of segment H however, is not explainable by assimilation, and requires another source, possibly the ASP plume. So we must consider the likelihood that a number of factors, including assimilation and an over-enriched component, affect the Cl content of these basalt glasses.

Because the spreading rate is not a variable in this area, the observation that ASP platform lavas show some clear signs of magma-crust interactions suggests that on a local scale (100 - 200 km length), the presence of thicker crust has increased the

likelihood of magma-crust interaction. It is also possible that as a result of the ASP hotspot's presence, the crust is warmer beneath the platform, allowing for extended magma-crust interaction.

Global Major Element Correlations

Klein and Langmuir (1989, 1987) recognized that systematic global variations in averaged MORB chemistry correlate with axial depth. These variations in MORB chemistry reflect varying degrees of melting and varying depths of melting of a peridotitic mantle source. The sodium content of a magma decreases with an increased degree of melting, and the FeO* content increases with an increased pressure of melting. When the global MORB data set is corrected for the effects of shallow-level crystal fractionation, the average Na₂O and SiO₂ correlate positively with axial depth, while FeO* and CaO/Al₂O₃ show negative correlations with axial depth. The corrected values can be used to determine the mean depth and degree of melting along-axis. Increased melting is expected in association with hotspots, so ridge segments in the ASP region, closer to the hotspot, such as on the ASP platform could be expected to produce lavas reflecting greater degrees of melting and mean pressures of melting than segments further away from the hotspot. The lateral extent of such influence depends on the degree to which the ASP hotspot has influenced the temperature and composition of the mantle under the ridge segments in this region.

Klein and Langmuir (1989) considered both the global and local effects on MORB composition. In their melting column model (Figure 18) hotter mantle intersects the solidus at a greater depth creating a taller melting column, resulting in greater mean pressures and extents of melting. Colder mantle intersects the solidus at a shallower depth, creating a shorter melting column, and leading to lower mean

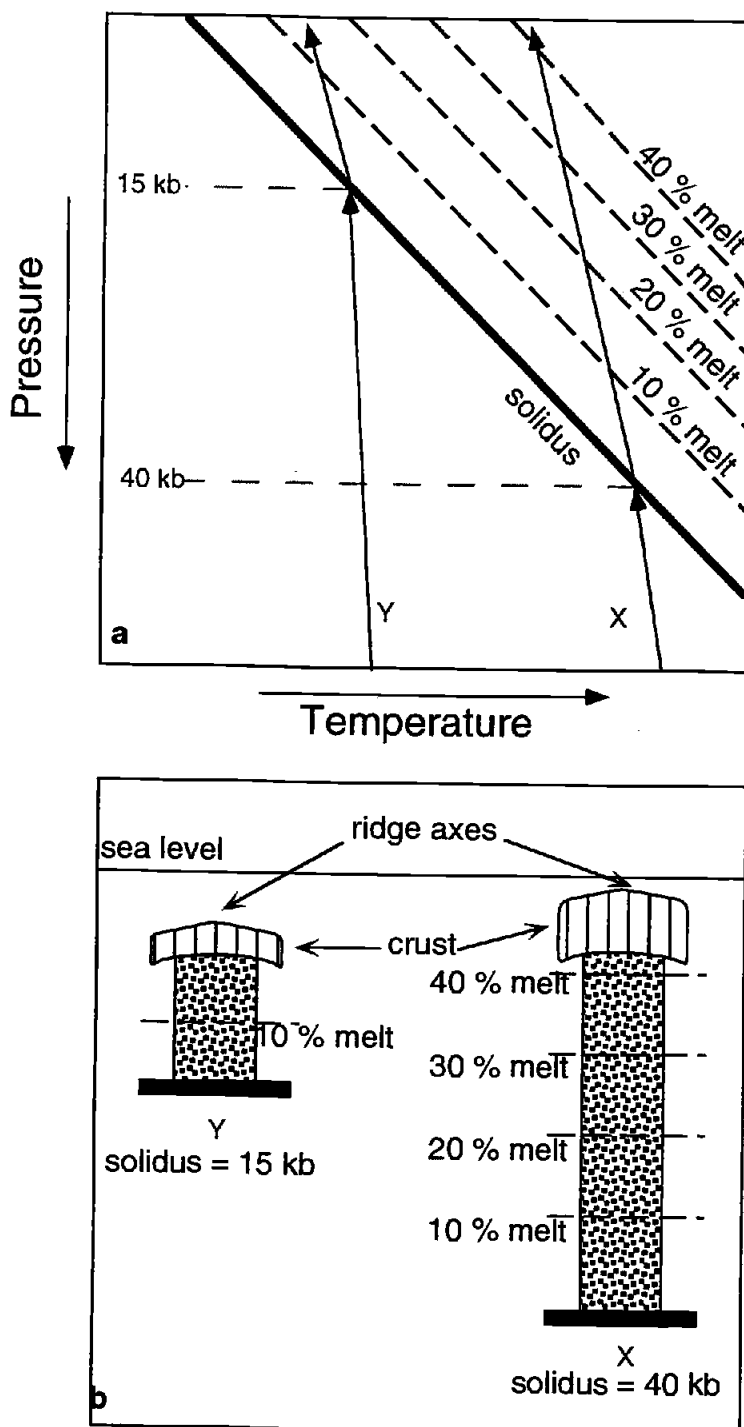


Figure 18: Klein and Langmuir's (1987, 1989) mantle melting column model. a) Schematic drawing of mantle melting relationships. Path X represents a hotter parcel of mantle that intersects the solidus at greater depth and undergoes greater extents of melting upon ascent; Path Y, a cooler parcel of mantle, intersects the solidus at shallower depth and melts less upon ascent. b) Schematic cross section of the oceanic crust and mantle resulting from Paths X and Y.

pressures and extents of melting. The global trends of MORB major element compositions can be explained by temperature variations between different melting columns or "inter-column" variations. Local effects are produced by "intra-column" variations, which are the result of the imperfect aggregation or pooling of instantaneous melts from a single melting column. Within a single column, the lowest degree melts have the deepest (high pressure) origin and the highest degree melts the shallowest (low pressure) origin. This can produce local chemical variations that are opposite to the global systematics and the local trend of chemical variation will be approximately orthogonal to the global trend (Klein and Langmuir, 1989).

In the vicinity of the ASP platform the use of Na_8 , Fe_8 and the $\text{CaO}/\text{Al}_2\text{O}_3$ ratio to infer the degree and depth of melting is not as straightforward as along normal ridge segments due to the presence of the ASP hotspot. Klein and Langmuir (1989) made distinctions within their global data set between normal ridge basalts, back-arc basin basalts and hotspot-influenced ridge basalts. Compared to normal ridges, some hotspot-influenced ridges have anomalous major element compositions, e.g. low Fe_8 and sometimes low Na_8 . The Galapagos Spreading Center is such a case, in which the relationships between Na_8 , Fe_8 and depth, are opposite of that observed globally (Langmuir et al., 1992). The shallowest regions of the Galapagos ridge system have the lowest Fe_8 and the highest Na_8 . However, not all hotspot-influenced ridges show anomalous behavior. Along the Reykjanes Ridge for example, major element data are consistent with the global relationships of normal ridge basalts.

The running average values of Figure 10 are compared with the values predicted from the global correlations with axial depth of Na_8 , Fe_8 and $\text{CaO}/\text{Al}_2\text{O}_3$ in Figure 19. Linear equations for each of the three parameters were determined from the original Klein and Langmuir major element-depth relationships. Using these equations allows the prediction of Na_8 , Fe_8 and $\text{CaO}/\text{Al}_2\text{O}_3$ variations from the variation in ridge-axis

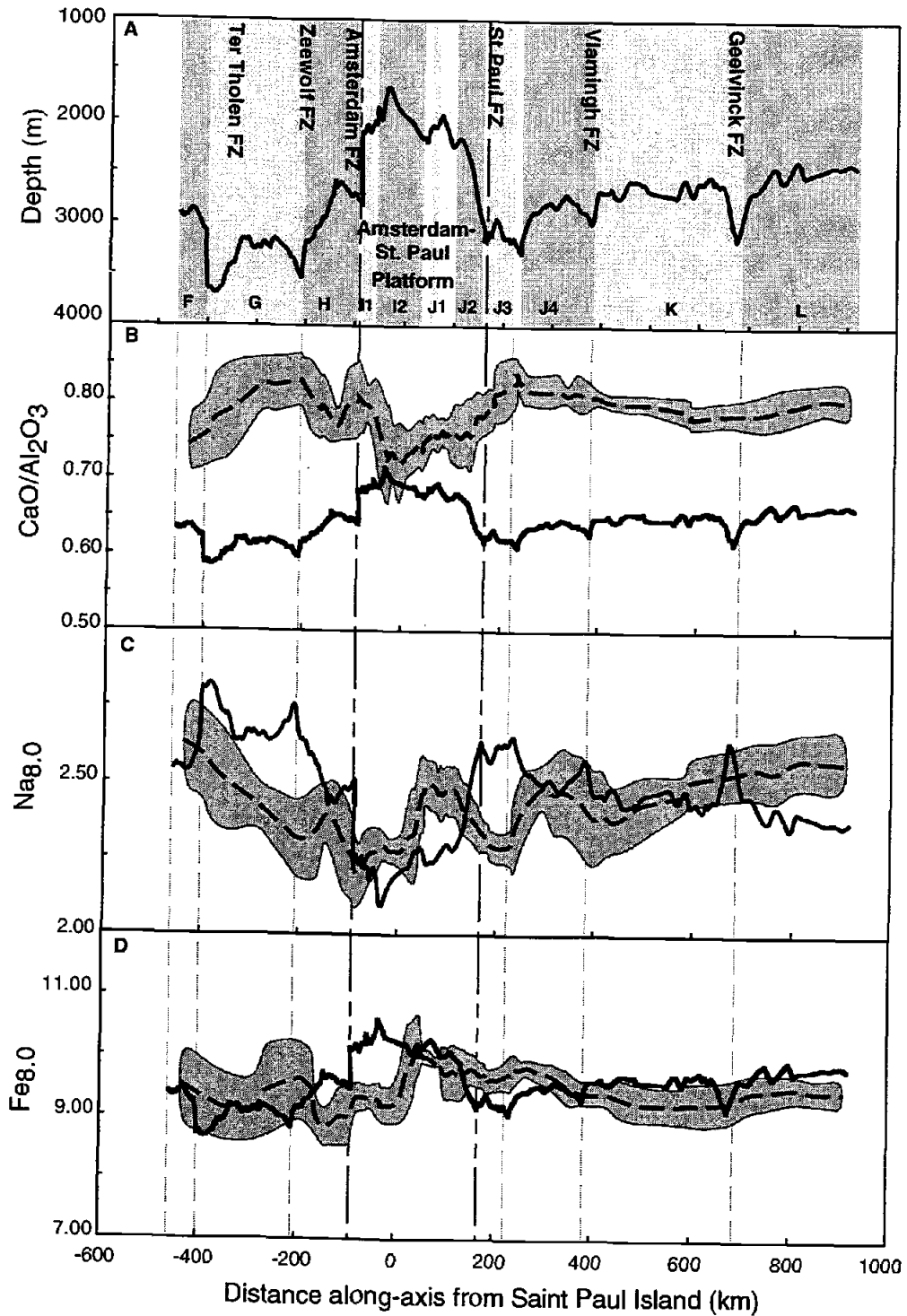


Figure 19: Along-axis variations in observed and predicted fractionation-corrected oxides. A) Along-axis depth profile. B) $\text{CaO}/\text{Al}_2\text{O}_3$, C) $\text{Na}_{8.0}$ and D) $\text{Fe}_{8.0}$ vs. along-axis distance. The enveloped dashed lines shown on B, C and D are five point running averages of the on-axis samples with the shaded envelope representing ± 1 standard deviation. The unenveloped line represents the predicted values.

depth in the ASP region. Predicted and observed values of Fe₈ agree in several areas along-axis (Figure 19). Southeast of the ASP platform (along segments L, K, J4, and J3), the observed Fe₈ shows a long wavelength (~ 500 km) increase towards the platform, while the predicted values decrease slightly over this same region. Along segments I1, I2 and H, the observed and the predicted Fe₈ trends are the most different, with observed values up to 1 wt. % lower than the predicted. Beyond Segment H, to the northwest of the platform, as well as on Segments J2 and J1, the predicted and observed Fe₈ overlap one another within uncertainty.

Predicted and observed Na₈ values both increase away from the platform to the northwest although the observed values are systematically lower by up to 0.5 wt. %. Predicted Na₈ increases towards the platform from the southeast, along J4, but it then drops sharply along J2; in contrast, the observed values decrease towards the platform, then increase on segments J2 and J1, and then sharply drop along segment I2.

The predicted and the observed values of CaO/Al₂O₃ do not overlap anywhere in the region. The observed CaO/Al₂O₃ values are significantly higher than the predicted values, and the two lines are essentially the inverse of one another. Segments L and K, and F, G and H show systematic offsets of -0.15 in CaO/Al₂O₃. In addition, segments J4 through H show opposite trends to those predicted from axial depth. It is clear that the observed variations in Na₈, Fe₈ and CaO/Al₂O₃ do not mimic the predictions from Klein and Langmuir's global relationships. Plotting the CaO/Al₂O₃, Na₈ and Fe₈ data in Figures 10 and 19 using a five-point running average. This helps to remove the "noise" from individual dredges, and provides more of a segment-scale view. Nevertheless, the averaging of the data is on a significantly shorter scale than the global data set of Klein and Langmuir (1989), and some of the differences between the observed and predicted values must certainly be attributed to the 'local effects' of Klein and Langmuir (i.e. imperfect aggregation of instantaneous melts). However, even

considering the 'local effect', the differences between the observed and predicted values are still significantly different, especially with respect to $\text{CaO}/\text{Al}_2\text{O}_3$ (Figure 19).

Given that local chemical variations are opposite to global systematics, then the local vector of chemical variation should be approximately orthogonal to the global one (Klein and Langmuir, 1989). Relative to global and local trends, i.e. those produced by "inter"- and "intra-column" effects, most of the ridge segments show a near-horizontal trend on the $\text{Fe}_8 - \text{Na}_8$ diagram, owing to the relatively larger variations in Fe_8 compared to the variations in Na_8 for our sample suite (Figure 20). This trend is intermediate between the global and local trends. The observation that most of the SEIR data from this region lie on near-horizontal trends suggests that mantle melts separate from their source in this region over a range of mean pressures, as evidenced by the relatively large variations in Fe_8 and as predicted for local variability in the melting column model. However, on the scale of individual ridge segments, these liquids appear to represent similar extents of melting, as evidenced by their relatively smaller variations in Na_8 . The fact that the near-horizontal trends are intermediate to the global and local vectors supports the contention that factors other than those associated with imperfect pooling of melts from throughout the melting column (such as source heterogeneity introduced by the ASP hotspot) also play a role in the genesis of MORB magmas from this region. Support for the involvement of factors other than "intra-column" (local) effects is also found in examination of Si_8 vs. Na_8 (Figure 20b). Like FeO^* , SiO_2 systematics are dependent on the pressure as well as the extent of melting. For a given extent of melting, increased pressure causes SiO_2 to decrease (Klein and Langmuir, 1987). Here again, as seen on the Fe_8 versus Na_8 plot, the data have a horizontal trend which fits neither local nor global trends of Klein and Langmuir.

Another explanation other than the 'local effect' of Klein and Langmuir is clearly required for the behavior of the ASP major elements. Because some hotspot

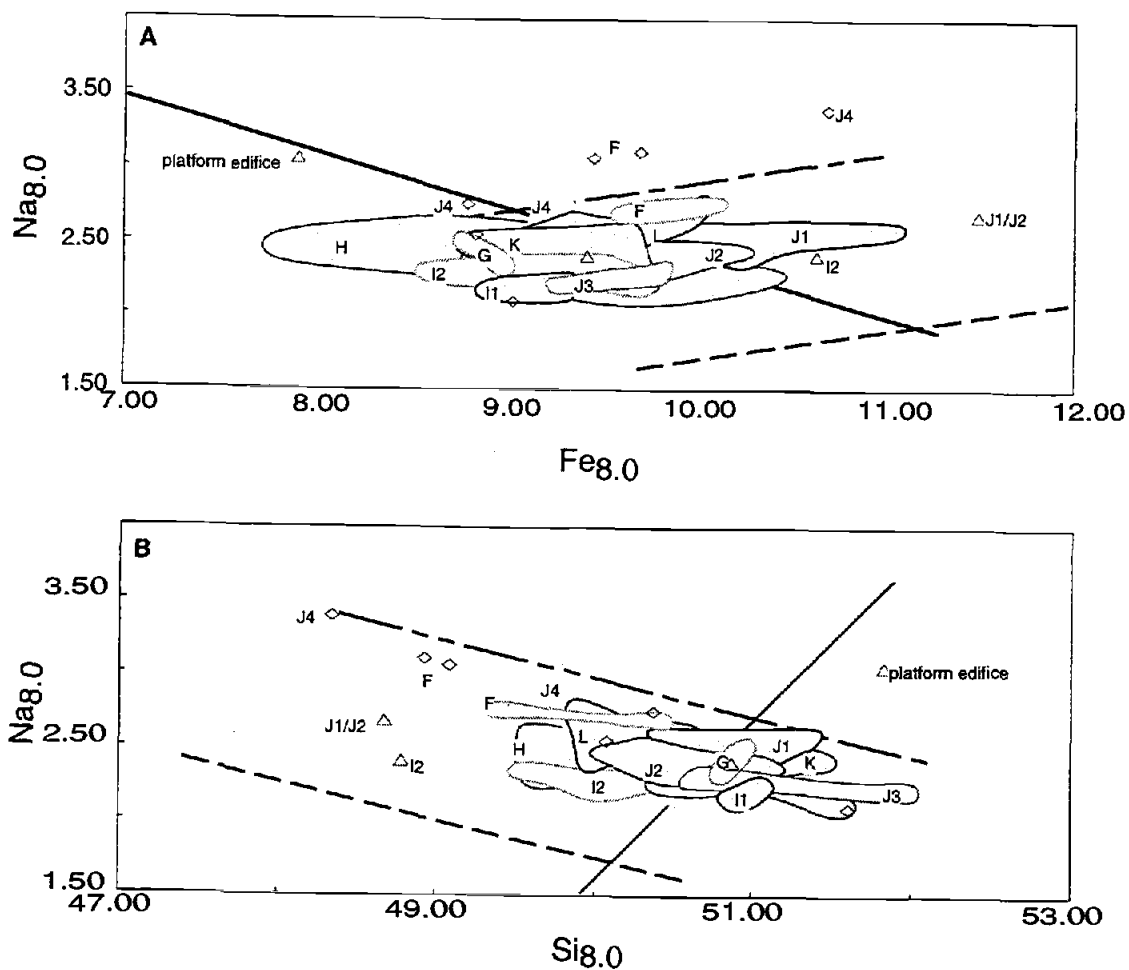


Figure 20: A) Fe₈ vs. Na₈ and B) Si₈ vs. Na₈. Data fields for each of the segments are shown, rather than the individual points, with the exception of the off-axis samples which are shown by unfilled triangles for ASP platform samples, and unfilled diamonds for those off-platform. The solid line shown is the global trend of Klein and Langmuir (1989), taken to primarily reflect variations in mantle temperature and the resulting chemical effects associated with sampling different melt columns. The dashed lines are two of Klein and Langmuir's (1989) local vectors from Rekyjanes Peninsula (even dashes) and 11.4° N - 11.97° N on the MAR (alternating dashes). The local vector on this diagram is typically orthogonal or oblique to the global trend, and is a result of chemical variations associated with the sampling of instantaneous melts from a single melting column.

basalts have anomalous major element compositions (low Fe₈ and sometimes low Na₈) compared to MORB at the same depth (Langmuir et al., 1992), those ridge segments exhibiting the strongest hotspot signal as inferred from minor and trace elements and ³He/⁴He ratios, could be expected to show the largest geochemical deviation from predicted values. In the case of Fe₈, segments H, I1 and I2 do have values lower than predicted from axial depth, while in a general sense the Fe₈ of the ASP region as a whole is not far from the predicted values. Overall the along-axis trend of observed Na₈ is slightly lower than predicted, however atop the platform, the observed Na₈ is higher than predicted. This may be the result of a source region which is initially richer in sodium. The most striking deviation is in the observed CaO/Al₂O₃ from the predicted ratio. While the plot of predicted values along-axis mimics the depth profile, the observed values are the exact opposite. As mentioned earlier the low CaO/Al₂O₃ ratios atop the platform and the positive covariation of Na₈ and Fe₈ in this same area, qualitatively suggests high pressure fractionation of clinopyroxene.

Crystallization

In an attempt to more completely assess the nature of melting and crystallization beneath the ASP region of the SEIR, a crystallization model was utilized. Numerous modeling attempts were made with variations in the starting compositions and the pressures of crystallization, but here only the models which proved to be relevant are included for discussion. In judging the quality of fit for each model to the ASP data, the off-axis data were excluded.

Initially the 1-atmosphere isobaric fractional crystallization model of Nielsen (1990) was adopted, using primitive compositions (based on MgO) from segments J2 and H. This modeling proved inadequate to fit the ASP data. Next, pressure was

increased to values between 1 - 12 kb (1, 2, 3, 4, 5, 6, 8, 10 and 12) using the COMAGMAT model of Ariskin et al. (1993). The most primitive compositions from each of the eleven segments were chosen as starting points. Of the starting compositions used, the segment K composition appeared the most likely parental composition to the data set as a whole. On each of the diagrams in Figure 21 only those pressures best fitting the data have been included, and these pressures differ for the different elements. A number of the isobaric models mimic individual elements fairly well, but no single pressure consistently works for all the elements. For instance, the CaO data was best modeled by crystallization at 1 and 2 kb, whereas for FeO* the 8, 10 and 12 kb models fit best.

Because of this inconsistency in the isobaric model results, the polybaric fractional crystallization model of COMAGMAT (Ariskin et al., 1993) was tried. This is a decompression model in which a specified increment of crystallization occurs for pressure decreases of a specified increment. Once a specified minimum pressure is reached, the lava continues to crystallize up to 80%, or to an otherwise specified crystallization amount. The models were run to a minimum pressure of 1 atmosphere (Figure 22). For example, in the 6 kb model, crystallization began at 6 kb and finished at 80% crystallization when the pressure was 0.001 kb. However, the models are shown only to 60% crystallization. As in Figure 21 only those models fitting the ASP data reasonably well are included, but in this case there is more consistency when all the elements are considered collectively. Those models providing the most consistent results are the 2, 3, 4 and 5 kb polybaric models. Of these four pressures, the 4 kb model appears to provide the best fit. However, differences of ± 1 kb associated with these models are probably not resolvable.

An attempt has been made here, using only the major elements, to gain a basic understanding of the type of crystallization processes that have taken place, and it appears polybaric crystallization is responsible for the generation of the ASP lavas.

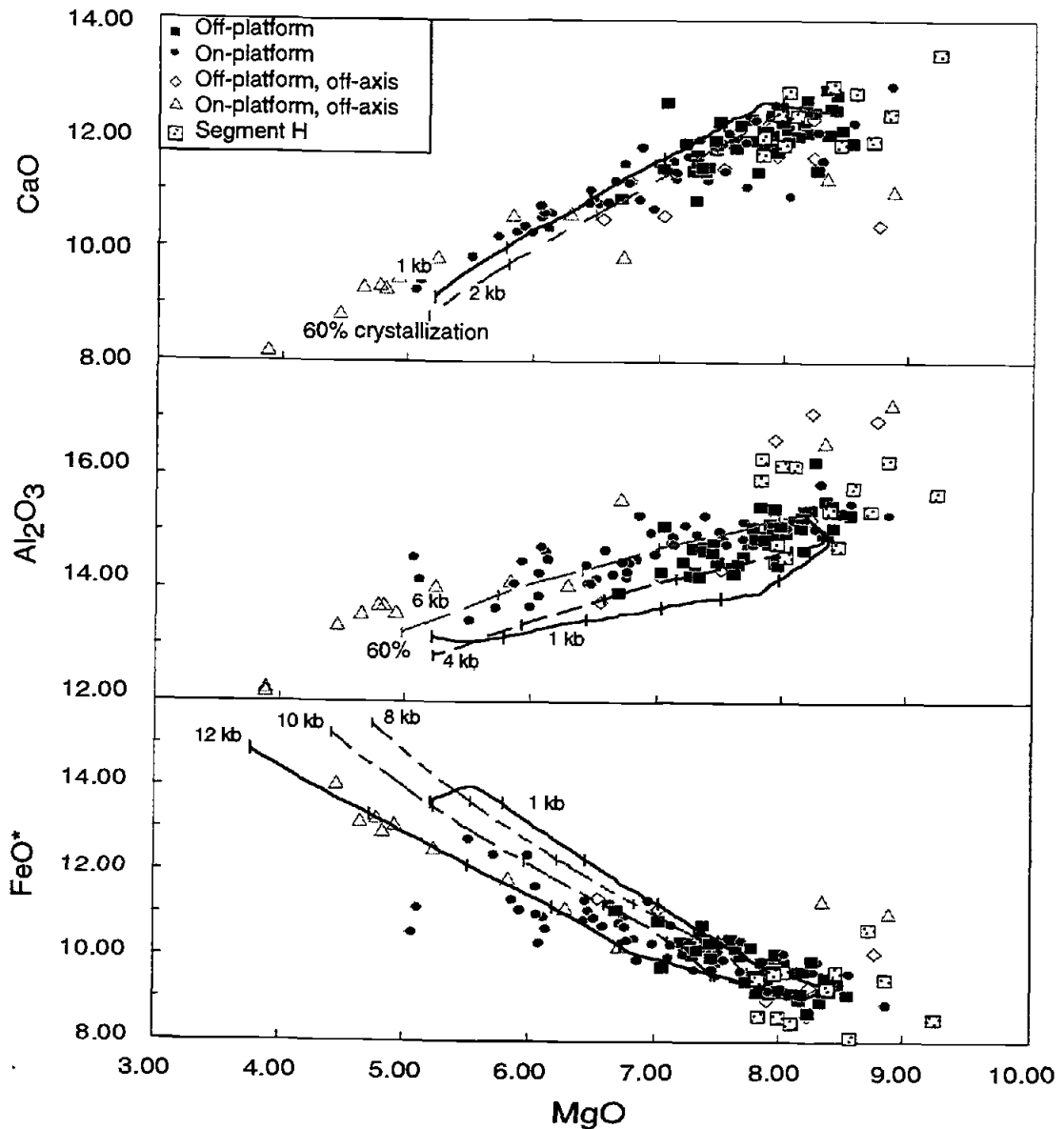


Figure 21: Isobaric fractional crystallization model. The ASP data is plotted with the LLD predicted by the COMAGMAT program of Ariskin et al. (1993). The starting composition used was a primitive composition from segment K, and the models were run at the FMQ buffer. Each LLD represents a different pressure and is labeled with that pressure. The models are for 60% crystallization and the tick marks on the LLD represent 10% crystallization increments.

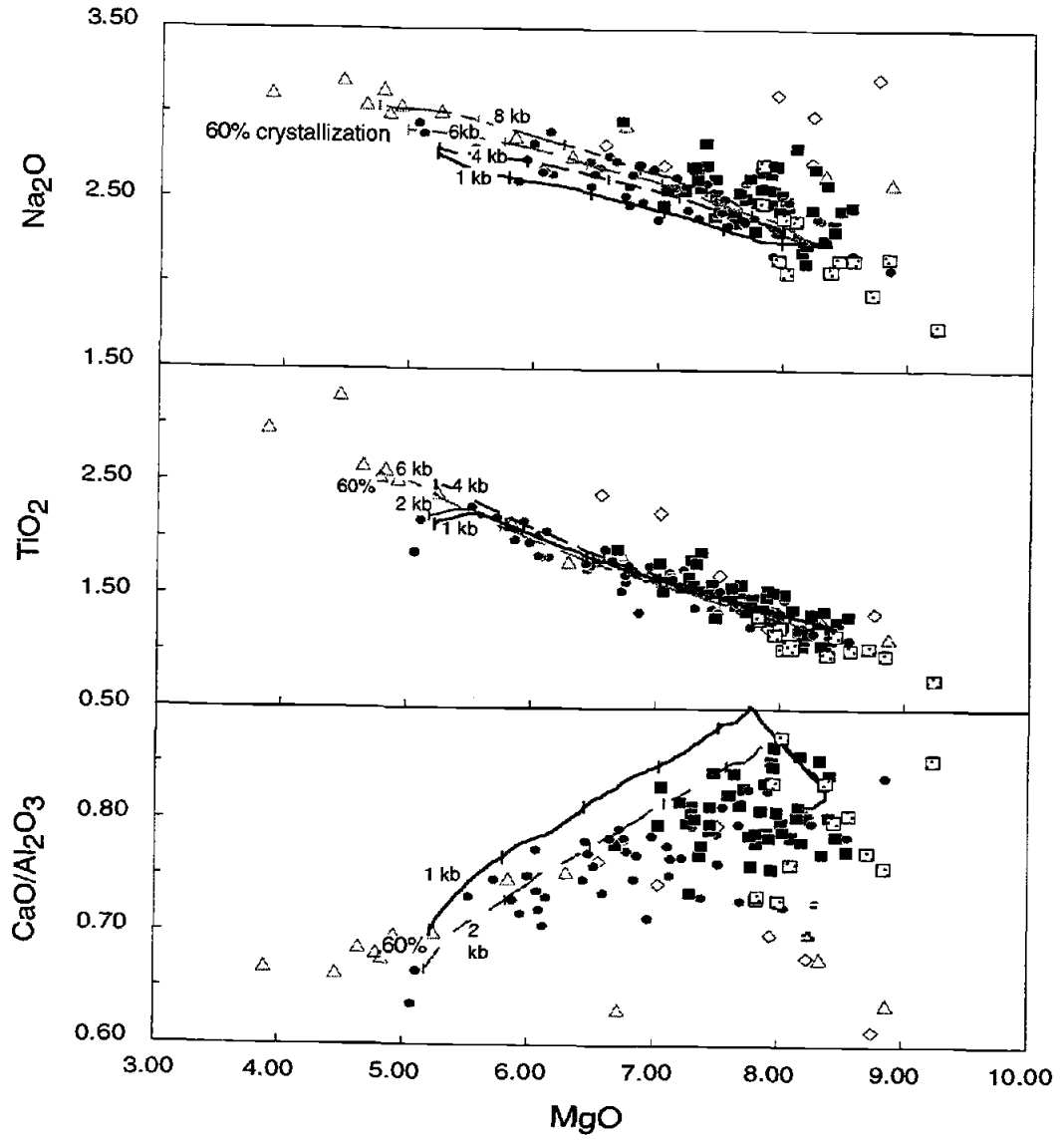


Figure 21 continued.

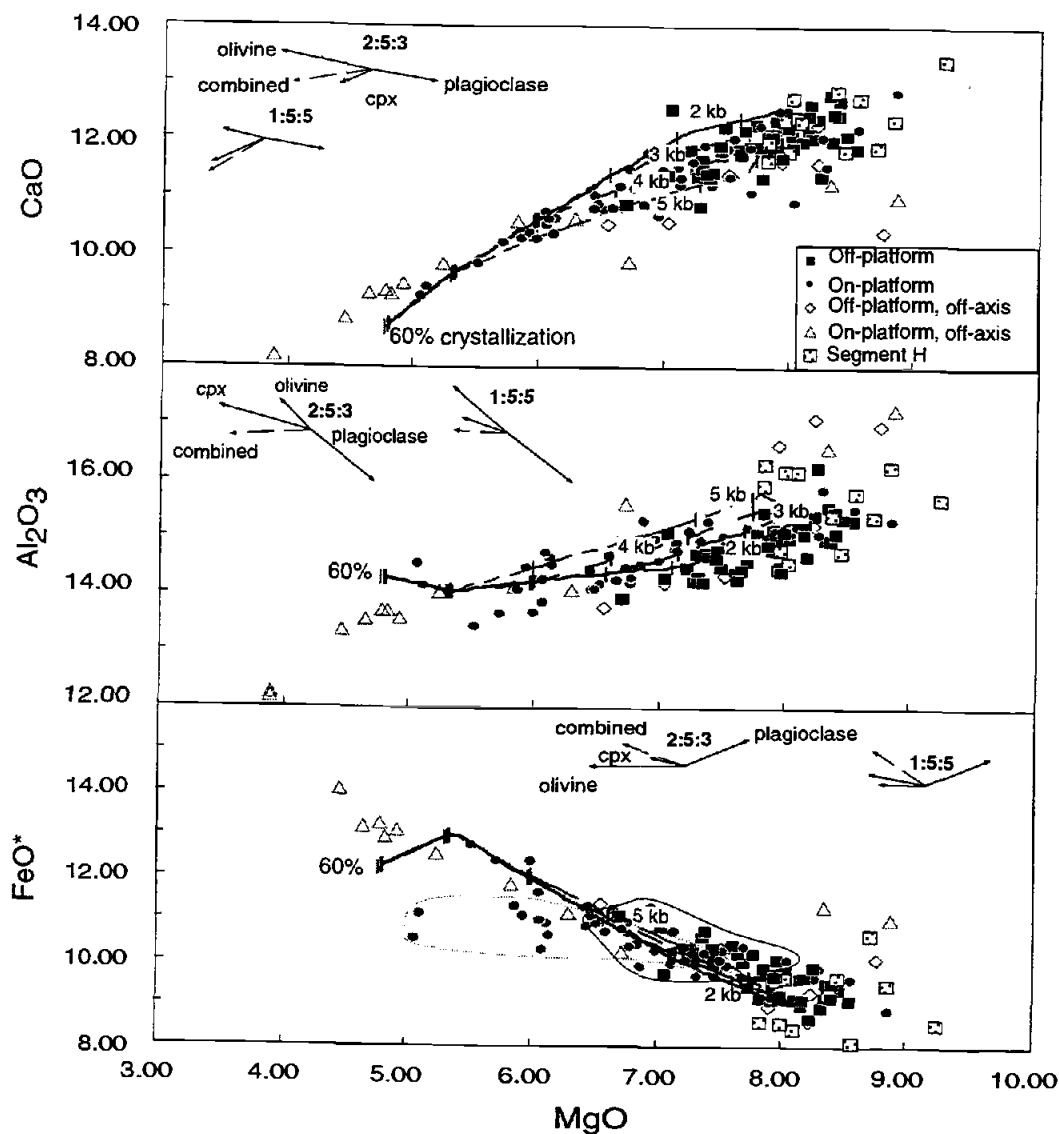


Figure 22: Polybaric fractional crystallization model. The ASP data is plotted with the LLD predicted by the COMAGMAT program of Ariskin et al. (1993). The starting composition used is a primitive composition from segment K, and the models were run at the FMQ buffer. There are four LLD on each plot: 2, 3, 4 and 5 kb. Each pressure is labeled individually except on the plots where it is difficult to distinguish between the four pressures (i.e. on the TiO_2 diagram). The models are for 60% crystallization and the tick marks on the LLD represent 10% crystallization increments. Proportional crystallization vectors for olivine, plagioclase and clinopyroxene, and the simultaneous crystallization of all three phases are shown in the corner of each plot. Two crystallization proportions were used, 1:1:5, and 2:5:3, for ol:plag:cpx, respectively. The first proportions are suitable for low pressure crystallization, while the second are more appropriate for higher pressure crystallization.

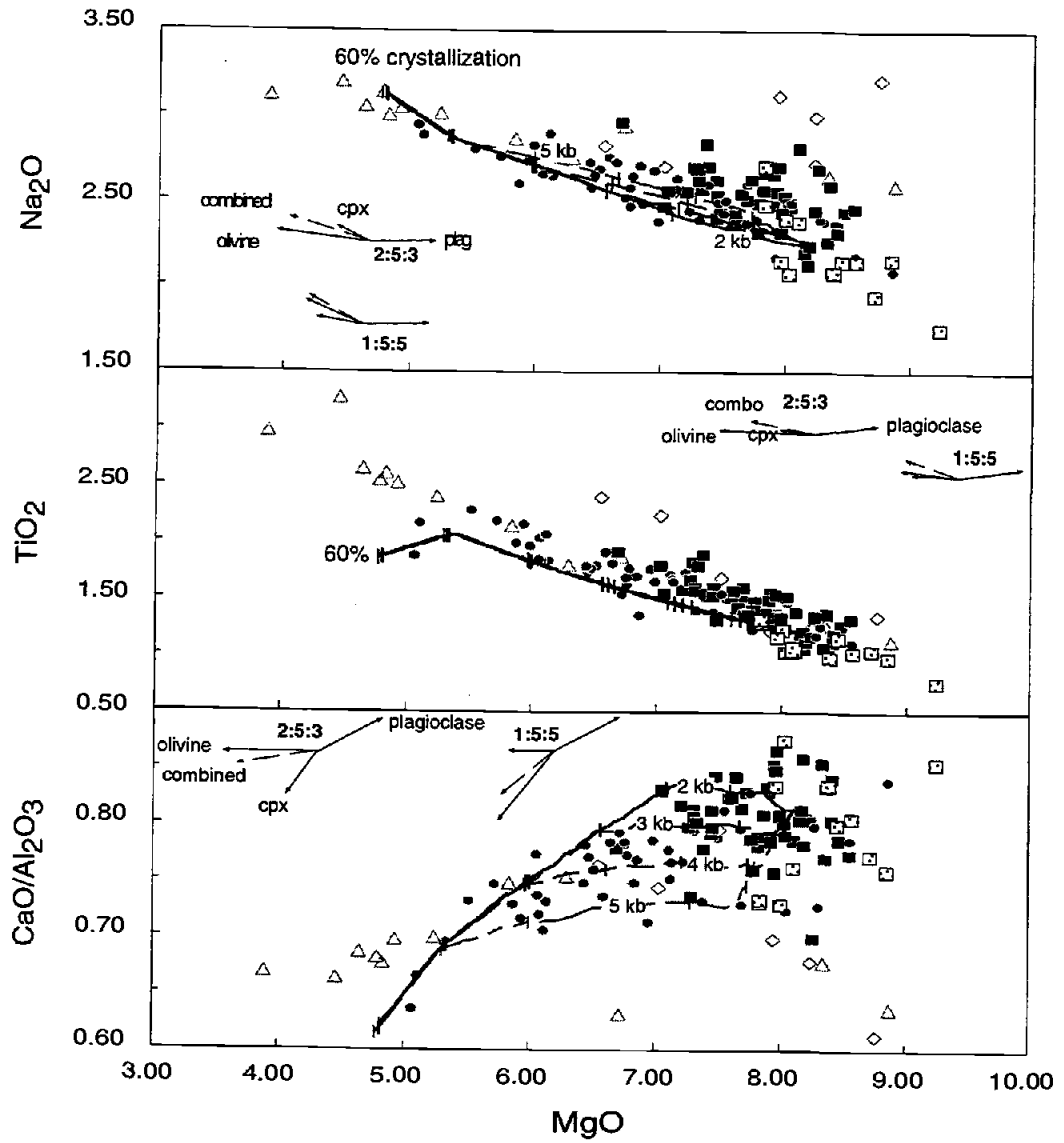


Figure 22 continued.

Somewhat surprisingly there does not seem to be an obvious difference between the crystallization pressure of models which fit ridge segments on and off the platform. There is some variation in the quality of the model fit to the on- versus off-platform samples (e.g. Na_2O), but this is more likely related to the parental magma being of slightly different composition than a difference in crystallization pressure.

Figure 22 includes proportional vector crystallization diagrams for olivine, plagioclase, clinopyroxene, and the simultaneous crystallization of all three phases. Two different crystallization proportions were used, 1:1:5, and 2:5:3, for ol:plag:cpx, respectively. The first proportions are suitable for low pressure crystallization, while the second are more appropriate for higher pressure crystallization. Overall, the most common general trend of the on-axis ASP data is along the three phase crystallization vector (marked as combination), or in between the three phase vector and the clinopyroxene crystallization vector, suggesting that three phase saturation is commonplace in these lavas. On the MgO vs. CaO plot (Figure 22) the overall trend of the data appears to be dominated by clinopyroxene crystallization while the dispersion at higher MgO, reflects the crystallization of ol \pm plag. On the MgO vs. $\text{CaO}/\text{Al}_2\text{O}_3$ plot (Figure 22) the off-platform samples trend between olivine and plagioclase while the platform samples fall on the three phase crystallization trend. Although there is this distinction between two and three phase crystallization, overall the ASP data lies close to a single general LLD trend, suggesting that the on-platform lavas are following the same path as the off-platform lavas but are simply more evolved. Scheirer et al. (1997) have suggested that the crustal thickness beneath the ASP platform may be twice that of the surrounding ridge axis. If so, the magmas beneath the platform must spend more time moving through the crust before eruption than those magmas away from the platform, allowing more extensive fractionation to occur.

The crystallization trends of segments I2 and J1 are also worth noting. On the MgO vs. FeO^* plot the crystallization trend for segment I2 is intermediate between

olivine and clinopyroxene. J1 also has a slightly more horizontal trend suggesting a stronger olivine/clinopyroxene influence than the rest of the ASP data set. Segments I2 and J1 are adjacent, and may be experiencing more olivine/clinopyroxene and less plagioclase crystallization than other segments. Although with the model used the pressure differences between segments are not resolvable, it is reasonable to suggest that the crystallization pressures are slightly higher beneath the platform, allowing for larger amounts of olivine/clinopyroxene crystallization and lesser amounts of plagioclase crystallization.

Distribution of Plume Material

On a whole, the distribution of N-MORB and E-MORB along-axis in the ASP region (Figures 6 and 7) is consistent with the location of the hotspot just southwest of the ridge. Most basalts atop the ASP platform are E-MORB ($K_2O/TiO_2 \geq 0.14$), while most basalts off-platform are N-MORB ($K_2O/TiO_2 \leq 0.11$). Those segments closest to the hotspot are the most enriched. However on closer examination, the distribution of plume material is more complex as evidenced by the over-enrichment found on segments H and I2. Segment H seems to have the strongest hotspot signal, based on the level of enrichment of the trace (Johnson et al., 1996) and minor elements (Figures 6, 7 and 9), and $^3He/^4He$ ratios (Graham et al., in prep). Gravity analysis also suggests that the influence of the ASP hotspot at depth extends further to the north than would be inferred from the sharp down step in topography at the northwest end of segment I1 (Figure 3, Scheirer et al., 1997). The geochemical variation of segment I2, as seen in Figures 7 and 9, is intermediate between the over-enriched trend of segment H and the

enriched trend of segments I1, J1, and J2. Whatever the process of over-enrichment affecting segment H, it has also affected segment I2 but to a lesser degree.

An intriguing question is why the geochemical peak is bimodal, occurring on both I2 and H, yet not as strongly on I1 (Figure 23)? How is it that I1 is "left out"? Qualitatively it seems that mixing is occurring between a depleted N-MORB source and an enriched plume source, with variations in the extent or thoroughness of mixing. Enrichment decreases from the northwest end of segment I2 towards I1. Although the K_2O/TiO_2 values of I1 are lower than those on I2, neither segment has samples with low K_2O/TiO_2 values. On segment H however samples with low K_2O/TiO_2 are present, at both the southeast and northwest ends of the segment. The lowest K_2O/TiO_2 value along-axis is found at the southeast end of segment H while the highest K_2O/TiO_2 value along-axis is in the center of segment H. Because mixing has not been thorough on segment H, depleted lavas and over-enriched lavas are both erupted along the segment. Segment I1 lavas appears to have undergone a more thorough mixing of the depleted and the enriched plume components, producing lavas that are enriched in incompatible elements with respect to N-MORB, but not to the same level as on segment H. Segment I2 lavas also seems more thoroughly mixed than H lavas, having no low K_2O/TiO_2 values, however mixing hasn't been as complete as on I1 as evidenced by the higher K_2O/TiO_2 values of segment I2. This contention is supported by the changing levels of diversity between these three segments. The range of compositions for segment I1 lavas is relatively small (i.e. $K_2O/TiO_2 = 0.16 - 0.19$), segment H lavas show a much larger range ($K_2O/TiO_2 = 0.06 - 0.54$), and segment I2 lavas show a range intermediate to that of I1 and H ($K_2O/TiO_2 = 0.19 - 0.43$).

To further examine a mixing scenario, fractionation-corrected minor elements were used. Their ratios may provide good tracers of mantle source differences. Covariations between K8, P8 and Ti8 are shown in Figure 24. On the diagram of K8

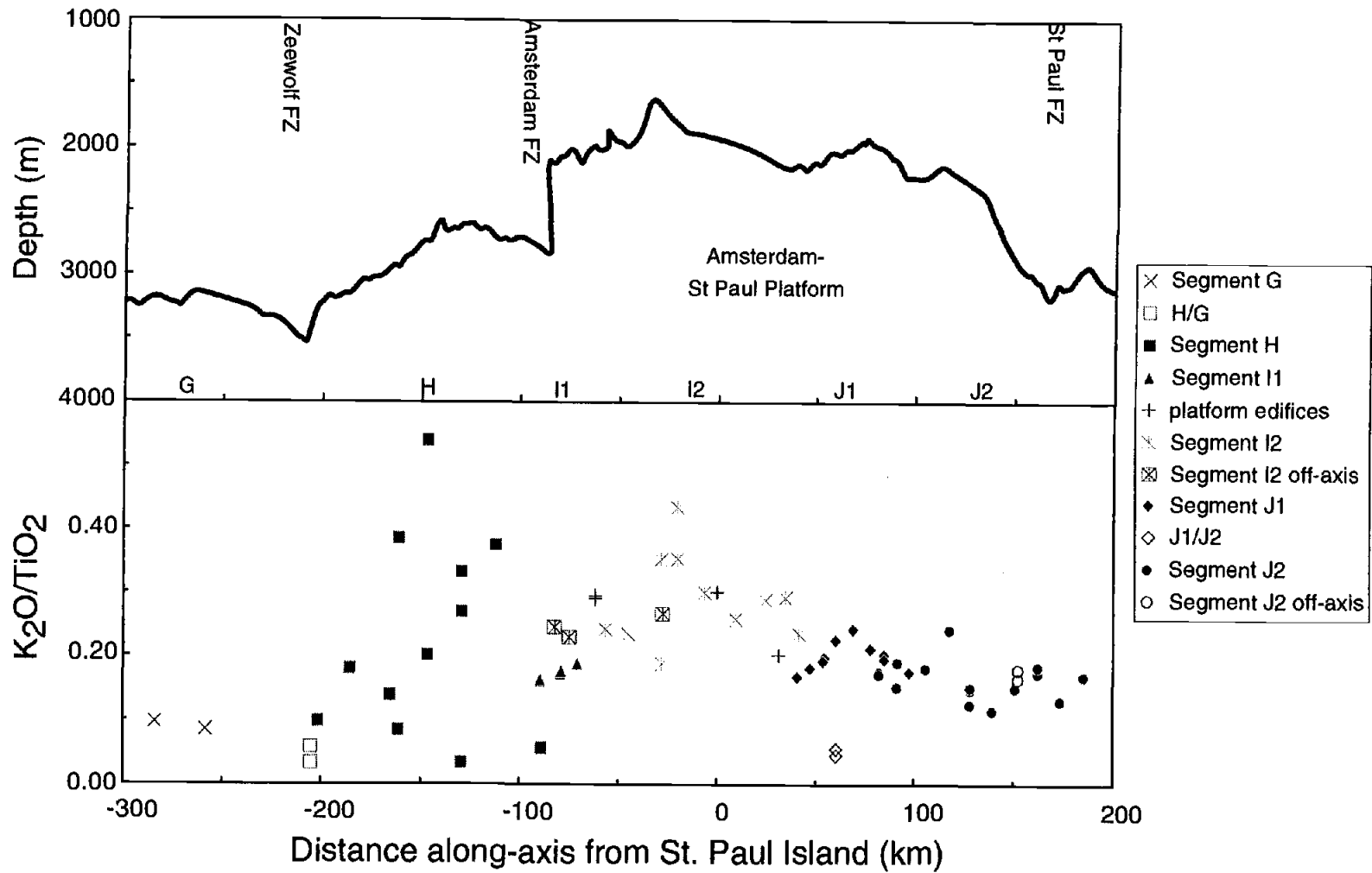


Figure 23: Variation of K_2O/TiO_2 in the area of the ASP platform.

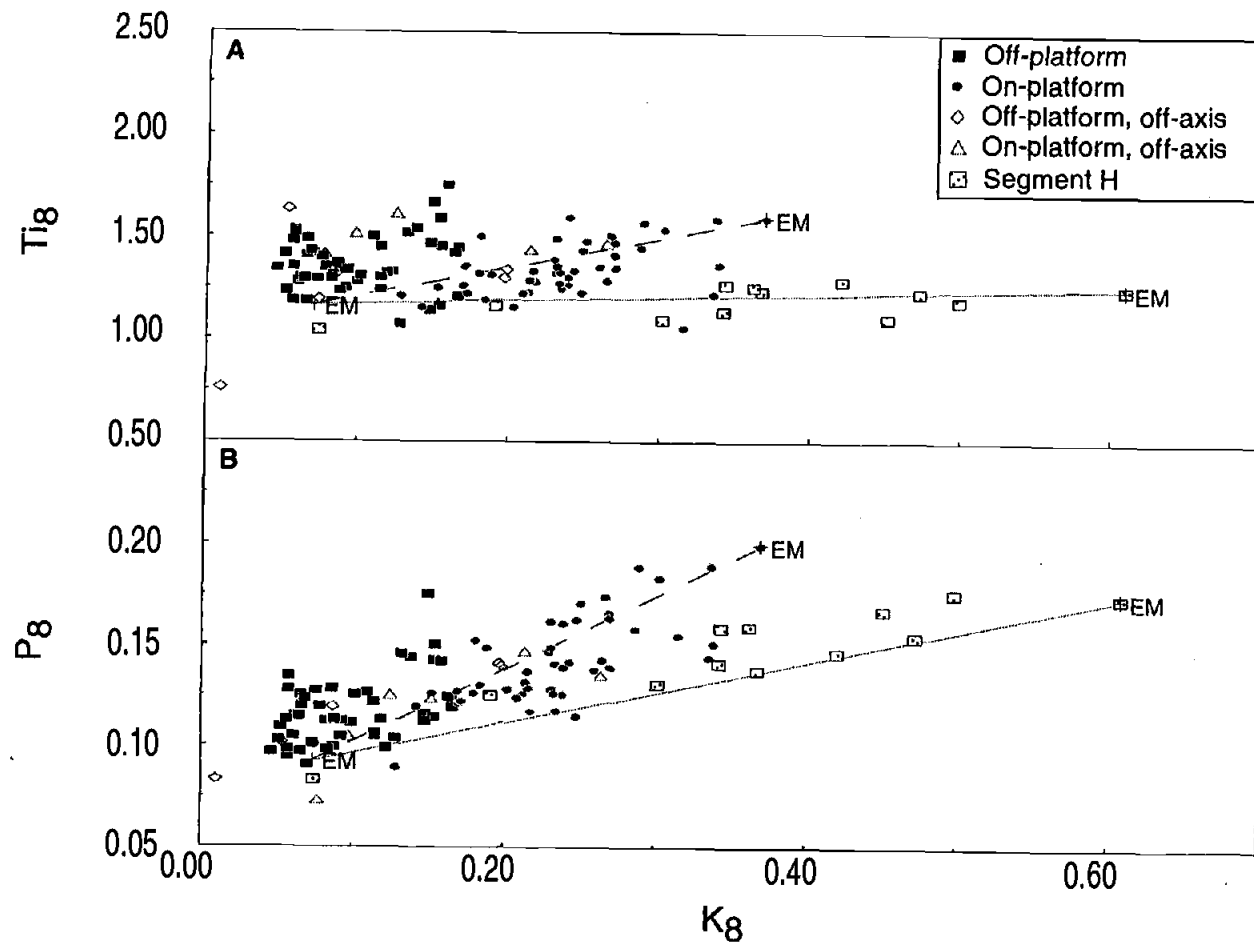


Figure 24: Covariation of fractionation-corrected minor elements. A) K_8 vs. Ti_8 . B) K_8 vs. P_8 . C) Ti_8 vs. P_8 . The lines are mixing lines between the three end members as described in the text. Each end member is indicated by EM. The dashed line is the mixing line between the depleted end member and the enriched end member. The solid line is the mixing line between the depleted end member and the over-enriched end member.

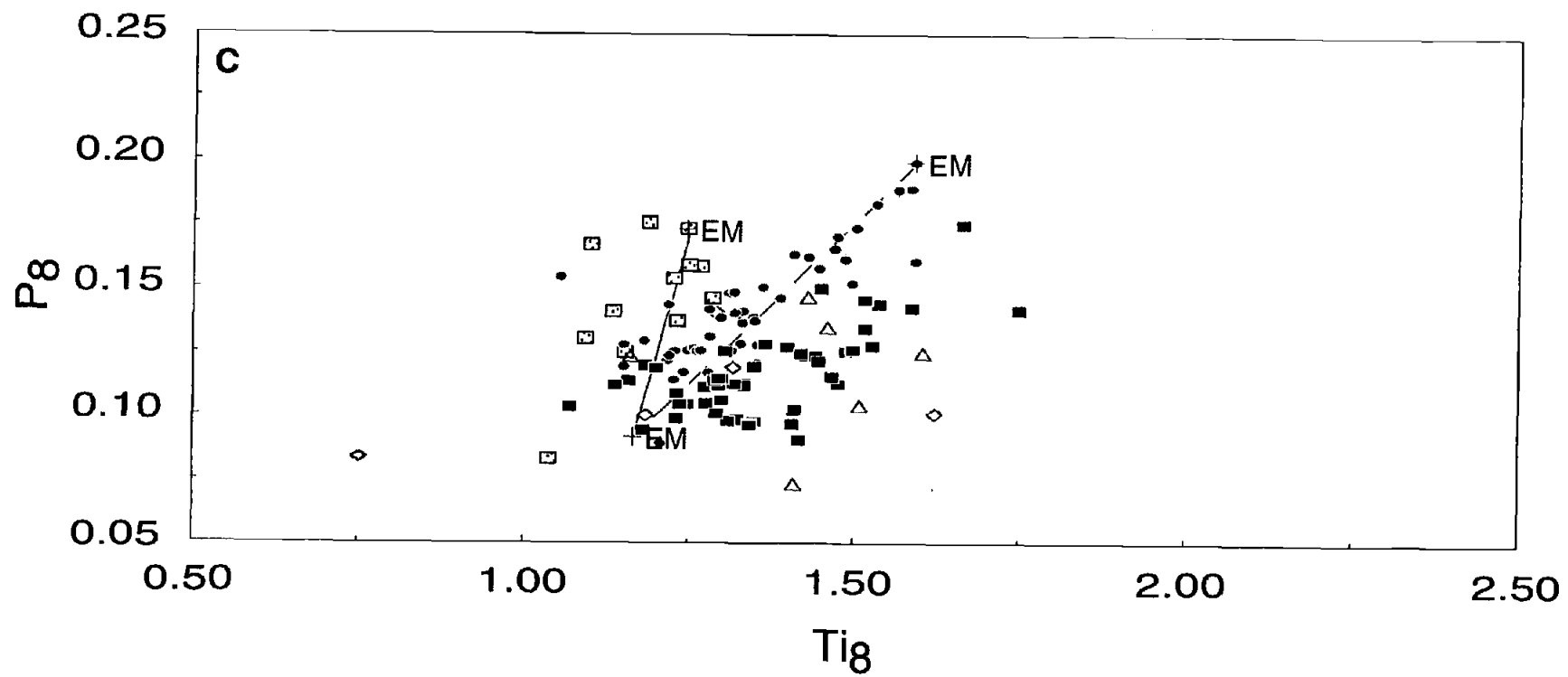


Figure 24 continued.

vs. Tig the trend of the ASP data is somewhat horizontal, with only a small amount of variation in Tig values within the data set and wide range of Kg. Segment H has slightly lower Tig values than either the on- or off-platform samples. As in the case of the uncorrected oxides, Tig is behaving more compatibly than Kg. Kg and P8 show a better positive correlation, with P8 showing slightly more compatible behavior than Kg. There is a clear separation on the Kg - P8 diagram between the on-platform, off-platform, and segment H samples. The samples with the lowest Kg and P8 values are those to the southeast of the platform (segments L, K, and J4). The samples from atop the platform have both higher Kg and P8 values. Segment H spans a large range of values, with both high and low Kg and P8 values. In general samples from atop the platform have higher P8 values than those of segment H. On the Tig - P8 diagram there is more scatter but the Tig and P8 of the on-platform samples are positively correlated, and Tig is more compatible than P8. To summarize then, of the three elements, Tig is the most compatible, and Kg is the least compatible. Kg has the largest range of values, and there are clear separations between the Kg values of on-platform, off-platform and segment H. In contrast, Tig has a very limited range of values, although a distinction still can be made between the Tig of segment H and the Tig of the remaining ASP data set. There is also a range of P8 values within the data set, with visible separations between segment H and the on- and off-platform samples, although not as large as Kg. The separation of data is further demonstrated on the ratio plots of Figure 25. Off-platform samples have the lowest P8/Tig, Kg/Tig and Kg/P8 values, while segment H samples have the highest.

Binary mixing lines between a "depleted end member" and an "over-enriched end member" have been included in Figures 24 and 25. The depleted end member has low Kg, low P8 and low Tig, and the composition is the average of an N-MORB from

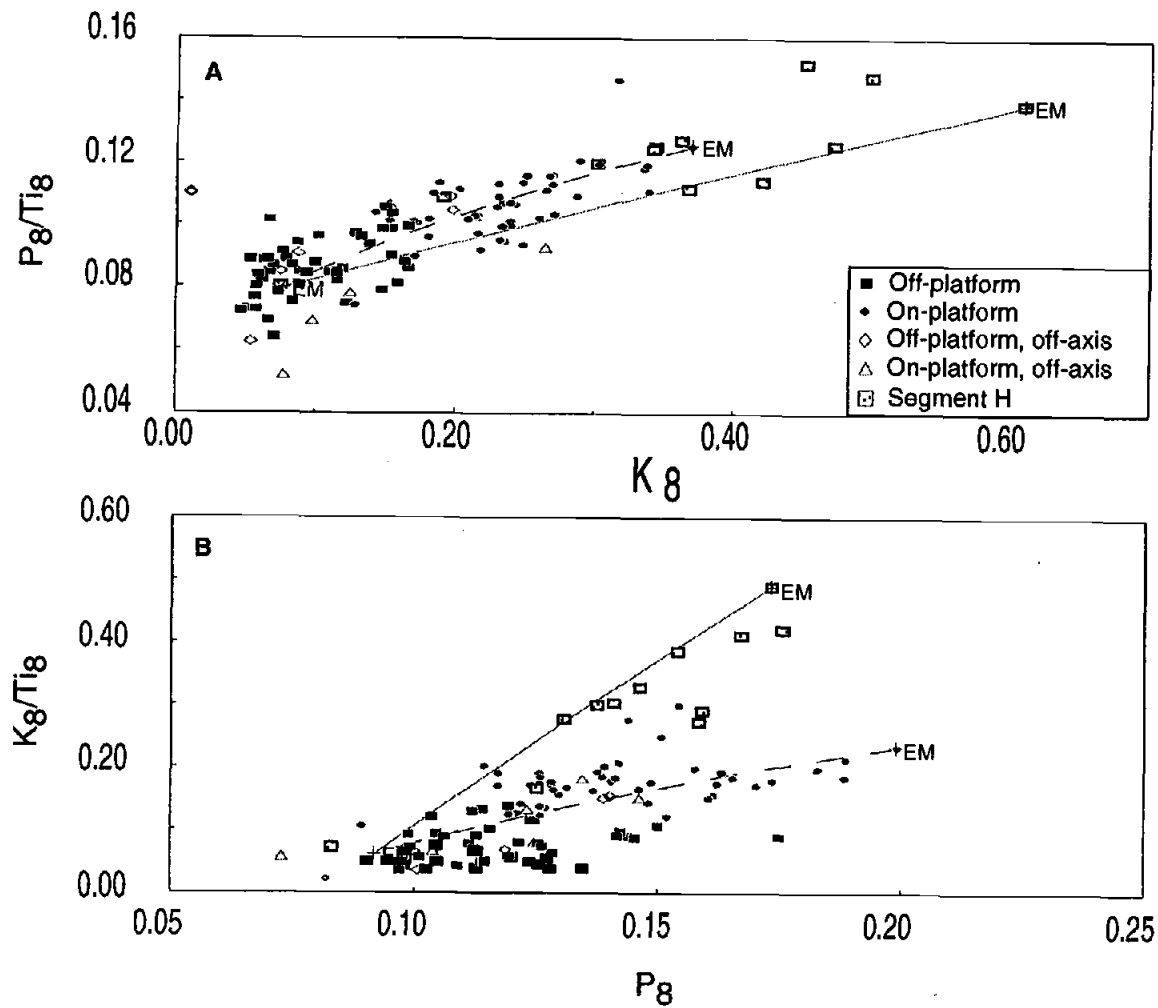


Figure 25: Fractionation-corrected minor element ratios. A) K_8 vs. P_8/Ti_8 . B) P_8 vs. K_8/Ti_8 . C) Ti_8 vs. K_8/P_8 . D) K_8/Ti_8 vs. P_8/Ti_8 . Symbols and mixing lines as in Figure 24.

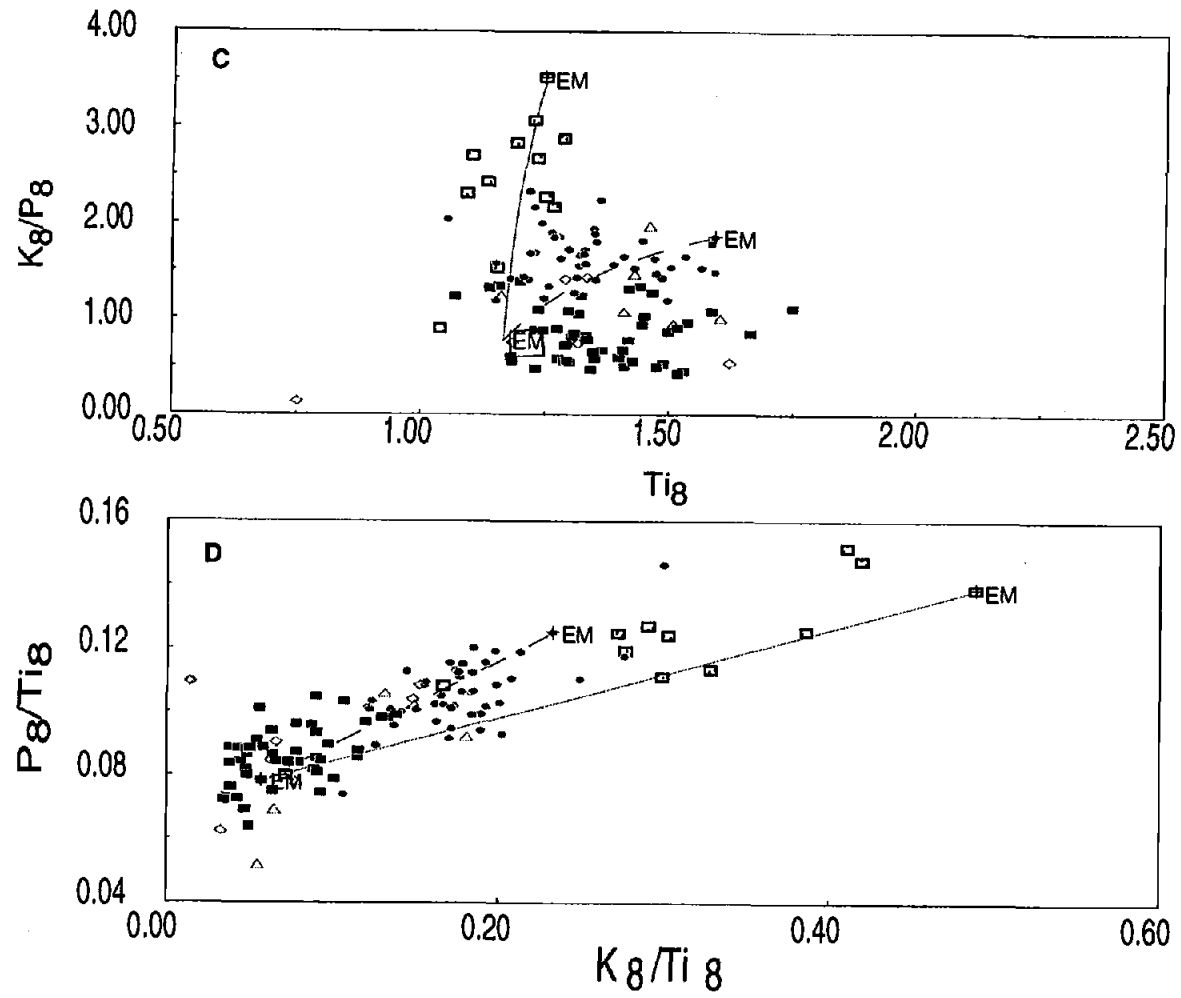


Figure 25 continued.

segment H (sample D72) and a N-MORB from segment K (D39). The over-enriched end member (sample W47) has high K₈, high P₈, and a Ti₈ content similar to the depleted end member. Binary mixing of these two end members alone does not seem to account for the range of the ASP data, and so a third, "enriched end member" (D59) has also been included. This third end member has higher P₈ and Ti₈, and lower K₈ than the over-enriched end member.

The three component mixing system shown does not wholly explain the range of ASP data (Figures 24 and 25). To examine the possibility that binary mixing plus the melting of one of these end members could explain the ASP data, the melting trajectory of a primitive mantle composition was calculated. The primitive mantle composition of Sun and McDonough (1989) was chosen as an arbitrary reference point. Liquid compositions determined for batch melting and aggregated fractional melting of spinel peridotite are illustrated on Figure 26. Instantaneous melt compositions have not been included on the diagram, but the composition of the instantaneous melt forms a similar trend to the batch and aggregate melts, with more extreme values. The batch melting model shown is for 7 - 21% melting, and the aggregated fractional melting model for 8 - 20%. The modes and partition coefficients used are shown in Table 4.

On the plot of K₈ vs. Ti₈ of Figure 24, there is a wide range of K₈ values, and a limited range of Ti₈ values. Binary mixing fails to explain the data; a three component system covers more of the data but still not completely. The Ti₈ values of the off-platform samples and some of the on-platform samples are higher than explainable by the mixing of these three components. Melting will increase the Ti₈ in a direction that can account for the Ti₈ values of the platform lavas (Figure 26a). On this diagram melting clearly does not explain the range of compositions seen in segment H lavas. The Ti₈ values of segment H remain too constant and the K₈ values of segment H lavas are too high. If the segment H lavas were to be explained by melting on this diagram it

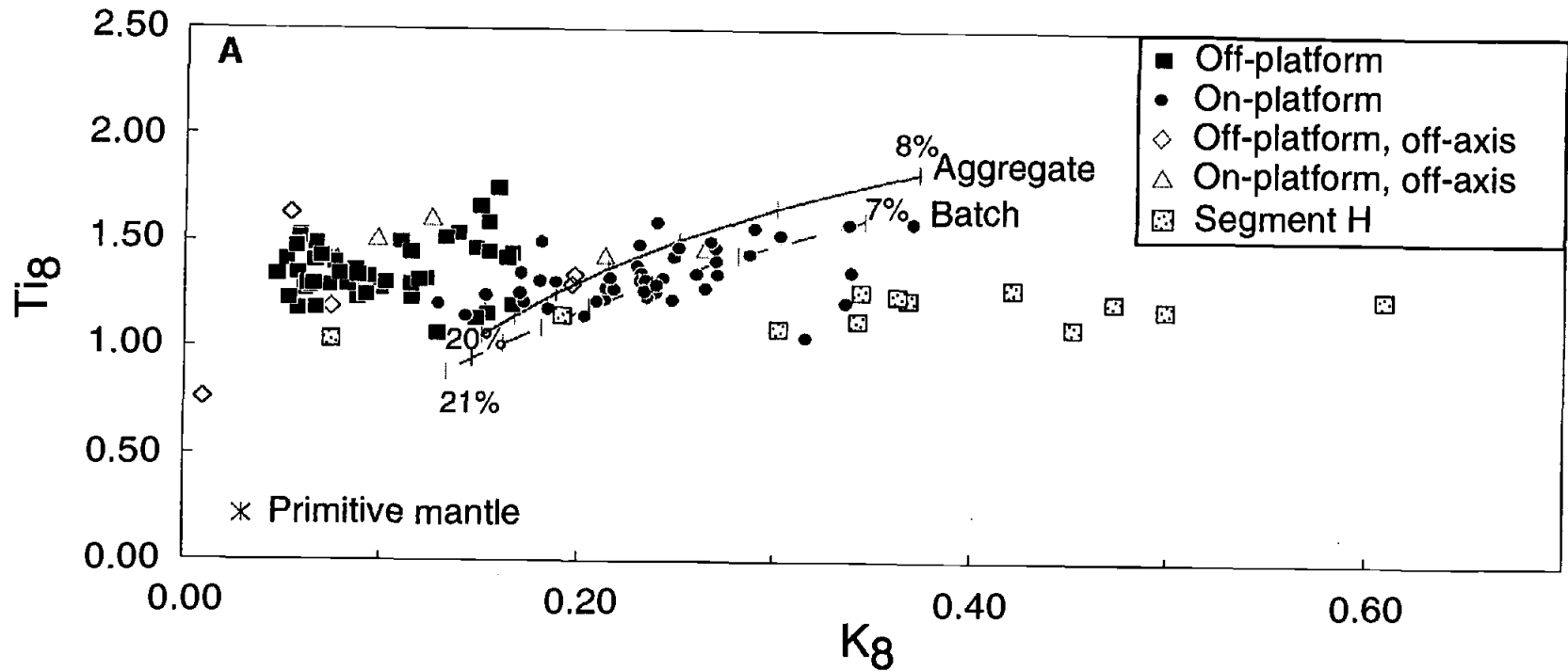


Figure 26: Melting model of ASP data. A) K_8 vs. Ti_8 . B) K_8 vs. P_8 . C) Ti_8 vs. P_8 . D) Ti_8 vs. K_8/P_8 . E) K_8 vs. P_8/Ti_8 . F) P_8 vs. K_8/Ti_8 . G) K_8/Ti_8 vs. P_8/Ti_8 . The asterisk represents the primitive mantle composition. The models shown are for a batch melt (dashed line) and an aggregated fractional melt (solid line) of a primitive MORB composition ($K = 250$ ppm, $P = 95$ ppm, $Ti = 1300$ ppm, Sun and McDonough, 1989). The melting models have ticks for melting increments of 2%. For batch melting the range of melting is between 7 and 21%. On the fractional melting model the range is between 8 and 20%. Figures 26d-f include a binary mixing line (alternating dashes) between the depleted end member and the over-enriched end member as described in the text.

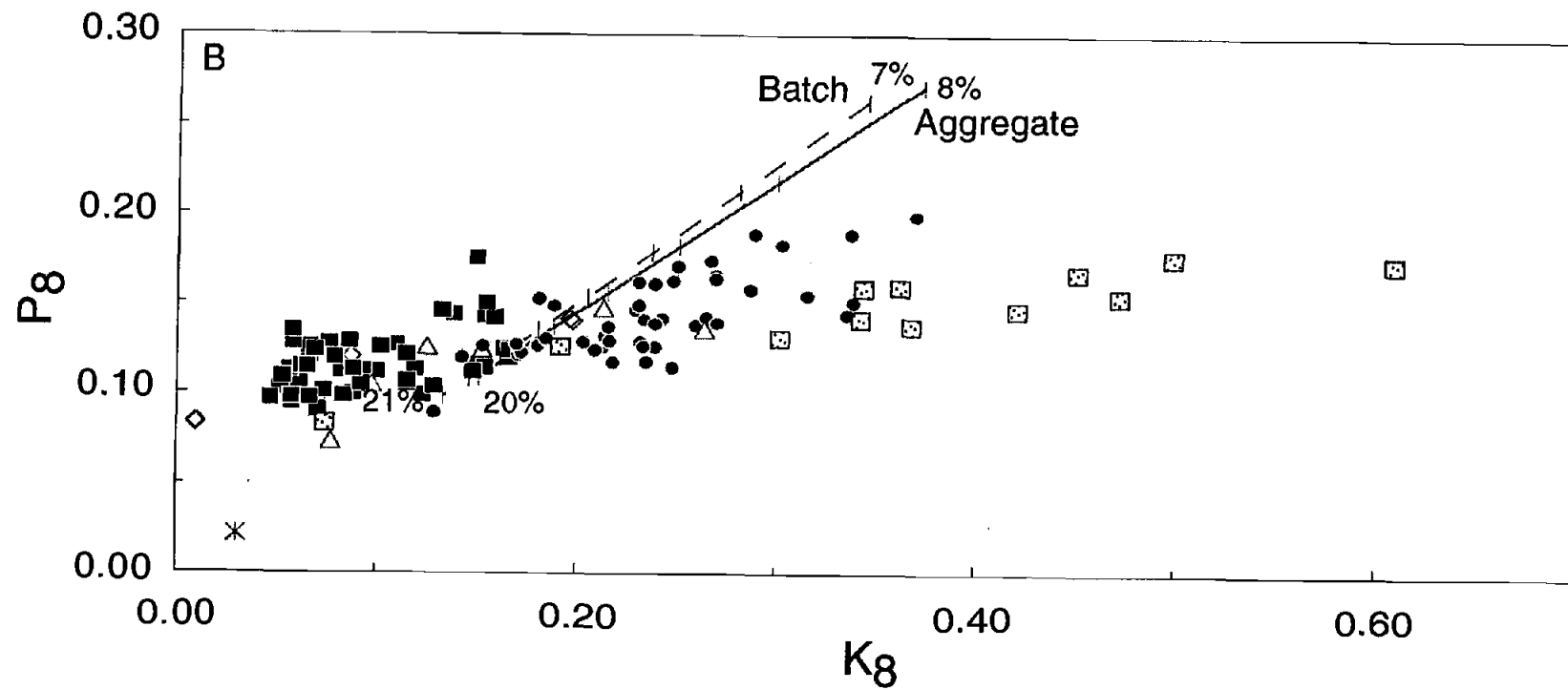


Figure 26 continued.

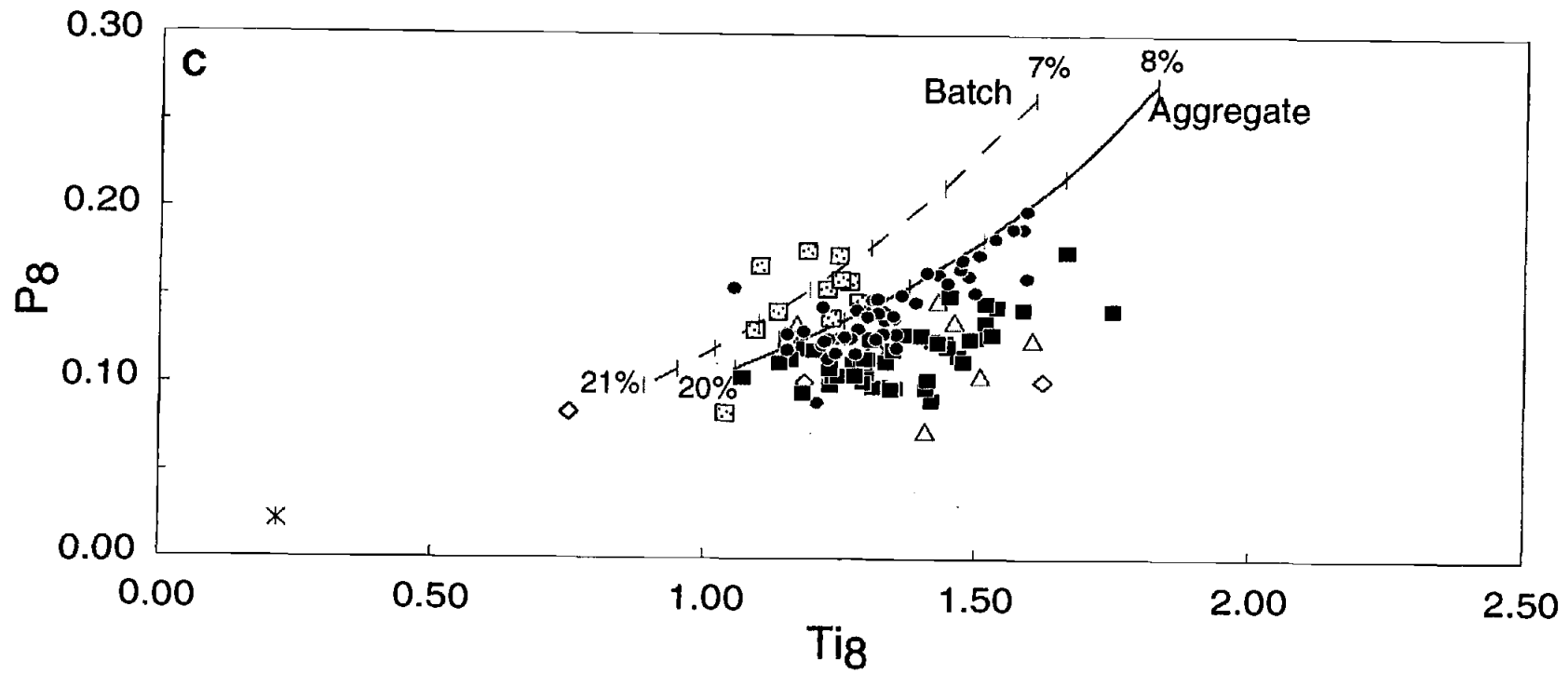


Figure 26 continued.

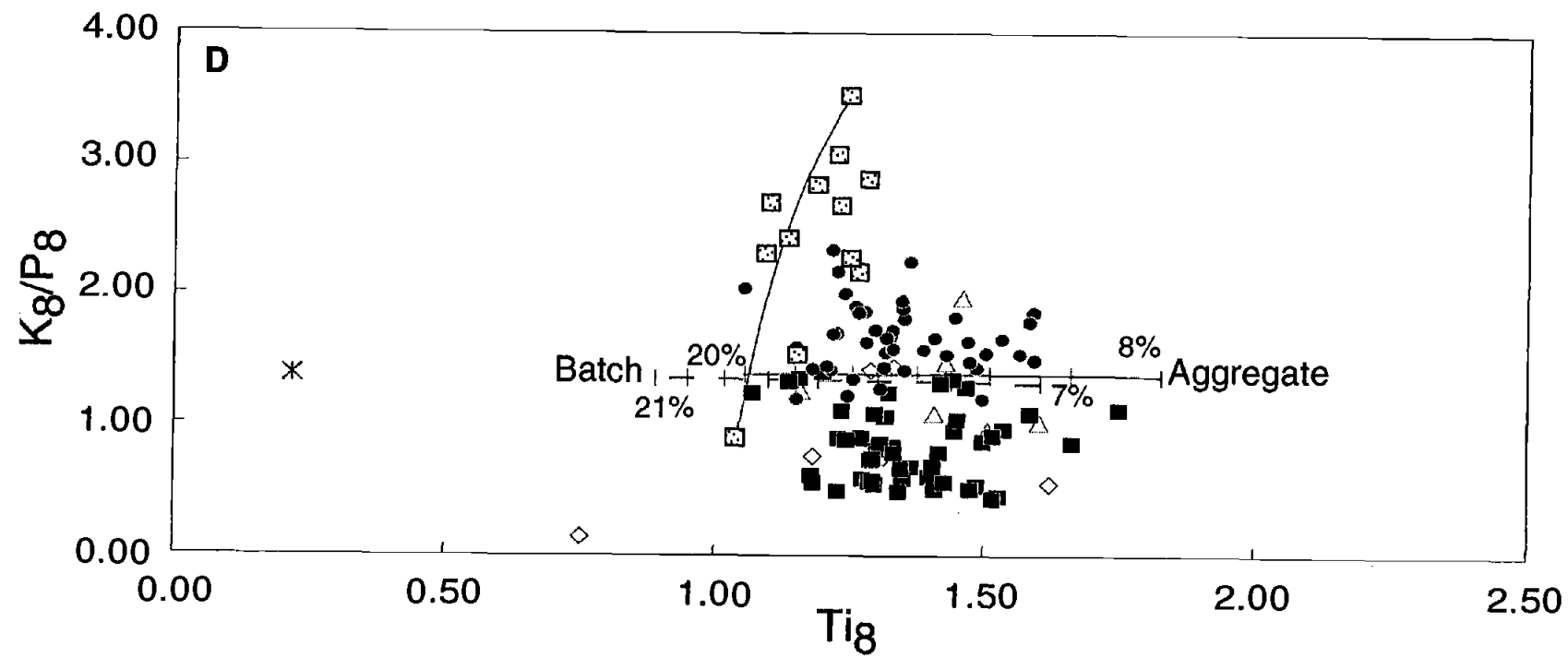


Figure 26 continued.

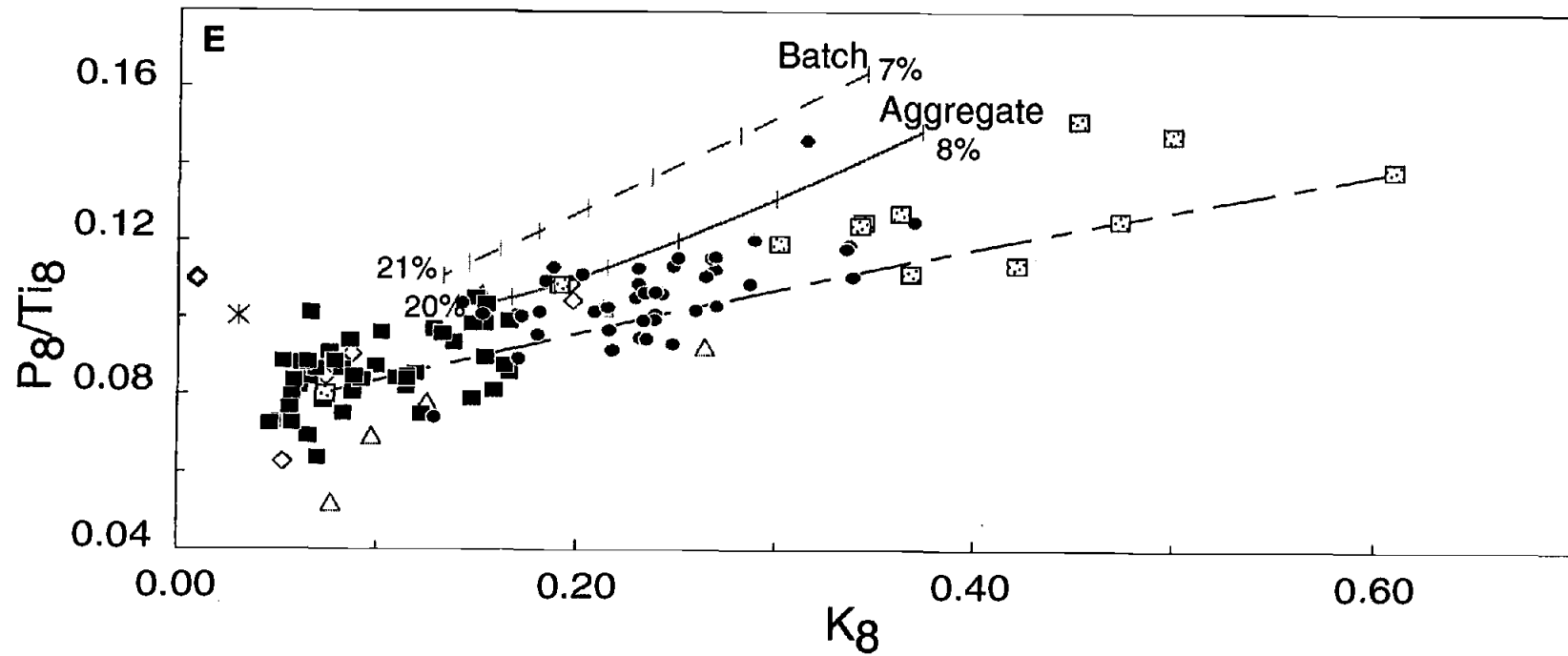


Figure 26 continued.

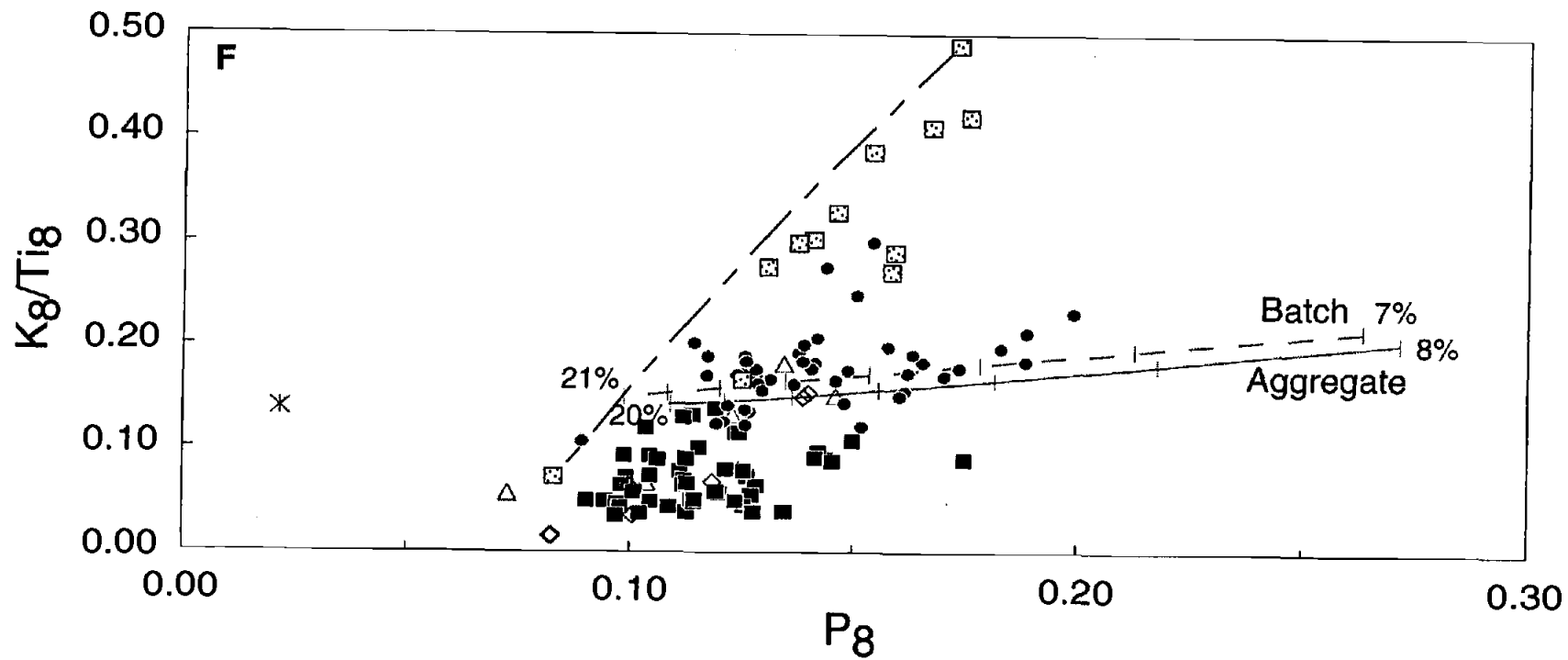


Figure 26 continued.

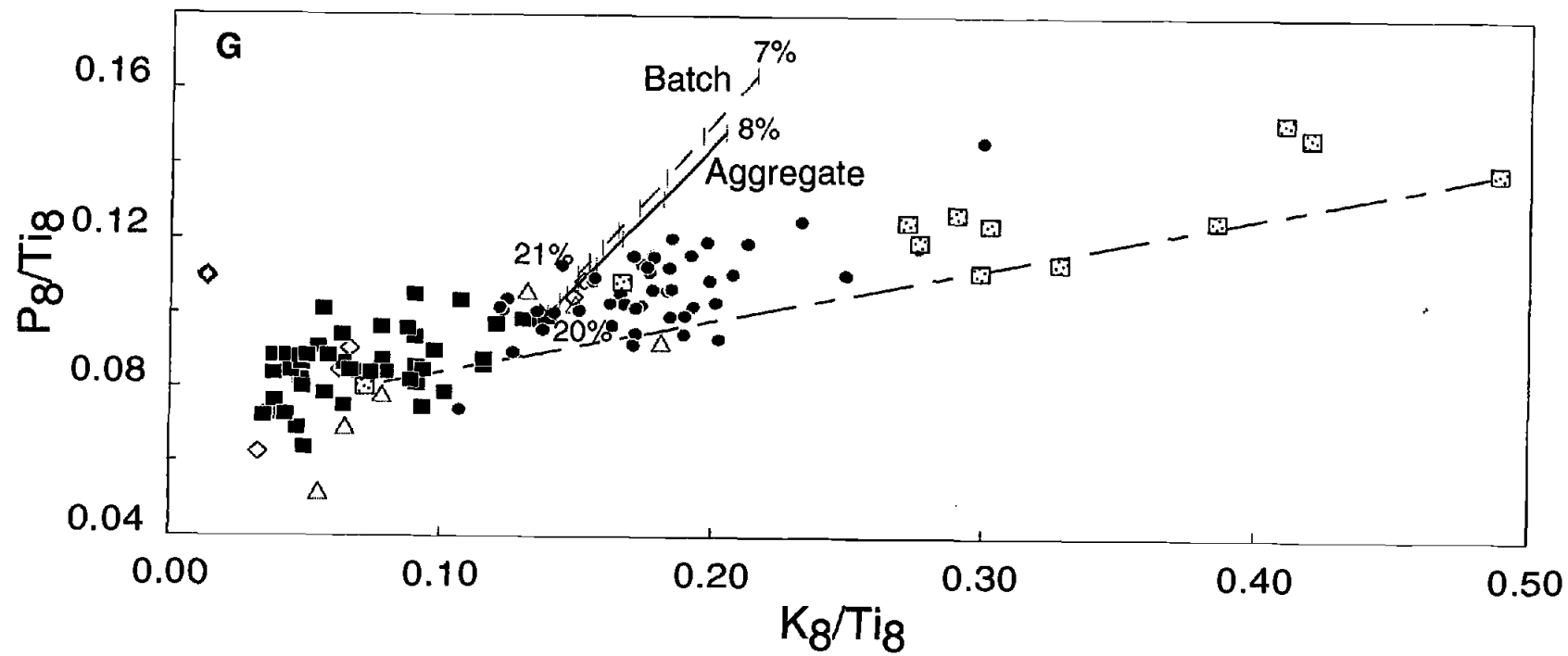


Figure 26 continued.

Table 4: Partition coefficients and modes used in the melting model. References for the partition coefficients are as follows. For olivine, P (Ulmer, 1989), K (Ohanti, 1989), Ti (Bougalt and Hekinian, 1974). For orthopyroxene, P (Ulmer, 1989), K (Kelemen and Dunn, 1992), Ti (McKenzie and O'Nions, 1991). For clinopyroxene, P (Baker and Wyllie, 1992), K (Kelemen and Dunn, 1992), Ti (Dunn, 1987). For spinel, P and K (R. Nielsen, pers. comm.), Ti (McKenzie and O'Nions, 1991).

	K	P	Ti	(wt. %) Solid mode	(wt. %) Melting mode
olivine	0.03	0.01	0.037	0.551	0.05
orthopyroxene	0.0003	0.03	0.024	0.247	0.298
clinopyroxene	0.007	0.0044	0.35	0.148	0.596
spinel	0.00001	0.00001	0.048	0.055	0.055

would require the melting of a heterogeneous source with a wide range of K_2O values and essentially unchanging TiO_2 values. The off-platform lavas are also unexplained by melting from the initial primitive mantle composition. However, the mantle composition of Sun and McDonough is a relatively enriched composition, not depleted, and if a slightly more depleted mantle composition were used, the melting trajectory would pass through the off-platform lavas.

On the K_8 vs. P_8 diagram (Figure 26b) again segment H is not explained by any calculated melting trajectory. Melting increases the P_2O_5 to much higher values than seen on segment H, while failing to increase the K_2O enough. The melting lines do not fit the platform data on this diagram (as they do in Figure 26a), but rather melting increases the P_8 and K_8 almost equally. However, the platform lavas, while having a range of P_8 contents explainable by melting, are clearly enriched with respect to K_8 , having more K_8 than explainable by melting.

The platform lavas fall very nicely along the melting trajectory when Ti_8 and P_8 are plotted (Figure 26c). The melting trajectory of a mantle composition more depleted than the primitive mantle of Sun and McDonough (1989) would pass directly through the off-platform lavas. The segment H lavas could possibly be explained by the melting of a heterogeneous mantle source with constant TiO_2 as explained in reference to the K_8 vs. Ti_8 diagram although it is difficult to completely understand the origin of such a mantle source.

The separation of data on the Ti_8 vs. K_8/P_8 diagram is quite distinct. Melting will increase the Ti_8 but will not change the K_8/P_8 ratio of the lavas (Figure 26d). Included on Figures 26d-f is a binary mixing line between the over-enriched end member and the composite depleted end member. The mixing line on Figure 26d can explain a portion of the data, but not all of the data. Overall the segment H lavas fall nicely along the binary mixing line with a spread in Ti_8 that may be attributed to

melting. The spread of the on-platform lavas seems to involve both the melting and mixing with the over-enriched source to create the range of K₈/P₈ values seen.

Melting increases the P₈/Ti₈ ratio of the magmas (Figure 26e and g). On its own, the diagram of K₈ vs. P₈/Ti₈ (Figure 26e) seems to suggest that the genesis of segment H lavas may be a result of melting, but examination of the other diagrams shows that this is not possible. Here again the melting trajectories fail to move directly through the platform lavas as the result of the lavas having higher K₈ contents than dictated by melting. The K₂O/TiO₂ ratio increases only slightly during melting, while the P₂O₅ increases significantly (Figure 26f). The range of K₈/Ti₈ values seen on segment H are unexplainable by melting of a homogenous source, even if it is over-enriched. Melting will produce the horizontal spread that is seen in both the on- and off-platform lavas, although two sources with different levels of enrichment, both depleted and enriched, are necessary. Notably a few samples from segment I2 fall close to the segment H lavas. Remember that segment I2 is the segment that in previous minor element diagrams (i.e. Figure 9) exhibited behavior intermediate between the over-enriched lavas and the enriched lavas. This may be a result of mixing between the enriched melt and the over-enriched source.

On the K₈/Ti₈ vs. P₈/Ti₈ (Figure 26g) diagram all of the ASP data falls approximately along the mixing line between the over-enriched end member and the depleted end member. However, the P₈/Ti₈ ratio is slightly higher than that provided by mixing alone, producing scatter in the data. As mentioned previously and as seen on Figure 26g, the P₈/Ti₈ ratio does increase relative to the starting composition during melting, which could provide an explanation for the scatter.

Overall the diagrams of Figure 26 demonstrate that 1) the melting of spinel peridotite is a feasible explanation for some of the range in the ASP data; 2) melting of a homogenous source, even if it is over-enriched, cannot explain the composition of

segment H lavas; and 3) both depleted and enriched mantle sources are necessary. It is possible that the enriched mantle source is the result of mixing between a depleted mantle source and an over-enriched mantle source, which is then melted. But it is just as likely that there are three distinct mantle sources, and distinguishing which in fact is occurring will require trace element and isotopic data and is beyond the scope of this discussion. In either case, melting of both a depleted mantle source and an enriched mantle source is necessary to explain the ASP data.

The question of why segment I2 and H are more enriched and over-enriched than segment I1 is not completely clear, but likely is explained by flow dynamics in the upper mantle. Scheirer et al. (1997) subdivide the ASP study region into three representative areas: off-platform (segments L, K, J4, H, G, F), on-platform (segments J1, I2, I1), and edge of platform (segments J3, J2). Important to the discussion here is the off-platform and on-platform categories. Scheirer et al. (1997) characterize the off-platform area as straight segments with small axial ridges (< 200 m relief) and valleys which are separated by long-lived (> several million years) ridge offsets. Off-axis seamounts are few, the neovolcanic zone is ridge-centered, abyssal hills are relatively large and the magnetic anomaly patterns are relatively simple. On the platform, the spreading axis is composed of shorter segments which are typically curved and have overlapping, *en echelon* offsets. Off-axis seamounts are more abundant, the neovolcanic zone is more complex than away from the platform, abyssal hills are smaller and the magnetic anomaly patterns are more complex. Off-axis patches of reflective seafloor (neovolcanic zone) in side-scan images are also common. Combined, these factors suggest that the influence of the ASP hotspot brings about a less stable plate boundary geometry (more rapid ridge jumps/propagation events), smaller faults, and more off-axis volcanism on-platform than seafloor spreading away from the platform (Scheirer et al., 1997). Perhaps these complexities can explain the bimodal geochemical peak. Segment H and I2 apparently receive a larger over-enriched

contribution than segment I1. If the confusion of the surficial features reflects complexities in mantle flow and melting beneath the ridge axis, perhaps the supply of magma, as well as the mixing of mantle and magmas in this region may also be somewhat sporadic or inefficient. The increased accessibility of the over-enriched plume material to segments H and I2, and not I1, as a result of channeled flow could explain the absence of the geochemical peak on I1.

Conclusions

The SEIR in the area of the ASP platform today continues to feel the effect of ridge-hotspot interaction, acting as a sink to draw in plume material and producing magmas with a hotspot influence. As in other hotspot regions, the major and minor element systematics in MORB from this region are affected by the presence of the ASP hotspot and its thermal effect on the surrounding mantle. Magmas along the ridge show long wavelength and segment-scale changes both in major and minor elements. As seen in some other hotspot regions (e.g. Galapagos, Langmuir et al., 1992) the ASP hotspot region has lower Fe₈, and higher Na₈ and CaO/Al₂O₃ than predicted by the global major element correlations. The ASP lavas fall intermediate to the 'local' and 'global' effects of Klein and Langmuir (1989). The low CaO/Al₂O₃ ratios atop the platform, and the positive covariation of Fe₈ and Na₈ in this same region, suggest this intermediate behavior may be related to high pressure clinopyroxene fractionation. There is some indication that high pressure clinopyroxene crystallization was also important in the generation of lavas near the center of the Galapagos Platform (Fisk et al., 1982).

In the ASP region the degree of fractionation increases from both the northwest and the southeast with the most evolved lavas atop the platform, similar to crystallization behavior observed in the Galapagos region (Fisk et al., 1982; Shilling et al., 1982). However, as compared to the low pressure crystallization of the Galapagos lavas (Fisk et al., 1982), polybaric crystallization near 4 kb best explains major element trends in the ASP data. Although crystallization pressure differences between on- and off-platform segments are not resolvable with the model used, it is reasonable to suggest that the crystallization pressures are slightly higher beneath the platform. Crystallization for the region as a whole may be occurring deeper than during normal generation of MORB elsewhere, and it is likely that high pressure crystallization of

clinopyroxene is occurring and dominating the crystallization paths of these lavas. Three phase saturation seems most common in these lavas, but in some cases slightly higher pressures of crystallization may result in the two phase crystallization of olivine and clinopyroxene.

Minor elements K_2O , P_2O_5 and to a lesser degree TiO_2 show large concentration spikes atop the platform, and in the case of K_2O and P_2O_5 these enrichments extend beyond the platform to include segment H. Segment H and to a lesser degree segment I2, show an excess level of enrichment, unexplainable by fractional crystallization, and described in this study as over-enriched. The Cl content of selected SEIR basalt glasses provides clear evidence that assimilation of crustal material has occurred during the development of some ASP lavas. Nevertheless, the over-enrichment on segments H and I2 is not related to assimilation of crustal material, securing the likelihood that the over-enrichment is hotspot related.

Binary mixing of a depleted end member and an over-enriched end member (associated with the hotspot) plus the melting of the depleted end member provide a plausible explanation for the variation in minor element compositions seen in this region.

Surprisingly the hotspot signal is strongest in segment H lavas, rather than in lavas from atop the platform, although platform segments are also enriched. The distribution of plume material is not uniform in this area. Trace elements and isotopic compositions will provide additional constraints on the mantle sources involved in magmatism, as well as provide further insight into the distribution of plume material, along this section of the SEIR.

Bibliography

- Ariskin, A.A., M.Y. Frenkal, G.S. Barmina, and R.L. Nielsen, COMAGMAT: A FORTRAN program to model magma differentiation processes, *Comp. and Geosci.*, 1993, 1155-1170, 1993.
- Baker, M.B. and P.J. Wyllie, High pressure apatite solubility in carbonate-rich liquids: Implications for mantle metasomatism, *Geochim. Cosmochim. Acta*, 56, 3409-3422, 1992.
- Bougalt, H., and R. Hekinian, Rift valley in the Atlantic Ocean near 36°50' N: Petrology and geochemistry of basaltic rocks, *Earth Planet. Sci. Lett.*, 24, 249-261, 1974.
- Byers, C.D., D.M. Christie, D.W. Muenow, and J.M. Sinton, Volatile contents and ferric-ferrous ratios of basalt, ferrobasalt, andesite, and rhyodacite glasses from the Galapagos 95.5°W propagating rift, *Geochim. Cosmochim. Acta*, 48, 2239-2245, 1984.
- Byers, C.D., D.W. Muenow, and M.O. Garcia, Volatiles in basalts and andesites from the Galapagos Spreading Center, 85°W to 86°W, *Geochim. Cosmochim. Acta*, 47, 1551-1558, 1983.
- Carroll, M.R., and M.J. Rutherford, Sulfur speciation in hydrous experimental glasses of varying oxidation state: Results from measured wavelength shifts of sulfur X-rays, *Amer. Mineral.*, 73, 845-849, 1988.
- Carroll, M.R., and J.D. Webster, Solubilities of sulfur, noble gases, nitrogen, chlorine and fluorine in magmas, in *Volatiles in Magmas, Reviews in Mineralogy*, vol. 30, edited by M.R. Carroll and J.R. Holloway, pp. 231-279, Mineral. Soc. Amer., 1994.
- Christie, D.M., D. Pyle, J.C. Sempéré, and J. Palmer, Petrologic diversity, axial morphology and magma supply at the AAD, *EOS Trans. AGU*, 71, 1388, 1990.
- Cochran, J.R., Systematic variations of axial morphology along the SEIR, *EOS Trans. AGU*, 72, 260, 1991.
- Czmanske, G.K., and J.G. Moore, Composition and phase chemistry of sulfide globules in basalt from the Mid-Atlantic Ridge near 37°N lat., *Geol. Soc. Amer. Bull.*, 88, 587-599, 1977.
- Dosso, L., H. Bougault, P. Beuzart, J.Y. Clavex, and J.L. Joron, The geochemical structure of the Southeast Indian Ridge, *Earth Planet. Sci. Lett.*, 88, 47-59, 1988.
- Douglas, L.M., D.W. Graham, K.T.M. Johnson, D.S. Scheirer, and D.W. Forsyth, Major element composition of basalt glasses along the SEIR in the vicinity of the ASP platform, *EOS Trans. AGU*, 77, F690, 1996.
- Dunn, T., Partitioning of Hf, Lu, Ti and Mn between olivine, clinopyroxene, and basaltic liquid. *Contrib. Mineral. Petrol.*, 96, 476-484, 1987.

- Dupré, B., and C.J. Allègre, Pb-Sr isotope variation in Indian Ocean basalts and mixing phenomena, *Nature*, 303, 142-146, 1983.
- Fisk, M.R., A.E. Bence, and J.G. Schilling, Major element chemistry of Galapagos Rift zone magmas and their phenocrysts, *Earth Planet. Sci. Lett.*, 61, 171-189, 1982.
- Fisk, M.R., K.T.M. Johnson, and J.C. Alt, Effect of assimilation of altered oceanic crust on magma chemistry: An experimental study, in *Proc. of ODP Sci. Results*, vol. 137/140, edited by J. Erzinger, K. Becker, H.J.B. Dick, and L.B. Stokking, pp. 43-51, ODP, College Station TX, 1995.
- Forsyth, D.W., R.L. Ehrenbard, and S. Chapin, Anomalous upper mantle beneath the AAD, *Earth Planet. Sci. Lett.*, 471-478, 1987.
- Graham, D.W., and J.E. Lupton, Helium isotope variations along mid-ocean ridges: Implications for magma history and mantle heterogeneity, *Goldschmidt Conf. Program Abstract*, A43, 1992.
- Graham, D.W., K.T.M. Johnson, L.M. Douglas, and J.E. Lupton, Hotspot-ridge interaction along the Southeast Indian Ridge near Amsterdam and St. Paul Islands: Helium isotope evidence, in prep., 1998.
- Gripp, A.E., and R.G. Gordon, Current plate velocities relative to the hotspots incorporating the NUVEL-1 global plate motion model, *Geophys. Res. Lett.*, 17, 1109-1112, 1990.
- Grove, T.L., R.J. Kinzler, and W.B. Bryan, Fractionation of mid-ocean ridge basalt (MORB), in *Mantle Flow and Melt Generation at Mid-Ocean Ridges*, *Geophys. Monogr. Ser.*, vol. 71, edited by J. Phipps-Morgan, D.K. Blackman, and J.M. Sinton, pp. 281-310, AGU, Washington DC, 1992.
- Hamelin, B., B. Dupré, and C.J. Allègre, Pb-Sr-Nd isotopic data of Indian Ocean ridges: New evidence of large-scale mapping of mantle heterogeneities, *Earth Planet. Sci. Lett.*, 76, 288-298, 1986.
- Haughton, D.R., P.L. Roeder, and B.J. Skinner, Solubility of sulfur in mafic magmas, *Econ. Geol.*, 69, 451-467, 1974.
- Ito, E., W.M. White, and C. Gopel, The O, Sr, Nd and Pb isotope geochemistry of MORB, *Chem. Geol.*, 62, 157-176, 1987.
- Jambon, A., B. Deruelle, G. Dreibus, and F. Pineau, Cl and Br abundance in MORB: The contrasting behavior of the MAR and the EPR and implications for the Cl geodynamic cycle, *Chem. Geol.*, 101-117, 1995.
- Jarosewich, E., J.A. Nelen and J.A. Norberg, Reference samples for electron microprobe analysis, *Geostandards Newsletter*, 4, 43-47, 1980.
- Johnson, K.T.M., L.M. Douglas, D.W. Graham, D.S. Scheirer, and D.W. Forsyth, Ridge-hotspot interaction on the SEIR near the Amsterdam-St. Paul Platform, *EOS Trans. AGU*, 77, F684, 1996.
- Katsura, T., and S. Nagshima, Solubility of sulfur in some magmas at 1-atm., *Geochim. Cosmochim. Acta*, 38, 517-531, 1974.

- Kelemen, P.B., and J.T. Dunn, Depletion of Nb relative to other highly incompatible elements by melt/rock reaction in the upper mantle, *EOS Trans. AGU*, 73, 656, 1992.
- Klein, E.M., and C.H. Langmuir, Global correlations of ocean ridge basalt chemistry with axial depth and crustal thickness, *J. Geophys. Res.*, 92, 8089-8115, 1987.
- Klein, E.M., and C.H. Langmuir, Local versus global variations in ocean ridge basalt composition: A reply, *J. Geophys. Res.*, 94, 4241-4252, 1989.
- Langmuir, C.H., J.F. Bender, A.E. Bence, and G.N. Hanson, Petrogenesis of basalts from the FAMOUS area: Mid-Atlantic Ridge, *Earth Planet. Sci. Lett.*, 36, 133-156, 1977.
- Langmuir, C.H., E.M. Klein, and T. Plank, Petrological systematics of mid-ocean ridge basalts: Constraints on melt generation beneath ocean ridges, in *Mantle Flow and Melt Generation at Mid-Ocean Ridges*, *Geophys. Monogr. Ser.*, vol. 71, edited by J. Phipps-Morgan, D.K. Blackman, and J.M. Sinton, pp. 183-280, AGU, Washington DC, 1992.
- Luhr, J.F., Experimental phase relations of water- and sulfur-saturated arc magmas and the 1982 eruptions of El Chichon volcano, *J. Petrol.*, 31, 1071-1114, 1990.
- Magenheim, A.J., Spivack, A.J., Michael, P.J., and J.M. Gieskes, Chlorine stable isotope composition of the oceanic crust: Implications for Earth's distribution of chlorine, *Earth and Plan. Sci. Lett.*, 131, 427-432, 1995.
- Marks, K.M., D.T. Sandwell, P.R. Vogt, and S.A. Hall, Mantle downwelling beneath the AAD zone: Evidence from geoid height versus topography, *Earth Planet. Sci. Lett.*, 103, 325-338, 1991.
- Mathez, E.A., Sulfur solubility and magmatic sulfides in submarine basalt glass, *J. Geophys. Res.*, 81, 4269-4276, 1976.
- McKenzie, D., and R.K. O'Nions, Partial melt distributions from inversion of REE concentrations, *J. Petrol.*, 32, 1021-1091, 1991.
- Melson, W.G., T.L. Vallier, T.L. Wright, G. Byerly, and J. Nelson, Chemical diversity of abyssal volcanic glass erupted along the Pacific, Atlantic and Indian Ocean seafloor spreading centers, in *The Geophysics of the Pacific Ocean Basin and its Margin*, *Geophys. Monogr. Ser.*, vol. 19, edited by G. Sutton, M.H. Manghnani, and R. Moberly, pp. 351-367, AGU, Washington DC, 1976.
- Michael, P.J., and W.C. Cornell, The influence of spreading rate and magma supply on crystallization and assimilation beneath mid-ocean ridges: Evidence from Cl and major element chemistry of MORB, *J. Geophys. Res.*, in press, 1998.
- Michael, P.J. and W.C. Cornell, Spreading rate dependency on magma-hydrothermal systems, *Goldschmidt Conf. Program Abstract*, A70-A71, 1992.
- Michael, P.J. and J.G. Schilling, Chlorine in mid-ocean ridge magmas: Evidence for assimilation of seawater-influenced components, *Geochim. Cosmochim. Acta*, 53, 3131-3143, 1989.

- Michael, P.J. and J.G. Schilling, Chlorine in mid-ocean ridge basalts and FeTi basalts: Evidence for magma chamber contamination by a seawater-derived component?, *EOS Trans. AGU*, 69, 1469, 1988.
- Michard, A., R. Montigny, and R. Schlich, Geochemistry of the mantle beneath the Rodriguez Triple Junction and the Southeast Indian Ridge, *Earth Planet. Sci. Lett.*, 78, 104-114, 1986.
- Moore, J.G., and B.P. Fabbi, An estimate of the juvenile sulfur content of basalt, *Contrib. Mineral. Petrol.*, 33, 118-127, 1971.
- Morgan, W.J., Hotspot tracks and the opening of the Atlantic and Indian Oceans, in *The Sea, The Oceanic Lithosphere*, vol. 7, edited by C. Emiliani, pp. 443-487, Wiley-Interscience, New York, 1981.
- Morgan, W.J., Hotspot tracks and the early rifting of the Atlantic, in *Processes of Continental Rifting*, vol. 94, edited by P. Morgan, pp. 123-139, Tectonophysics, 1983.
- Mutter, J.C., and S.C. Cande, The early opening between Broken Ridge and Kerguelen Plateau, *Earth Planet. Sci. Lett.*, 65, 369-376, 1983.
- Nagshima, S., and T. Katsura, The solubility of sulfur in Na₂O-SiO₂ melts under various oxygen partial pressures at 1100°, 1250° and 1300°C, *Bull. Chemical Soc. Japan*, 46, 3099-3103, 1973.
- Nielsen, R.L., Simulation of igneous differentiation processes, in *Modern Methods of Petrology: Understanding Magmatic Processes, Reviews in Mineralogy*, vol. 24, edited by J. Nicholls and J.K. Russel, pp. 65-106, Mineral. Soc. Amer., 1990.
- Nielsen, R.L., D.M. Christie and F. Sprtel, Anomalously low Na MORB magmas: Evidence for depleted MORB or analytical artifact? *Geochim. Cosmochim. Acta*, 59, 5023-5029, 1995.
- Ohanti, E., I. Kawabe, J. Moriyama, and Y. Nagata, Partitioning of elements between majorite garnet and melt and implications for petrogenesis of komatiite, *Contrib. Mineral. Petrol.*, 103, 263-269, 1989.
- Pyle, D.G., D.M. Christie, and J.J. Mahoney, Resolving an isotope boundary within the AAD, *Earth Planet. Sci. Lett.*, 112, 161-178, 1992.
- Royer, J.Y. and M.F. Coffin, Jurassic to Eocene plate tectonic reconstructions of the southern Kerguelen plateau (Indian Ocean) region, in *Proc. of ODP Sci. Results*, vol. 120, edited by Wise, W.S., R. Schlich et al., pp. 917-928, ODP, College Station, TX, 1992.
- Royer, J.Y. and D.T. Sandwell, Evolution of the eastern Indian Ocean since the late Cretaceous: Constraints from Geosat altimetry, *J. Geophys. Res.*, 94, 13755-13782, 1989.
- Royer, J.Y. and R. Schlich, The SEIR between the Rodriguez Triple Junction and the Amsterdam and St. Paul Islands: Detailed kinematics for the past 20 m.y., *J. Geophys. Res.*, 93, 13524-13550, 1988.

- Sandwell, D.T., and W.H.F. Smith, Global marine gravity from ERS-1, Geosat, and Seasat reveals new tectonic fabric, *EOS Trans. AGU*, 73, 133, 1992.
- Scheirer, D.S., D.W. Forsyth, K.T.M. Johnson, and D.W. Graham, The SEIR near Amsterdam-St. Paul Islands: Results from Boomerang, Leg 6, *Ridge Events*, July 1996.
- Scheirer, D.S., M. Eberle, and D.W. Forsyth, The influence of the Amsterdam-St. Paul hotspot on the morphology of the Southeast Indian Ridge, *EOS Trans. AGU*, 78, F674, 1997.
- Schilling, J.G., Iceland mantle plume, geochemical evidence along Reykjanes Ridge, *Nature*, 242, 565-571, 1973.
- Schilling, J.G., Upper mantle heterogeneities and dynamics, *Nature*, 314, 62-67, 1985.
- Schilling, J.G., Geochemical and isotopic variation along the Mid-Atlantic Ridge axis from 79°N to 0°N, in *The Geology of North America: The Western North Atlantic Region*, vol. M, edited by P.R. Vogt and B.E. Turcholke, pp. 137-156, Geol. Soc. Amer., 1986.
- Schilling, J.G., Fluxes and excess temperatures of mantle plumes inferred from their interaction with migrating mid-ocean ridges, *Nature*, 352, 397-403, 1991.
- Schilling, J.G., M.B. Bergeron, and R. Evans, Halogens in the mantle beneath the North Atlantic, *Phil. Trans. Roy. Soc. Lond.*, A297, 147-178, 1980.
- Schilling, J.G., R.H. Kingsley, and J.D. Devine, Galapagos hot spot-spreading center system 1. Spatial petrological and geochemical variations (83°W-101°W), *J. Geophys. Res.*, 87, 5593-5610, 1982.
- Schilling, J.G., G. Thompson, R.H. Kingsley, and S.E. Humphris, Hotspot-migrating ridge interaction in the South Atlantic: Geochemical evidence, *Nature*, 313, 187-191, 1985.
- Sempéré, J.C., C. Small, A. Shah, B.P. West, D.M. Christie, J.R. Cochran, and L. Geli, Long wavelength variations in segmentation characteristics along the SEIR between 88°E and 120°E, *EOS Trans. AGU*, 76, 146, 1995.
- Sempéré, J.C., J. Palmer, D.M. Christie, J. Phipps-Morgan, and A. Shor, The Australian Antarctic Discordance, *Geology*, 19, 429-432, 1991.
- Sinton, J.M., and R.S. Detrick, Mid-ocean ridge magma chambers, *J. Geophys. Res.*, 97, 197-216, 1992.
- Small, C., and D.T. Sandwell, An abrupt change in ridge axis gravity roughness and spreading rate, *J. Geophys. Res.*, 94, 17383-17392, 1989.
- Storey, M., A.D. Saunders, J. Tarney, I.L. Gibson, M.J. Norry, M.F. Thirwall, P. Leat, R.N. Thompson, and M.A. Menzies, Contamination of Indian Ocean asthenosphere by the Kerguelen-Heard mantle plume, *Nature*, 338, 574-576, 1989.

- Sun, S.S., and W.F. McDonough, Chemical and isotopic systematics of oceanic basalts: Implications for mantle compositions and processes, in *Magmatism in the Ocean Basins*, *Geol. Soc. Spec. Pub.*, no. 42, edited by A.D. Saunders and M.J. Norry, pp. 313-345, Blackwell Scientific Pub., Oxford, 1989.
- Toomey, D.R., S.C. Solomon, and G.M. Purdy, Microearthquakes beneath the median valley of the Mid-Atlantic Ridge near 23°N: Tomography and tectonics, *J. Geophys. Res.*, 93, 9093-9112, 1988.
- Ulmer, P., Partitioning of HFSE among olivine, pyroxenes, garnet and calcalkaline picobasalt: Experimental results and an application, *Annu. Rep. Dir. Geophys. Lab.*, 42-47, 1989.
- Wallace, P., and I.S.E. Carmichael, Sulfur in basaltic magmas, *Geochim. Cosmochim. Acta*, 56, 1863-1874, 1992.
- White, W.M., and A.W. Hoffman, Sr and Nd isotope geochemistry of oceanic basalts and mantle evolution, *Nature*, 296, 821-825, 1982.

Appendices

Appendix 1: Ungrouped Major Element Data.

Three points along a transect were set and analyzed on each glass chip by electron microprobe. Analyses with totals $< 98\%$ or $> 101\%$, those outside a reasonable margin of error as determined by counting statistics, or analyses displaying any obvious anomalies, were excluded from the data set. Those samples left without three useable analyses were reanalyzed. After this screening and any necessary reruns, three or more points from an individual sample were averaged together. The exceptions to this were waxcore 11b and waxcore 32c in which only 2 analyses were averaged together. A total of 312 glass samples were analyzed and these comprise 126 distinct chemical groups. The following table contains the 312 glass samples before group averaging. Operating conditions are listed in the text.

Group	Sample	n=	SiO ₂	TiO ₂	Al ₂ O ₃	FeO*	MnO	MgO	CaO	Na ₂ O	K ₂ O	P ₂ O ₅	Cr ₂ O ₃	Total
1	d33-1	3	50.58	1.56	15.19	9.44	0.11	7.90	12.01	2.66	0.13	0.16	0.04	99.79
1	d33-2	3	50.26	1.53	15.09	9.45	0.14	7.86	11.86	2.65	0.14	0.14	0.04	99.17
1	d33-3	3	50.66	1.57	15.19	9.45	0.16	7.95	12.07	2.65	0.14	0.14	0.05	100.03
2	w3a	3	50.76	1.55	15.11	9.73	0.15	7.06	12.55	2.56	0.15	0.13	0.05	99.78
3	w3b	3	50.23	1.49	14.80	9.67	0.16	7.89	12.34	2.48	0.15	0.12	0.06	99.38
4	d34-1	3	50.93	1.89	13.89	11.00	0.19	6.65	10.92	2.92	0.20	0.17	0.01	98.77
4	d34-2	3	50.95	1.92	13.92	11.13	0.19	6.67	10.78	2.90	0.21	0.19	0.03	98.89
4	d34-3	3	51.38	1.94	13.99	11.10	0.22	6.76	10.88	3.06	0.19	0.19	0.01	99.71
5	d34-4	3	51.29	1.66	14.24	10.31	0.16	7.27	11.36	2.70	0.12	0.16	0.02	99.30
6	d35-1	3	51.27	1.68	14.36	10.11	0.16	7.29	11.57	2.60	0.19	0.16	0.03	99.41
6	d35-2	5	51.58	1.62	14.44	10.18	0.17	7.31	11.95	2.73	0.19	0.15	0.03	100.35
6	d35-3	3	51.14	1.65	14.29	10.04	0.17	7.31	11.72	2.70	0.18	0.15	0.02	99.37
6	d35-4	3	51.00	1.55	14.26	9.87	0.15	7.26	11.50	2.62	0.18	0.16	0.03	98.58
6	d35-8	5	50.92	1.54	14.27	10.06	0.17	7.33	11.58	2.67	0.17	0.15	0.03	98.90
6	d35-9	3	51.06	1.54	14.27	9.98	0.14	7.32	11.54	2.63	0.16	0.14	0.01	98.80
7	d36-1	3	50.63	1.82	14.72	10.25	0.16	7.29	10.84	2.69	0.16	0.20	0.05	98.80
8	d36-2	3	50.54	1.89	14.74	10.60	0.17	7.37	11.34	2.83	0.17	0.17	0.04	99.85
9	d36-4	3	51.19	1.58	14.24	10.14	0.16	7.30	11.49	2.62	0.18	0.15	0.03	99.08
10	d37-1a	3	50.77	2.38	13.76	11.36	0.15	6.59	10.39	2.83	0.18	0.26	0.02	98.69
10	d37-1b	6	50.50	2.38	13.77	11.26	0.18	6.54	10.53	2.84	0.17	0.26	0.03	98.46
10	d37-1c	3	50.68	2.41	13.73	11.40	0.18	6.56	10.56	2.78	0.18	0.27	0.02	98.78
11	d37-2a	3	50.44	2.23	14.25	11.06	0.18	7.13	10.54	2.75	0.18	0.22	0.03	99.00
11	d37-2b	5	50.02	2.23	14.14	11.12	0.19	6.94	10.55	2.64	0.17	0.23	0.04	98.27

Group	Sample	n=	SiO ₂	TiO ₂	Al ₂ O ₃	FeO*	MnO	MgO	CaO	Na ₂ O	K ₂ O	P ₂ O ₅	Cr ₂ O ₃	Total
12	d37-3a	3	50.63	1.69	14.32	10.29	0.14	7.49	11.38	2.47	0.12	0.17	0.04	98.73
12	d37-3b	3	50.47	1.67	14.33	10.35	0.16	7.55	11.40	2.43	0.12	0.16	0.03	98.69
13	w4a	3	51.12	1.48	14.85	9.56	0.15	7.85	11.33	2.50	0.09	0.14	0.05	99.13
13	w4b	3	51.17	1.46	14.91	9.59	0.18	7.74	11.30	2.45	0.09	0.13	0.05	99.08
13	w4c	3	51.01	1.49	14.95	9.51	0.15	7.76	11.37	2.52	0.10	0.15	0.05	99.05
14	w7a	3	50.75	1.33	14.91	9.15	0.11	7.75	11.71	2.52	0.11	0.13	0.06	98.52
14	w7b	3	51.02	1.40	14.91	9.12	0.16	7.87	11.88	2.58	0.11	0.14	0.05	99.23
14	w7c	3	51.36	1.38	15.03	9.17	0.17	7.86	11.81	2.58	0.10	0.09	0.05	99.60
15	d38-brlp a	3	51.00	1.33	15.05	9.10	0.14	7.96	11.84	2.56	0.10	0.14	0.05	99.29
15	d38-brlp b	3	51.05	1.36	14.91	9.14	0.19	7.89	11.71	2.55	0.10	0.11	0.04	99.07
16	d38-brlp c	3	51.10	1.34	15.12	9.21	0.15	7.99	12.22	2.53	0.09	0.11	0.06	99.93
17	w8a	3	50.54	1.56	14.69	10.67	0.17	7.44	11.51	2.71	0.12	0.13	0.04	99.58
17	w8b	3	50.40	1.54	14.67	10.80	0.18	7.33	11.35	2.70	0.12	0.13	0.05	99.26
18	w8c	3	51.04	1.60	14.76	9.97	0.16	7.44	11.81	2.54	0.14	0.14	0.05	99.65
18	w8d	3	51.12	1.60	14.85	9.95	0.13	7.47	11.80	2.53	0.15	0.14	0.04	99.79
19	w9a	3	50.54	1.37	14.72	9.93	0.17	7.87	12.09	2.49	0.08	0.11	0.05	99.44
19	w9b	3	50.49	1.39	14.81	9.89	0.20	7.91	12.04	2.49	0.09	0.11	0.05	99.46
19	w9c	3	51.36	1.39	15.11	9.78	0.18	7.81	12.00	2.41	0.09	0.10	0.04	100.27
20	w10a	3	50.63	1.51	14.69	10.34	0.16	7.45	11.90	2.36	0.14	0.13	0.04	99.36
20	w10b	3	50.34	1.53	14.61	10.27	0.17	7.39	11.88	2.41	0.14	0.14	0.04	98.93
20	w10c	3	50.71	1.53	14.61	10.33	0.20	7.49	11.89	2.43	0.15	0.13	0.06	99.53
21	d39-1	3	50.93	1.21	15.25	8.98	0.15	8.16	12.38	2.26	0.11	0.10	0.05	99.58
21	d39-3	3	51.14	1.21	15.30	9.00	0.16	8.17	12.47	2.23	0.11	0.10	0.05	99.93

Group	Sample	n=	SiO ₂	TiO ₂	Al ₂ O ₃	FeO*	MnO	MgO	CaO	Na ₂ O	K ₂ O	P ₂ O ₅	Cr ₂ O ₃	Total
22	d39-2	3	50.13	1.41	15.10	10.20	0.20	7.77	11.89	2.32	0.08	0.11	0.04	99.25
23	w11a	3	51.04	1.80	14.46	10.90	0.21	7.00	11.44	2.41	0.14	0.17	0.04	99.61
23	w11c	3	50.94	1.79	14.15	10.75	0.19	7.06	11.34	2.52	0.14	0.15	0.04	99.06
24	w11b	2	50.07	1.79	14.22	10.15	0.17	7.33	11.41	2.57	0.15	0.16	0.05	98.07
25	d40-1	3	50.12	1.23	15.20	8.57	0.19	8.23	12.16	2.73	0.08	0.11	0.05	98.67
25	d40-2	3	50.31	1.24	15.23	8.52	0.18	8.22	12.29	2.71	0.09	0.12	0.05	98.97
25	d40-5	4	50.52	1.25	15.28	8.68	0.15	8.27	12.33	2.70	0.08	0.11	0.05	99.41
26	d40-3	3	50.48	1.20	15.33	8.91	0.14	7.93	12.09	2.54	0.08	0.11	0.05	98.87
26	d40-4	3	49.73	1.22	15.45	8.98	0.16	7.90	12.22	2.56	0.08	0.10	0.08	98.47
27	d41-1	3	50.34	1.24	15.11	9.14	0.14	8.03	12.08	2.49	0.09	0.10	0.03	98.80
28	d41-2	3	49.72	1.38	15.23	9.13	0.13	8.11	11.98	2.81	0.07	0.09	0.05	98.68
29	d41-3	3	49.89	1.32	15.43	9.54	0.15	7.86	12.06	2.62	0.07	0.12	0.04	99.10
29	d41-4	3	50.04	1.33	15.48	9.54	0.18	7.79	12.07	2.70	0.06	0.10	0.05	99.35
30	d41-5	3	50.78	1.53	14.81	10.18	0.18	7.45	11.73	2.62	0.10	0.15	0.04	99.58
31	w12a	3	50.82	1.07	15.07	9.43	0.15	8.37	12.40	2.06	0.04	0.09	0.03	99.55
31	w12b	3	50.11	1.05	14.86	9.58	0.16	8.36	12.52	2.12	0.05	0.08	0.05	98.95
32	w12c	3	50.49	1.31	14.49	9.88	0.14	7.48	12.22	2.43	0.09	0.14	0.05	98.72
33	w14a	3	48.43	1.35	16.98	10.01	0.15	8.82	10.39	3.25	0.04	0.09	0.03	99.53
33	w14b	3	48.57	1.34	17.11	9.93	0.18	8.84	10.36	3.17	0.04	0.08	0.04	99.64
33	w14c	3	47.74	1.34	16.80	10.24	0.12	8.65	10.39	3.20	0.04	0.11	0.04	98.68

Group	Sample	n=	SiO ₂	TiO ₂	Al ₂ O ₃	FeO*	MnO	MgO	CaO	Na ₂ O	K ₂ O	P ₂ O ₅	Cr ₂ O ₃	Total
34	d42-1	3	50.88	1.58	14.51	10.34	0.20	7.24	11.83	2.53	0.10	0.14	0.04	99.38
34	d42-2	3	50.58	1.57	14.45	10.35	0.21	7.17	11.83	2.58	0.10	0.12	0.04	99.02
35	w15a	3	50.92	1.50	14.32	10.55	0.16	7.52	11.79	2.38	0.07	0.12	0.04	99.37
35	w15b	3	50.88	1.51	14.52	10.26	0.20	7.61	11.90	2.46	0.07	0.11	0.04	99.57
35	w15c	3	50.92	1.53	14.32	10.25	0.19	7.65	11.88	2.42	0.06	0.12	0.02	99.36
36	d43-1	3	50.47	1.39	15.57	9.13	0.17	8.34	11.92	2.58	0.06	0.11	0.05	99.79
36	d43-2	3	50.45	1.37	15.54	9.22	0.15	8.35	12.02	2.56	0.06	0.14	0.05	99.90
36	d43-3	3	50.81	1.36	15.58	9.08	0.14	8.37	12.03	2.64	0.05	0.10	0.05	100.21
37	d43-4	3	50.85	1.27	15.35	9.34	0.17	8.47	12.07	2.44	0.06	0.11	0.04	100.18
38	d43-6	3	50.86	1.52	15.00	9.83	0.19	8.04	11.87	2.46	0.06	0.13	0.03	99.98
39	w16a	3	51.47	1.60	14.57	9.99	0.17	7.72	11.94	2.51	0.07	0.13	0.04	100.22
39	w16b	3	51.23	1.59	14.60	10.04	0.20	7.66	11.83	2.51	0.07	0.16	0.04	99.93
40	d44-1	3	50.82	1.41	14.50	10.11	0.18	7.69	12.22	2.55	0.10	0.12	0.05	99.77
40	d44-2	3	50.70	1.43	14.37	10.27	0.18	7.61	12.14	2.60	0.10	0.11	0.05	99.57
40	d44-3	3	50.61	1.43	14.46	10.08	0.19	7.72	12.26	2.54	0.10	0.12	0.05	99.55
40	d44-4	3	50.83	1.43	14.38	10.41	0.16	7.61	12.06	2.52	0.10	0.14	0.05	99.67
40	d44-5	3	50.73	1.42	14.52	10.02	0.17	7.66	12.20	2.52	0.10	0.11	0.04	99.50
40	d44-6	3	50.60	1.42	14.36	10.26	0.20	7.60	12.12	2.53	0.10	0.14	0.05	99.38
41	w17a	3	51.40	1.58	14.30	10.39	0.18	7.62	11.79	2.36	0.06	0.13	0.04	99.85
41	w17b	3	51.38	1.59	14.28	10.36	0.16	7.60	11.76	2.37	0.07	0.12	0.02	99.72
41	w17c	3	50.94	1.55	14.24	10.46	0.17	7.61	11.73	2.36	0.08	0.13	0.03	99.30
42	w18a	3	50.96	1.37	14.51	9.69	0.15	7.98	12.34	2.32	0.05	0.10	0.04	99.51
42	w18b	3	51.17	1.38	14.48	9.70	0.15	7.97	12.33	2.33	0.06	0.10	0.06	99.72
42	w18c	3	51.07	1.35	14.42	9.81	0.19	7.88	12.38	2.30	0.06	0.10	0.06	99.63

Group	Sample	n=	SiO ₂	TiO ₂	Al ₂ O ₃	FeO*	MnO	MgO	CaO	Na ₂ O	K ₂ O	P ₂ O ₅	Cr ₂ O ₃	Total
43	w19a	3	51.14	1.34	14.50	9.67	0.18	7.96	12.31	2.31	0.06	0.12	0.05	99.66
44	w19b	3	50.08	1.19	14.99	9.71	0.15	8.16	12.11	2.17	0.09	0.10	0.04	98.80
44	w19c	3	50.76	1.19	15.18	9.53	0.16	8.16	12.14	2.21	0.08	0.09	0.04	99.53
45	d46-1	3	51.75	1.06	14.68	9.08	0.15	8.19	12.60	2.11	0.06	0.08	0.05	99.81
45	d46-2	3	51.72	1.06	14.70	9.14	0.17	8.17	12.64	2.14	0.07	0.08	0.05	99.92
46	w20a	3	50.68	1.10	15.44	9.63	0.14	8.24	12.03	2.25	0.07	0.07	0.05	99.69
46	w20b	3	50.31	1.13	15.37	9.60	0.15	8.18	11.99	2.23	0.07	0.08	0.06	99.18
46	w20c	3	50.38	1.15	15.36	9.69	0.15	8.14	12.07	2.23	0.08	0.10	0.05	99.39
47	d47-1	3	50.43	1.11	15.50	9.11	0.17	8.34	12.40	2.33	0.13	0.10	0.05	99.67
47	d47-2	3	50.20	1.10	15.46	9.23	0.13	8.42	12.42	2.40	0.13	0.08	0.03	99.60
47	d47-3	3	50.30	1.12	15.45	9.15	0.15	8.40	12.36	2.37	0.13	0.11	0.06	99.60
47	d47-4	3	50.20	1.14	15.48	9.20	0.16	8.45	12.50	2.29	0.12	0.10	0.06	99.70
47	d47-5	3	50.28	1.13	15.41	9.19	0.13	8.41	12.47	2.34	0.12	0.11	0.06	99.66
47	d47-6	3	50.31	1.13	15.55	9.09	0.14	8.43	12.48	2.37	0.12	0.11	0.06	99.81
48	d48-1	3	49.84	1.26	15.80	9.95	0.17	8.35	11.56	2.38	0.15	0.11	0.04	99.61
48	d48-2	3	49.77	1.25	15.86	9.90	0.15	8.32	11.54	2.36	0.15	0.09	0.04	99.45
48	d48-3	3	49.77	1.25	15.85	9.80	0.16	8.29	11.50	2.38	0.14	0.12	0.03	99.29
48	d48-4	3	49.91	1.27	15.95	9.82	0.16	8.26	11.55	2.40	0.15	0.12	0.04	99.63
49	d49-1	3	51.39	1.79	14.06	11.12	0.17	6.31	10.59	2.75	0.30	0.19	0.02	98.69
50	d49-3	5	51.89	2.97	12.22	16.22	0.25	3.89	8.17	3.11	0.54	0.34	0.01	99.61
51	w21a	3	51.01	1.69	14.19	10.99	0.25	6.78	11.10	2.57	0.25	0.17	0.05	99.04
51	w21b	3	51.02	1.67	14.18	10.98	0.19	6.77	11.21	2.59	0.27	0.18	0.03	99.07
51	w21c	3	50.90	1.70	14.23	10.86	0.21	6.73	11.12	2.57	0.25	0.19	0.03	98.78

Group	Sample	n=	SiO ₂	TiO ₂	Al ₂ O ₃	FeO*	MnO	MgO	CaO	Na ₂ O	K ₂ O	P ₂ O ₅	Cr ₂ O ₃	Total
52	d50-brlp a	3	50.89	1.54	14.84	10.04	0.16	7.55	11.27	2.48	0.26	0.17	0.03	99.24
52	d50-brlp c	3	51.31	1.55	14.95	10.52	0.16	7.49	11.44	2.52	0.28	0.16	0.04	100.44
53	d50-brlp b	3	51.46	1.65	14.79	10.74	0.19	7.13	11.33	2.63	0.30	0.16	0.03	100.43
54	w23a	6	50.90	1.24	14.74	9.59	0.16	7.75	12.24	2.37	0.16	0.13	0.06	99.33
54	w23b	6	50.96	1.22	14.80	9.56	0.17	7.78	12.26	2.37	0.16	0.11	0.06	99.46
54	w23c	3	51.10	1.22	14.84	9.58	0.18	7.77	12.25	2.45	0.16	0.15	0.06	99.77
55	d51-1	3	51.37	1.80	14.02	11.22	0.22	6.36	10.82	2.69	0.31	0.20	0.02	99.03
55	d51-brlp a	3	51.33	1.74	14.13	11.17	0.19	6.50	10.91	2.63	0.30	0.18	0.03	99.12
55	d51-brlp b	3	51.40	1.77	14.08	10.99	0.16	6.52	10.89	2.65	0.29	0.17	0.01	98.93
55	d51-brlp c	3	51.29	1.77	14.17	10.94	0.21	6.53	10.86	2.63	0.30	0.19	0.02	98.89
56	d52-brlp a	3	50.44	0.97	15.32	8.87	0.14	8.86	12.85	2.09	0.14	0.10	0.05	99.83
57	d52-brlp b	3	50.29	1.11	15.52	9.60	0.17	8.56	12.20	2.18	0.17	0.11	0.02	99.94
58	d52-brlp c	3	50.39	1.17	15.08	9.64	0.17	8.27	12.04	2.39	0.15	0.12	0.03	99.46
59	w25a	3	50.84	2.06	14.62	10.87	0.18	6.11	10.38	2.86	0.50	0.23	0.03	98.68
59	w25b	3	50.91	2.07	14.76	11.04	0.16	6.12	10.32	2.92	0.51	0.23	0.03	99.05
59	w25c	3	50.66	2.06	14.58	10.83	0.19	6.13	10.33	2.90	0.49	0.23	0.04	98.43
60	d53-1	5	51.42	1.81	14.26	11.25	0.19	6.65	11.18	2.73	0.33	0.18	0.03	100.04
61	d54-1	3	51.19	1.98	13.72	12.47	0.21	5.99	10.32	2.81	0.29	0.19	0.01	99.17
61	d54-4	3	51.00	1.95	13.63	12.30	0.18	5.99	10.22	2.84	0.30	0.16	0.01	98.59
62	d54-2	3	51.24	1.79	14.34	10.81	0.19	6.44	10.79	2.74	0.33	0.21	0.00	98.89
62	d54-3	3	51.30	1.80	14.50	10.83	0.20	6.41	10.82	2.72	0.35	0.18	0.02	99.15
62	d54-5	3	51.36	1.78	14.38	10.91	0.15	6.36	10.70	2.72	0.34	0.19	0.00	98.87
62	d54-6	3	51.28	1.77	14.46	10.85	0.16	6.55	10.86	2.72	0.34	0.17	0.02	99.19

Group	Sample	n=	SiO ₂	TiO ₂	Al ₂ O ₃	FeO*	MnO	MgO	CaO	Na ₂ O	K ₂ O	P ₂ O ₅	Cr ₂ O ₃	Total
63	w29a	3	51.07	2.18	13.66	12.39	0.22	5.72	10.20	2.76	0.38	0.25	0.03	98.85
64	w29b	3	51.23	2.28	13.46	12.69	0.22	5.51	9.85	2.79	0.39	0.25	0.02	98.67
64	w29c	2	51.25	2.29	13.43	12.84	0.18	5.53	9.82	2.82	0.40	0.23	0.01	98.79
65	w26a	3	51.61	1.70	14.54	10.37	0.19	6.86	10.81	2.69	0.29	0.17	0.04	99.27
65	w26b	3	51.58	1.69	14.56	10.45	0.20	6.86	10.89	2.68	0.30	0.17	0.05	99.43
65	w26c	3	51.46	1.71	14.46	10.41	0.18	6.79	10.87	2.75	0.30	0.18	0.03	99.14
66	d55-1	3	51.27	1.38	14.74	9.69	0.17	7.46	11.75	2.49	0.28	0.13	0.04	99.40
67	d55-2	3	51.31	1.80	14.18	10.90	0.18	6.52	10.78	2.69	0.35	0.20	0.02	98.93
68	w30a	3	51.25	1.78	14.55	10.41	0.19	6.84	11.25	2.70	0.38	0.20	0.02	99.58
68	w30b	3	51.00	1.75	14.37	10.25	0.16	6.72	11.11	2.58	0.37	0.18	0.03	98.52
68	w30c	3	51.15	1.78	14.48	10.45	0.16	6.78	11.19	2.66	0.37	0.22	0.02	99.27
69	d59-1	3	50.99	1.70	14.88	10.00	0.20	7.13	11.51	2.59	0.41	0.18	0.04	99.64
69	d59-2	3	51.04	1.69	14.75	10.04	0.14	7.12	11.55	2.58	0.41	0.21	0.04	99.57
69	d59-3	3	51.01	1.68	14.86	9.74	0.17	7.12	11.47	2.55	0.42	0.20	0.05	99.24
69	d59-4	3	51.25	1.71	14.78	9.97	0.18	7.17	11.69	2.46	0.39	0.20	0.02	99.82
69	d59-5	3	51.34	1.72	14.87	9.97	0.14	7.08	11.50	2.52	0.41	0.19	0.03	99.78
69	d59-6	3	51.15	1.71	14.79	10.04	0.18	7.06	11.50	2.56	0.42	0.21	0.03	99.65
69	d59-7	3	51.30	1.74	14.80	10.04	0.18	7.09	11.48	2.56	0.42	0.20	0.04	99.85
70	w31a	3	51.14	1.91	14.77	10.68	0.19	6.59	10.75	2.77	0.43	0.20	0.03	99.45
70	w31b	3	50.79	1.89	14.69	10.70	0.20	6.63	10.85	2.76	0.42	0.23	0.02	99.18
70	w31c	3	50.78	1.93	14.60	10.75	0.17	6.56	10.83	2.74	0.43	0.24	0.02	99.06
71	d60-1	3	51.14	1.36	15.03	10.06	0.16	7.50	11.84	2.42	0.26	0.13	0.03	99.94
72	d60-2	3	51.19	1.35	15.30	9.90	0.18	6.86	11.76	2.48	0.27	0.14	0.03	99.48

Group	Sample	n=	SiO ₂	TiO ₂	Al ₂ O ₃	FeO*	MnO	MgO	CaO	Na ₂ O	K ₂ O	P ₂ O ₅	Cr ₂ O ₃	Total
73	d60-3	3	51.25	1.54	14.57	10.87	0.18	6.58	11.37	2.52	0.30	0.14	0.01	99.34
73	d60-4	3	51.12	1.54	14.37	10.69	0.21	6.87	11.57	2.52	0.29	0.14	0.02	99.33
74	d61-1	3	51.30	1.69	14.93	10.39	0.16	7.12	11.26	2.58	0.34	0.18	0.02	99.96
74	d61-2	3	51.53	1.67	14.94	10.22	0.17	7.10	11.22	2.60	0.33	0.20	0.05	100.04
74	d61-3	3	51.34	1.66	14.94	10.21	0.17	7.16	11.22	2.53	0.32	0.18	0.04	99.78
74	d61-4	3	51.36	1.68	14.90	10.23	0.15	7.13	11.16	2.56	0.33	0.18	0.04	99.73
75	w32a	3	50.89	1.47	15.09	10.06	0.20	8.04	10.91	2.49	0.27	0.17	0.04	99.63
76	w32b	3	51.19	1.50	15.23	10.24	0.18	7.71	11.05	2.59	0.28	0.17	0.04	100.17
76	w32d	3	51.55	1.51	15.25	10.40	0.18	7.63	11.10	2.62	0.28	0.15	0.03	100.70
76	w32e	3	51.11	1.51	15.10	10.44	0.15	7.73	11.09	2.58	0.27	0.17	0.05	100.20
77	w32c	2	51.04	1.52	15.31	10.21	0.15	7.38	11.21	2.60	0.27	0.16	0.04	99.89
78	w33a	3	50.63	1.74	15.02	11.28	0.19	6.97	10.68	2.66	0.29	0.17	0.02	99.65
78	w33b	3	50.57	1.78	15.04	11.46	0.20	7.03	10.72	2.71	0.30	0.16	0.03	99.99
78	w33c	3	50.54	1.76	14.92	11.19	0.18	6.86	10.67	2.66	0.30	0.17	0.02	99.27
79	w35a	3	51.40	1.65	14.28	10.83	0.17	6.64	11.11	2.51	0.39	0.22	0.01	99.21
79	w35b	3	51.26	1.61	14.32	10.69	0.16	6.81	11.23	2.44	0.38	0.20	0.01	99.12
79	w35c	3	51.38	1.61	14.31	10.55	0.17	6.84	11.23	2.45	0.37	0.19	0.03	99.13
80	d62-brlp a	3	51.80	2.04	14.04	11.45	0.20	5.73	10.19	2.61	0.60	0.27	0.00	98.94
80	d62-brlp b	3	51.58	1.94	14.15	11.21	0.17	6.01	10.37	2.59	0.56	0.25	0.02	98.84
81	w36a	3	51.07	2.04	14.23	10.97	0.19	6.05	10.48	2.69	0.58	0.28	0.01	98.58
81	w36b	3	51.45	2.03	14.30	11.17	0.21	6.13	10.59	2.69	0.58	0.26	0.03	99.45
81	w36c	3	51.44	2.04	14.29	10.80	0.14	6.02	10.48	2.64	0.60	0.25	0.03	98.74

Group	Sample	n=	SiO ₂	TiO ₂	Al ₂ O ₃	FeO*	MnO	MgO	CaO	Na ₂ O	K ₂ O	P ₂ O ₅	Cr ₂ O ₃	Total
82	d63-1	3	51.21	1.66	14.60	10.28	0.16	7.00	11.50	2.40	0.42	0.19	0.02	99.45
82	d63-2	3	51.08	1.65	14.60	10.34	0.16	6.95	11.44	2.39	0.43	0.23	0.01	99.26
82	d63-3	3	51.11	1.64	14.56	10.40	0.16	7.03	11.48	2.38	0.43	0.20	0.00	99.41
82	d63-4	3	51.16	1.64	14.65	10.24	0.17	7.03	11.48	2.36	0.42	0.20	0.02	99.36
82	d63-5	3	51.21	1.65	14.64	10.18	0.17	6.92	11.53	2.37	0.42	0.18	0.04	99.31
83	w37a	3	51.90	1.86	14.61	10.80	0.14	6.16	10.58	2.70	0.55	0.22	0.03	99.54
83	w37b	3	51.91	1.84	14.45	10.49	0.20	6.15	10.72	2.60	0.56	0.20	0.03	99.14
83	w37c	3	51.84	1.81	14.49	10.61	0.18	6.12	10.55	2.63	0.55	0.23	0.03	99.05
84	d64-1	3	51.74	1.86	14.72	10.23	0.16	6.06	10.58	2.65	0.66	0.26	0.01	98.93
84	d64-3	3	51.96	1.91	14.87	10.38	0.15	5.90	10.56	2.68	0.67	0.26	0.00	99.35
84	d64-6	3	51.88	1.82	14.75	10.25	0.19	6.15	10.64	2.57	0.65	0.23	0.01	99.14
84	d64-7	3	51.75	1.80	14.75	10.28	0.18	6.18	10.69	2.69	0.64	0.26	0.00	99.23
84	d64-8	3	51.70	1.86	14.63	10.55	0.17	6.05	10.58	2.70	0.65	0.23	0.02	99.13
84	d64-9	3	51.71	1.81	14.69	10.18	0.17	6.10	10.66	2.68	0.64	0.25	0.01	98.90
84	d64-10	3	51.71	1.83	14.78	10.21	0.17	6.14	10.59	2.65	0.64	0.24	0.01	98.97
85	d64-2	3	53.47	1.84	14.53	10.51	0.17	5.11	9.28	2.94	0.81	0.30	0.02	98.97
85	d64-4	3	53.37	1.89	14.59	10.50	0.18	5.08	9.29	2.97	0.83	0.29	0.01	99.01
85	d64-5	3	53.71	1.90	14.50	10.63	0.16	4.91	9.05	2.95	0.84	0.31	0.01	98.98
85	d64-11	3	53.16	1.87	14.56	10.53	0.16	5.16	9.38	2.92	0.78	0.30	0.01	98.83
86	w38a	3	50.35	1.51	14.80	10.01	0.18	7.53	12.01	2.36	0.28	0.17	0.04	99.25
86	w38b	3	50.37	1.49	14.77	9.91	0.16	7.52	11.97	2.34	0.28	0.16	0.04	99.01
86	w38c	3	50.47	1.52	14.82	9.84	0.18	7.62	12.09	2.35	0.30	0.16	0.04	99.37
87	d65-brlp a	3	52.23	2.10	14.16	11.18	0.17	5.10	9.33	2.89	0.78	0.29	0.01	98.24
87	d65-brlp b	2	52.03	2.22	14.08	11.20	0.19	5.09	9.51	2.90	0.75	0.27	0.00	98.24
87	d65-brlp c	3	52.21	2.17	14.24	11.03	0.19	5.13	9.43	2.86	0.75	0.28	0.02	98.32

Group	Sample	n=	SiO ₂	TiO ₂	Al ₂ O ₃	FeO*	MnO	MgO	CaO	Na ₂ O	K ₂ O	P ₂ O ₅	Cr ₂ O ₃	Total
88	w39a	3	50.68	2.49	13.60	12.93	0.21	5.00	9.51	3.06	0.68	0.29	0.00	98.46
88	w39b	3	50.59	2.53	13.54	13.08	0.21	4.90	9.44	2.99	0.67	0.30	0.01	98.27
88	w39c	3	50.50	2.53	13.54	13.23	0.19	4.90	9.42	3.07	0.67	0.30	0.00	98.34
89	d66-1	3	50.09	1.77	15.02	10.11	0.17	7.25	11.63	2.46	0.41	0.22	0.04	99.17
89	d66-2	3	50.36	1.70	15.19	10.04	0.16	7.26	11.64	2.44	0.40	0.18	0.03	99.40
89	d66-3	3	50.15	1.74	15.06	9.95	0.15	7.16	11.60	2.46	0.41	0.20	0.03	98.92
89	d66-4	3	50.09	1.73	15.28	10.07	0.19	7.25	11.60	2.40	0.40	0.21	0.03	99.26
90	d67-1	3	51.39	2.17	14.54	11.07	0.19	5.96	10.37	2.77	0.52	0.26	0.02	99.27
90	d67-2	3	51.26	2.15	14.55	11.14	0.19	5.88	10.27	2.75	0.52	0.24	0.02	98.97
90	d67-3	3	51.48	2.14	14.35	11.04	0.20	5.96	10.48	2.67	0.53	0.28	0.02	99.15
91	d68-1	3	50.92	2.40	14.00	12.50	0.21	5.27	9.80	3.01	0.58	0.26	0.01	98.95
91	d68-2	3	50.92	2.40	14.13	12.52	0.22	5.31	9.84	2.96	0.59	0.27	0.01	99.17
91	d68-brlp a	3	50.96	2.41	13.93	12.46	0.20	5.20	9.87	3.00	0.60	0.25	0.00	98.90
91	d68-brlp b	3	51.00	2.38	14.08	12.65	0.20	5.23	9.73	3.06	0.58	0.26	0.01	99.19
92	w42a	3	51.30	2.63	13.71	12.93	0.24	4.88	9.31	3.09	0.61	0.30	0.00	98.99
92	w42b	3	51.00	2.59	13.68	12.90	0.20	4.85	9.24	2.92	0.60	0.27	0.00	98.26
92	w42c	2	51.15	2.58	13.70	12.91	0.17	4.79	9.25	2.98	0.58	0.30	0.01	98.42
93	d70-1	3	50.78	1.27	15.03	9.30	0.15	8.03	12.47	2.18	0.24	0.14	0.04	99.62
93	d70-2	3	51.05	1.26	15.25	9.17	0.17	7.90	12.57	2.11	0.24	0.13	0.05	99.90
93	d70-3	3	50.96	1.29	15.21	9.12	0.15	7.93	12.45	2.15	0.24	0.13	0.03	99.66
93	d70-4	3	51.08	1.29	15.04	9.16	0.18	7.87	12.56	2.17	0.25	0.12	0.06	99.77
93	d70-5	3	50.75	1.27	15.21	9.17	0.15	8.00	12.52	2.23	0.24	0.14	0.02	99.70
93	d70-brlp a	3	51.00	1.29	15.09	9.16	0.17	7.79	12.51	2.19	0.24	0.11	0.04	99.59
94	w43a	3	51.25	1.38	14.90	9.65	0.17	7.68	11.87	2.37	0.24	0.15	0.02	99.68

Group	Sample	n=	SiO ₂	TiO ₂	Al ₂ O ₃	FeO*	MnO	MgO	CaO	Na ₂ O	K ₂ O	P ₂ O ₅	Cr ₂ O ₃	Total
95	w43b	3	51.31	1.40	14.96	9.69	0.20	7.29	11.91	2.39	0.25	0.14	0.04	99.58
95	w43c	3	51.41	1.40	14.99	9.68	0.13	7.34	11.90	2.39	0.25	0.14	0.02	99.64
96	d71-1	3	51.32	1.87	13.84	11.62	0.19	6.06	10.73	2.61	0.29	0.18	0.01	98.72
96	d71-2	3	51.34	1.83	13.90	11.64	0.20	6.06	10.74	2.71	0.30	0.16	0.02	98.89
97	d71-3	3	51.37	1.73	14.06	11.30	0.20	6.43	11.01	2.56	0.29	0.18	0.03	99.18
97	d71-4	3	50.97	1.71	14.01	11.28	0.21	6.42	11.03	2.58	0.28	0.18	0.02	98.70
97	d71-5	3	51.47	1.74	14.21	11.38	0.18	6.49	11.03	2.60	0.28	0.17	0.02	99.56
98	d72-brlp a	3	51.63	1.03	14.58	9.58	0.15	7.99	12.75	2.04	0.06	0.08	0.05	99.94
98	d72-brlp b	3	51.60	1.03	14.63	9.64	0.19	8.12	12.79	2.12	0.06	0.08	0.02	100.29
98	d72-brlp c	3	51.48	1.02	14.48	9.67	0.17	7.98	12.68	2.05	0.06	0.08	0.05	99.71
99	w46a	3	50.36	1.06	16.14	8.38	0.17	8.07	12.30	2.42	0.41	0.16	0.05	99.50
99	w46b	3	50.49	1.06	16.16	8.43	0.16	8.10	12.33	2.36	0.39	0.16	0.05	99.70
99	w46c	3	50.50	1.09	16.23	8.44	0.16	8.14	12.36	2.35	0.41	0.15	0.04	99.88
100	d73-1	3	49.93	1.31	16.03	9.51	0.19	7.85	11.62	2.49	0.44	0.21	0.03	99.62
100	d73-2	3	49.89	1.31	15.87	9.45	0.18	7.80	11.69	2.45	0.43	0.16	0.05	99.27
100	d73-3	3	49.96	1.33	15.88	9.42	0.18	7.84	11.59	2.49	0.43	0.17	0.05	99.33
101	d73-4	3	50.85	0.76	15.82	8.57	0.16	9.28	13.40	1.80	0.03	0.05	0.07	100.77
101	d73-5	3	50.73	0.76	15.59	8.49	0.16	9.21	13.42	1.70	0.03	0.05	0.07	100.21
102	d73-6	3	50.73	1.02	15.79	8.10	0.17	8.57	12.73	2.15	0.27	0.12	0.05	99.70
103	w47a	3	49.72	1.30	16.41	8.50	0.14	7.82	11.89	2.68	0.68	0.20	0.05	99.39
103	w47b	3	49.87	1.28	16.44	8.49	0.14	7.86	11.87	2.67	0.68	0.17	0.05	99.51
103	w47e	3	49.23	1.30	16.20	8.70	0.12	7.78	12.04	2.71	0.72	0.19	0.04	99.03
103	w47f	3	49.53	1.30	16.26	8.60	0.16	7.94	11.99	2.74	0.71	0.19	0.04	99.47
103	w47g	3	49.31	1.28	16.21	8.67	0.15	7.78	11.95	2.72	0.70	0.21	0.04	99.03

Group	Sample	n=	SiO ₂	TiO ₂	Al ₂ O ₃	FeO*	MnO	MgO	CaO	Na ₂ O	K ₂ O	P ₂ O ₅	Cr ₂ O ₃	Total
104	w47c	3	51.06	1.14	14.81	9.53	0.13	8.53	11.71	2.13	0.22	0.13	0.03	99.41
104	w47d	3	50.11	1.17	14.71	9.72	0.14	8.38	11.90	2.16	0.24	0.08	0.06	98.66
105	d74-brlp a	3	49.83	1.00	16.21	9.50	0.17	8.79	12.36	2.19	0.09	0.07	0.05	100.26
105	d74-brlp c	3	50.01	0.96	16.31	9.40	0.15	8.92	12.33	2.13	0.08	0.06	0.05	100.39
106	d74-brlp b	3	50.57	1.22	16.18	8.57	0.16	8.00	11.80	2.39	0.47	0.15	0.04	99.57
107	w48a	3	50.94	0.99	15.22	9.15	0.19	8.31	12.92	2.06	0.14	0.10	0.06	100.09
107	w48b	3	51.11	0.97	15.54	9.27	0.18	8.51	12.82	2.09	0.13	0.08	0.06	100.76
107	w48c	3	51.27	0.99	15.42	9.31	0.17	8.34	12.81	2.08	0.14	0.10	0.07	100.69
108	w49a	3	51.63	1.17	14.81	9.60	0.14	8.02	12.34	2.16	0.21	0.13	0.03	100.26
108	w49b	3	51.47	1.16	14.79	9.58	0.16	7.91	12.36	2.13	0.21	0.12	0.04	99.92
109	w50a	3	49.90	1.04	15.50	10.51	0.15	8.54	11.95	1.94	0.10	0.09	0.05	99.78
109	w50b	3	49.19	1.01	15.11	10.73	0.15	8.92	11.83	1.91	0.10	0.09	0.04	99.09
109	w50c	3	49.83	1.07	15.53	10.67	0.19	8.69	11.85	1.98	0.10	0.10	0.05	100.05
110	d78-brlp a	3	51.30	1.32	15.51	9.04	0.17	8.55	11.78	2.43	0.07	0.11	0.04	100.31
110	d78-brlp b	3	51.07	1.31	15.34	9.16	0.15	8.60	11.89	2.46	0.09	0.10	0.04	100.22
110	d78-brlp c	3	50.93	1.34	15.09	9.07	0.17	8.51	11.86	2.49	0.07	0.12	0.04	99.69
111	w52a	3	50.73	1.17	15.42	8.61	0.13	8.22	12.39	2.45	0.16	0.12	0.04	99.43
111	w52b	3	51.22	1.17	15.46	8.63	0.16	8.26	12.41	2.45	0.15	0.13	0.05	100.11
111	w52c	3	50.99	1.16	15.37	8.77	0.16	8.22	12.35	2.43	0.15	0.10	0.05	99.75
112	d79-1a	3	50.56	1.05	14.84	8.95	0.16	8.30	12.90	2.28	0.10	0.09	0.06	99.30
112	d79-1b	3	51.17	1.08	15.13	8.88	0.15	8.37	12.71	2.24	0.11	0.11	0.05	100.00

Group	Sample	n=	SiO ₂	TiO ₂	Al ₂ O ₃	FeO*	MnO	MgO	CaO	Na ₂ O	K ₂ O	P ₂ O ₅	Cr ₂ O ₃	Total
113	w53a	3	51.09	1.38	14.79	9.49	0.18	7.69	12.21	2.61	0.12	0.13	0.05	99.74
113	w53b	3	50.99	1.39	14.74	9.49	0.16	7.71	12.29	2.62	0.12	0.12	0.04	99.68
113	w53c	3	50.79	1.33	14.88	9.27	0.16	7.79	12.32	2.65	0.10	0.10	0.04	99.43
114	d76-1	3	48.80	1.24	16.86	9.23	0.14	8.14	11.65	2.99	0.18	0.13	0.03	99.39
114	d76-2	3	48.84	1.24	17.10	9.18	0.17	8.31	11.59	3.02	0.18	0.13	0.03	99.78
114	d76-3	3	49.12	1.23	17.14	9.30	0.16	8.23	11.56	2.94	0.18	0.12	0.04	100.01
114	d76-4	3	49.14	1.23	17.16	9.33	0.16	8.26	11.55	2.98	0.19	0.14	0.03	100.19
114	d76-5	3	49.23	1.23	17.22	9.26	0.12	8.30	11.56	3.02	0.18	0.11	0.04	100.28
115	d76-6	3	48.95	1.31	16.63	9.76	0.17	7.95	11.61	3.11	0.20	0.14	0.04	99.87
116	d77-1	3	50.26	1.56	15.37	9.70	0.15	7.89	11.71	2.71	0.14	0.15	0.03	99.65
116	d77-2	3	50.36	1.53	15.40	9.61	0.18	7.93	11.65	2.74	0.14	0.16	0.03	99.73
116	d77-3	3	50.64	1.51	15.54	9.70	0.18	8.09	11.68	2.71	0.13	0.15	0.04	100.37
116	d77-4	3	50.40	1.55	15.41	9.64	0.16	7.89	11.72	2.64	0.14	0.13	0.04	99.72
117	w51a	3	49.11	1.36	16.14	9.92	0.16	8.19	11.45	2.66	0.13	0.15	0.04	99.30
117	w51b	3	49.47	1.34	16.29	9.95	0.14	8.25	11.30	2.67	0.14	0.15	0.04	99.74
117	w51c	3	49.47	1.34	16.36	9.79	0.17	8.35	11.34	2.72	0.14	0.12	0.04	99.83
118	SP-1a	3	50.63	3.29	13.37	14.18	0.24	4.49	8.91	3.25	0.99	0.41	0.00	99.76
118	SP-5b	3	50.29	3.23	13.33	13.92	0.22	4.45	8.78	3.14	0.97	0.45	0.00	98.77
119	d58-1	3	48.19	1.12	17.15	10.90	0.16	8.89	10.93	2.50	0.06	0.07	0.03	100.00
119	d58-2	3	48.02	1.13	17.30	11.08	0.19	8.90	11.04	2.61	0.06	0.06	0.04	100.42
119	d58-3	5	48.41	1.14	17.31	11.08	0.14	8.87	11.00	2.67	0.06	0.07	0.04	100.80
120	d58-4	3	48.49	1.27	16.59	11.31	0.17	8.35	11.23	2.64	0.06	0.06	0.04	100.21

Group	Sample	n=	SiO ₂	TiO ₂	Al ₂ O ₃	FeO*	MnO	MgO	CaO	Na ₂ O	K ₂ O	P ₂ O ₅	Cr ₂ O ₃	Total
121	w34a	3	51.06	1.88	15.55	10.22	0.15	6.77	9.83	2.96	0.38	0.19	0.03	99.02
121	w34b	3	51.02	1.88	15.61	10.19	0.15	6.68	9.81	2.92	0.37	0.22	0.05	98.90
121	w34c	3	51.34	1.86	15.60	10.26	0.16	6.73	9.88	2.92	0.39	0.22	0.02	99.37
122	d75-1	3	49.80	1.20	15.00	9.44	0.17	8.35	12.72	2.34	0.08	0.11	0.04	99.24
122	d75-2	3	49.90	1.20	15.12	9.37	0.18	8.53	12.69	2.29	0.07	0.11	0.05	99.51
122	d75-4	3	50.16	1.19	15.27	9.35	0.14	8.52	12.67	2.34	0.06	0.14	0.05	99.89
122	d75-5	3	49.97	1.16	15.02	9.61	0.15	8.38	12.59	2.29	0.07	0.13	0.05	99.40
122	d75-6	3	50.37	1.23	15.03	9.68	0.16	8.30	12.80	2.31	0.07	0.12	0.06	100.12
123	d75-3	3	50.87	1.35	14.42	10.05	0.17	7.97	12.49	2.43	0.04	0.10	0.03	99.91
124	w44a	3	50.73	2.63	13.54	13.11	0.22	4.66	9.29	3.09	0.75	0.31	0.00	98.33
124	w44b	3	50.98	2.69	13.50	13.30	0.20	4.59	9.22	3.00	0.78	0.31	0.01	98.58
124	w44c	3	51.07	2.60	13.60	13.07	0.24	4.71	9.36	3.06	0.76	0.30	0.01	98.78
125	w45a	3	50.76	2.12	14.26	11.67	0.21	5.88	10.52	2.80	0.61	0.25	0.01	99.10
125	w45b	3	50.80	2.11	14.09	11.60	0.21	5.81	10.50	2.82	0.62	0.22	0.00	98.79
125	w45d	3	50.98	2.14	14.25	11.98	0.18	5.96	10.66	2.93	0.62	0.28	0.01	100.00
125	w45f	3	50.35	2.13	14.07	11.95	0.19	5.80	10.56	2.83	0.62	0.23	0.01	98.76
125	w45h	3	50.39	2.16	13.99	11.84	0.20	5.78	10.56	2.90	0.63	0.26	0.01	98.71
126	w45c	3	50.99	2.53	13.78	13.09	0.22	4.79	9.28	3.02	0.74	0.30	0.02	98.75
126	w45e	3	50.86	2.55	13.66	13.36	0.18	4.78	9.43	3.19	0.76	0.30	0.01	99.09
126	w45g	3	50.55	2.54	13.67	13.23	0.22	4.80	9.28	3.19	0.75	0.30	0.01	98.56

Appendix 2: Analyses of the Basalt Glass Standard VG-A99.

The following table presents the results of analyzing the natural basalt glass standard VG-A99 from Makaopuhi Lava Lake, Hawaii (Jarosewich, 1980), as an unknown during analysis of the Amsterdam-St. Paul (ASP) glasses. The analyses are unaveraged, each representing an individual analysis. If the analyses of the basalt glass standard were lower or higher than expected, then the analyses run on the ASP glasses in that same time period were corrected accordingly. The correction column indicates which if any, elements needed to be corrected. Operating conditions are listed in the text.

Run #	Standard	SiO ₂	TiO ₂	Al ₂ O ₃	FeO*	MnO	MgO	CaO	Na ₂ O	K ₂ O	P ₂ O ₅	Cr ₂ O ₃	Total	Correction
1	VG-A99/BASL	51.04	3.97	12.43	13.15	0.16	5.11	9.47	2.62	0.86	0.42	0.00	99.23	TiO ₂
1	VG-A99/BASL	51.08	3.94	12.38	13.28	0.11	5.17	9.25	2.62	0.84	0.41	0.00	99.09	TiO ₂
1	VG-A99/BASL	50.96	3.93	12.51	13.19	0.17	5.11	9.33	2.54	0.84	0.44	0.00	99.01	TiO ₂
1	VG-A99/BASL	50.99	4.01	12.25	13.42	0.12	5.11	8.94	2.53	0.86	0.38	0.00	98.60	TiO ₂
1	VG-A99/BASL	50.96	4.03	12.37	13.27	0.18	5.07	9.00	2.48	0.83	0.47	0.00	98.65	TiO ₂
1	VG-A99/BASL	50.99	3.99	12.52	13.09	0.16	5.12	9.16	2.48	0.83	0.48	0.01	98.84	TiO ₂
1	VG-A99/BASL	51.05	4.14	12.32	13.39	0.17	5.04	9.24	2.63	0.83	0.45	0.00	99.26	TiO ₂
1	VG-A99/BASL	51.05	4.14	12.39	13.24	0.21	5.09	9.07	2.46	0.85	0.52	0.00	99.02	TiO ₂
1	VG-A99/BASL	50.72	4.12	12.38	13.05	0.20	5.12	9.06	2.51	0.85	0.48	0.00	98.48	TiO ₂
1	VG-A99/BASL	51.00	4.12	12.38	13.06	0.19	5.12	9.28	2.59	0.84	0.46	0.01	99.04	TiO ₂
1	VG-A99/BASL	50.95	4.03	12.47	13.14	0.19	5.09	9.30	2.54	0.86	0.41	0.00	98.98	TiO ₂
1	VG-A99/BASL	50.83	4.15	12.37	13.49	0.17	5.14	9.07	2.67	0.84	0.42	0.00	99.16	TiO ₂
2	VG-A99/BASL	51.22	4.00	12.56	13.39	0.17	4.97	9.30	2.52	0.81	0.41	0.01	99.37	None
2	VG-A99/BASL	50.91	4.01	12.52	13.43	0.18	5.03	9.31	2.48	0.81	0.41	0.00	99.08	None
2	VG-A99/BASL	51.03	4.03	12.44	13.27	0.20	5.02	9.24	2.55	0.80	0.39	0.00	98.96	None
2	VG-A99/BASL	51.35	4.03	12.45	13.46	0.13	5.00	9.35	2.41	0.80	0.41	0.00	99.39	None
2	VG-A99/BASL	51.30	4.01	12.53	13.45	0.19	5.03	9.24	2.37	0.83	0.39	0.00	99.35	None
2	VG-A99/BASL	51.33	4.01	12.45	13.33	0.19	4.99	9.22	2.44	0.81	0.40	0.01	99.18	None
2	VG-A99/BASL	51.06	4.00	12.66	13.39	0.19	5.00	9.30	2.46	0.77	0.39	0.00	99.24	None
2	VG-A99/BASL	50.65	3.97	12.60	13.35	0.19	4.98	9.26	2.49	0.81	0.39	0.01	98.70	None
2	VG-A99/BASL	51.09	3.99	12.54	13.39	0.20	5.02	9.23	2.54	0.78	0.44	0.01	99.23	None
2	VG-A99/BASL	51.11	4.07	12.57	13.52	0.15	5.00	9.40	2.44	0.77	0.46	0.02	99.49	None
2	VG-A99/BASL	50.82	4.02	12.44	13.50	0.19	4.96	9.23	2.42	0.79	0.42	0.01	98.80	None
2	VG-A99/BASL	50.46	4.11	12.54	13.61	0.16	5.09	9.34	2.51	0.79	0.41	0.03	99.06	None

Run #	Standard	SiO ₂	TiO ₂	Al ₂ O ₃	FeO*	MnO	MgO	CaO	Na ₂ O	K ₂ O	P ₂ O ₅	Cr ₂ O ₃	Total	Correction
3	VG-A99/BASL	51.32	4.06	12.60	13.18	0.19	5.19	9.26	2.44	0.78	0.42	0.00	99.44	None
3	VG-A99/BASL	51.24	4.09	12.48	13.04	0.21	5.20	9.32	2.48	0.76	0.45	0.00	99.26	None
3	VG-A99/BASL	51.01	4.06	12.40	13.00	0.15	5.15	9.27	2.47	0.77	0.45	0.00	98.72	None
3	VG-A99/BASL	51.03	4.02	12.33	13.02	0.14	5.15	9.26	2.42	0.80	0.37	0.01	98.54	None
3	VG-A99/BASL	51.15	3.96	12.40	13.23	0.12	5.24	9.12	2.50	0.76	0.42	0.02	98.95	None
3	VG-A99/BASL	50.85	4.01	12.34	13.36	0.19	5.16	9.23	2.52	0.80	0.47	0.02	98.95	None
3	VG-A99/BASL	51.10	4.10	12.47	13.04	0.18	5.17	9.22	2.45	0.75	0.45	0.00	98.94	None
3	VG-A99/BASL	51.31	4.04	12.40	13.12	0.16	5.16	9.22	2.54	0.77	0.45	0.01	99.18	None
3	VG-A99/BASL	51.25	4.09	12.41	13.39	0.15	5.18	9.32	2.56	0.77	0.39	0.00	99.52	None
3	VG-A99/BASL	50.89	4.06	12.64	13.36	0.10	5.19	9.27	2.46	0.78	0.46	0.00	99.20	None
3	VG-A99/BASL	50.72	4.03	12.40	13.32	0.24	5.13	9.33	2.50	0.80	0.39	0.00	98.86	None
3	VG-A99/BASL	51.12	4.03	12.40	13.24	0.19	5.08	9.32	2.46	0.79	0.41	0.01	99.04	None
3	VG-A99/BASL	51.14	4.05	12.40	12.90	0.14	5.15	9.07	2.47	0.81	0.42	0.00	98.54	None
3	VG-A99/BASL	51.04	3.99	12.46	13.30	0.20	5.15	9.28	2.48	0.79	0.38	0.00	99.07	None
3	VG-A99/BASL	51.05	4.07	12.43	13.30	0.18	5.15	9.26	2.55	0.78	0.43	0.00	99.20	None
3	VG-A99/BASL	51.04	4.01	12.34	13.04	0.18	5.13	9.04	2.51	0.79	0.45	0.00	98.52	None
3	VG-A99/BASL	51.32	3.95	12.48	13.23	0.19	5.18	9.21	2.48	0.77	0.37	0.01	99.19	None
3	VG-A99/BASL	50.84	4.12	12.47	13.21	0.14	5.16	9.08	2.38	0.77	0.41	0.02	98.59	None
4	VG-A99/BASL	50.62	4.03	12.44	13.05	0.19	5.13	9.44	2.51	0.84	0.45	0.01	98.72	None
4	VG-A99/BASL	50.64	3.97	12.37	13.21	0.22	5.21	9.32	2.49	0.84	0.42	0.01	98.69	None
4	VG-A99/BASL	50.60	3.98	12.38	12.96	0.19	5.16	9.32	2.59	0.83	0.41	0.02	98.43	None
4	VG-A99/BASL	50.62	4.01	12.43	13.43	0.14	5.19	9.30	2.58	0.83	0.44	0.01	98.98	None
4	VG-A99/BASL	50.82	3.97	12.44	13.23	0.18	5.22	9.23	2.55	0.87	0.45	0.02	98.98	None
4	VG-A99/BASL	50.80	4.05	12.51	13.63	0.24	5.10	9.34	2.56	0.84	0.42	0.02	99.50	None

Run #	Standard	SiO ₂	TiO ₂	Al ₂ O ₃	FeO*	MnO	MgO	CaO	Na ₂ O	K ₂ O	P ₂ O ₅	Cr ₂ O ₃	Total	Correction
4	VG-A99/BASL	50.74	4.03	12.38	13.34	0.16	5.11	9.22	2.58	0.87	0.43	0.00	98.86	None
4	VG-A99/BASL	50.52	4.09	12.42	13.30	0.17	5.16	9.28	2.60	0.85	0.47	0.02	98.89	None
4	VG-A99/BASL	50.61	4.07	12.36	13.29	0.18	5.08	9.23	2.54	0.85	0.47	0.01	98.69	None
4	VG-A99/BASL	51.21	4.08	12.54	13.43	0.19	5.18	9.12	2.60	0.85	0.45	0.00	99.64	None
4	VG-A99/BASL	50.98	4.06	12.58	13.37	0.17	5.13	9.30	2.47	0.87	0.45	0.01	99.40	None
4	VG-A99/BASL	50.88	4.09	12.40	13.46	0.18	5.04	9.21	2.50	0.87	0.46	0.01	99.10	None
4	VG-A99/BASL	50.95	4.07	12.39	13.30	0.15	4.97	9.19	2.52	0.86	0.47	0.01	98.88	None
4	VG-A99/BASL	50.86	4.03	12.30	12.99	0.25	4.98	9.13	2.57	0.84	0.47	0.02	98.44	None
4	VG-A99/BASL	50.80	4.04	12.35	13.17	0.20	5.04	9.11	2.62	0.86	0.42	0.02	98.62	None
4	VG-A99/BASL	50.79	4.03	12.36	13.27	0.18	5.09	9.12	2.64	0.85	0.46	0.00	98.78	None
4	VG-A99/BASL	50.91	4.04	12.32	13.37	0.22	5.09	9.21	2.52	0.85	0.41	0.00	98.94	None
4	VG-A99/BASL	50.90	4.07	12.40	13.33	0.19	5.02	9.09	2.51	0.85	0.42	0.00	98.79	None
4	VG-A99/BASL	50.86	4.02	12.41	13.42	0.15	5.16	9.29	2.52	0.85	0.44	0.01	99.14	None
4	VG-A99/BASL	50.97	4.01	12.38	13.47	0.19	5.10	9.21	2.59	0.86	0.42	0.01	99.20	None
4	VG-A99/BASL	50.84	3.93	12.52	13.47	0.24	5.17	9.19	2.44	0.87	0.48	0.02	99.16	None
5	VG-A99/BASL	50.93	3.93	12.42	13.42	0.22	5.15	9.24	2.55	0.85	0.42	0.02	99.15	FeO*
5	VG-A99/BASL	50.96	4.01	12.46	13.36	0.22	5.20	9.34	2.55	0.86	0.43	0.01	99.40	FeO*
5	VG-A99/BASL	51.12	4.01	12.50	13.26	0.13	5.17	9.33	2.63	0.85	0.44	0.02	99.47	FeO*
5	VG-A99/BASL	50.83	4.12	12.40	13.21	0.20	5.11	9.54	2.55	0.81	0.42	0.01	99.20	FeO*
5	VG-A99/BASL	50.98	4.12	12.43	13.38	0.18	5.09	9.32	2.52	0.85	0.36	0.01	99.25	FeO*
5	VG-A99/BASL	50.75	3.99	12.38	13.27	0.21	5.12	9.29	2.66	0.87	0.46	0.00	99.01	FeO*
5	VG-A99/BASL	51.08	4.08	12.39	13.64	0.20	5.17	9.36	2.55	0.84	0.44	0.00	99.75	FeO*
5	VG-A99/BASL	50.91	4.06	12.56	13.20	0.19	5.19	9.37	2.57	0.86	0.46	0.00	99.37	FeO*
5	VG-A99/BASL	51.09	4.04	12.48	13.52	0.19	5.15	9.37	2.54	0.85	0.44	0.00	99.67	FeO*

Run #	Standard	SiO ₂	TiO ₂	Al ₂ O ₃	FeO*	MnO	MgO	CaO	Na ₂ O	K ₂ O	P ₂ O ₅	Cr ₂ O ₃	Total	Correction
5	VG-A99/BASL	51.04	4.03	12.54	13.25	0.18	5.10	9.25	2.60	0.88	0.44	0.00	99.32	FeO*
5	VG-A99/BASL	50.90	4.04	12.44	13.32	0.21	5.06	9.24	2.59	0.87	0.43	0.00	99.08	FeO*
5	VG-A99/BASL	50.98	4.11	12.53	13.34	0.20	5.17	9.26	2.54	0.87	0.41	0.00	99.41	FeO*
5	VG-A99/BASL	51.04	4.13	12.46	13.28	0.19	5.11	9.41	2.57	0.86	0.44	0.01	99.51	FeO*
5	VG-A99/BASL	50.94	4.11	12.43	13.14	0.19	5.12	9.38	2.58	0.86	0.51	0.02	99.28	FeO*
5	VG-A99/BASL	50.83	4.03	12.56	13.22	0.16	5.14	9.26	2.47	0.85	0.41	0.01	98.94	FeO*
5	VG-A99/BASL	50.83	4.08	12.47	13.39	0.12	5.13	9.31	2.53	0.83	0.38	0.01	99.07	FeO*
5	VG-A99/BASL	51.22	4.00	12.52	13.04	0.17	5.11	9.43	2.51	0.85	0.45	0.00	99.31	FeO*
5	VG-A99/BASL	50.92	4.06	12.45	13.14	0.19	5.18	9.27	2.59	0.87	0.43	0.00	99.11	FeO*
6	VG-A99/BASL	51.28	4.04	12.57	13.42	0.21	5.13	9.26	2.51	0.83	0.42	0.01	99.68	FeO*
6	VG-A99/BASL	51.15	4.06	12.54	13.28	0.19	5.18	9.27	2.63	0.85	0.44	0.01	99.59	FeO*
6	VG-A99/BASL	51.10	4.02	12.60	13.28	0.21	5.11	9.39	2.54	0.84	0.42	0.02	99.54	FeO*
6	VG-A99/BASL	51.13	4.08	12.55	13.32	0.21	5.01	9.29	2.44	0.87	0.43	0.02	99.34	FeO*
6	VG-A99/BASL	50.91	4.05	12.54	13.34	0.19	5.00	9.32	2.71	0.85	0.44	0.00	99.36	FeO*
6	VG-A99/BASL	51.00	4.04	12.54	13.36	0.19	5.05	9.33	2.65	0.85	0.44	0.04	99.49	FeO*
6	VG-A99/BASL	51.16	4.13	12.60	13.45	0.23	5.01	9.25	2.56	0.85	0.45	0.00	99.69	FeO*
6	VG-A99/BASL	51.07	4.06	12.52	13.27	0.22	5.08	9.21	2.54	0.85	0.52	0.00	99.34	FeO*
6	VG-A99/BASL	50.95	4.06	12.54	13.26	0.14	5.03	9.28	2.47	0.89	0.49	0.00	99.11	FeO*
6	VG-A99/BASL	51.05	4.06	12.47	13.23	0.18	5.10	9.36	2.61	0.86	0.48	0.00	99.42	FeO*
6	VG-A99/BASL	51.04	4.01	12.51	13.17	0.19	5.05	9.36	2.57	0.84	0.47	0.01	99.23	FeO*
6	VG-A99/BASL	50.84	3.97	12.46	13.25	0.21	5.07	9.32	2.56	0.86	0.42	0.00	98.96	FeO*
6	VG-A99/BASL	51.22	4.07	12.52	13.34	0.18	5.07	9.33	2.48	0.85	0.49	0.01	99.54	FeO*
6	VG-A99/BASL	51.21	4.02	12.52	13.30	0.19	5.10	9.24	2.56	0.86	0.43	0.01	99.43	FeO*
6	VG-A99/BASL	51.11	4.04	12.49	13.22	0.24	5.04	9.26	2.50	0.85	0.45	0.01	99.22	FeO*

Run #	Standard	SiO ₂	TiO ₂	Al ₂ O ₃	FeO*	MnO	MgO	CaO	Na ₂ O	K ₂ O	P ₂ O ₅	Cr ₂ O ₃	Total	Correction
7	VG-A99/BASL	50.71	4.08	12.36	13.32	0.15	4.97	9.41	2.61	0.88	0.44	0.00	98.93	None
7	VG-A99/BASL	50.72	4.10	12.41	13.23	0.25	5.03	9.31	2.60	0.85	0.46	0.00	98.96	None
7	VG-A99/BASL	50.75	4.05	12.41	13.44	0.21	5.07	9.43	2.58	0.86	0.45	0.01	99.26	None
7	VG-A99/BASL	50.66	4.07	12.30	13.24	0.21	5.10	9.35	2.49	0.86	0.46	0.00	98.75	None
7	VG-A99/BASL	50.88	4.02	12.23	13.51	0.11	5.13	9.26	2.58	0.86	0.48	0.00	99.04	None
7	VG-A99/BASL	50.62	4.17	12.28	13.46	0.20	5.06	9.38	2.49	0.84	0.49	0.00	99.00	None
7	VG-A99/BASL	50.77	4.08	12.28	13.61	0.20	5.18	9.23	2.56	0.81	0.43	0.02	99.16	None
7	VG-A99/BASL	50.80	4.08	12.30	13.37	0.18	5.15	9.24	2.67	0.86	0.45	0.02	99.11	None
7	VG-A99/BASL	50.78	4.12	12.28	13.53	0.17	5.16	9.41	2.61	0.86	0.44	0.01	99.36	None
8	VG-A99/BASL	50.50	3.92	12.45	13.35	0.17	5.16	9.17	2.61	0.85	0.48	0.01	98.67	FeO*
8	VG-A99/BASL	50.55	3.98	12.43	13.39	0.14	5.12	9.16	2.58	0.87	0.40	0.00	98.64	FeO*
8	VG-A99/BASL	50.63	4.01	12.30	13.38	0.21	5.13	9.24	2.61	0.88	0.44	0.00	98.82	FeO*
8	VG-A99/BASL	50.46	4.01	12.29	13.23	0.19	5.13	9.23	2.58	0.87	0.49	0.02	98.50	FeO*
8	VG-A99/BASL	50.82	3.94	12.37	13.22	0.12	5.02	9.31	2.62	0.88	0.47	0.01	98.78	FeO*
8	VG-A99/BASL	50.56	3.97	12.35	13.22	0.21	4.99	9.20	2.66	0.91	0.54	0.01	98.61	FeO*

Appendix 3: Analyses of the Basalt Glass Standard IOB.

The following table presents the results of analyzing the Indian Ocean basalt glass standard USNM 113716 (Jarosewich, 1980), as an unknown during analysis of the Amsterdam-St. Paul glasses. This standard was analyzed concurrently with VG-A99 to monitor the consistency between analyses run on different days. The analyses are unaveraged and each represents an individual analysis. Operating conditions are listed in the text.

Run #	Standard	SiO ₂	TiO ₂	Al ₂ O ₃	FeO*	MnO	MgO	CaO	Na ₂ O	K ₂ O	P ₂ O ₅	Cr ₂ O ₃	Total
1	USNM 113716/IOB	51.24	1.28	15.11	9.01	0.11	8.12	11.28	2.52	0.07	0.11	0.03	98.88
1	USNM 113716/IOB	51.19	1.38	15.21	9.11	0.11	8.13	11.54	2.52	0.07	0.15	0.04	99.46
1	USNM 113716/IOB	50.95	1.36	15.13	9.09	0.18	8.20	11.40	2.55	0.07	0.12	0.04	99.09
1	USNM 113716/IOB	51.30	1.33	15.13	8.95	0.11	8.09	11.21	2.55	0.08	0.14	0.02	98.89
1	USNM 113716/IOB	51.13	1.31	15.21	9.05	0.14	8.21	11.07	2.49	0.09	0.12	0.05	98.86
1	USNM 113716/IOB	51.40	1.30	15.12	9.05	0.14	8.16	11.11	2.51	0.08	0.12	0.05	99.04
1	USNM 113716/IOB	51.20	1.29	15.19	8.92	0.15	8.09	11.03	2.55	0.07	0.11	0.04	98.62
1	USNM 113716/IOB	51.25	1.28	15.02	9.02	0.16	8.10	11.04	2.45	0.07	0.10	0.02	98.52
1	USNM 113716/IOB	51.12	1.30	15.15	8.93	0.10	8.08	11.18	2.50	0.09	0.15	0.05	98.64
1	USNM 113716/IOB	51.33	1.34	15.25	9.07	0.17	8.10	11.17	2.56	0.08	0.11	0.04	99.22
1	USNM 113716/IOB	51.45	1.35	15.25	9.16	0.13	8.14	11.01	2.59	0.07	0.14	0.05	99.34
1	USNM 113716/IOB	51.49	1.35	15.12	9.14	0.16	8.17	11.15	2.48	0.08	0.18	0.04	99.37
1	USNM 113716/IOB	51.30	1.27	15.23	8.87	0.15	8.09	10.90	2.40	0.08	0.14	0.03	98.46
1	USNM 113716/IOB	51.40	1.28	15.18	9.08	0.15	8.08	10.89	2.44	0.08	0.12	0.03	98.72
1	USNM 113716/IOB	51.44	1.27	15.21	8.99	0.17	8.16	11.07	2.42	0.07	0.13	0.03	98.97
1	USNM 113716/IOB	51.36	1.29	15.10	9.10	0.16	8.14	10.87	2.44	0.08	0.13	0.04	98.73
1	USNM 113716/IOB	51.27	1.32	15.16	9.03	0.12	8.08	10.98	2.55	0.08	0.13	0.03	98.75
1	USNM 113716/IOB	51.38	1.29	15.35	9.04	0.15	8.10	10.95	2.49	0.08	0.13	0.05	99.02
2	USNM 113716/IOB	51.10	1.33	15.12	9.32	0.16	7.89	11.41	2.35	0.08	0.10	0.03	98.89
2	USNM 113716/IOB	51.01	1.32	15.07	9.22	0.14	7.83	11.50	2.41	0.07	0.09	0.03	98.70
2	USNM 113716/IOB	50.80	1.33	15.04	9.38	0.17	7.84	11.38	2.40	0.08	0.13	0.04	98.59
2	USNM 113716/IOB	50.79	1.33	15.17	9.21	0.18	7.90	11.57	2.40	0.08	0.10	0.04	98.77
2	USNM 113716/IOB	50.50	1.32	15.13	9.18	0.15	8.08	11.29	2.39	0.08	0.08	0.05	98.25
2	USNM 113716/IOB	50.73	1.31	15.25	9.31	0.14	8.01	11.55	2.42	0.08	0.10	0.05	98.94

Run #	Standard	SiO ₂	TiO ₂	Al ₂ O ₃	FeO*	MnO	MgO	CaO	Na ₂ O	K ₂ O	P ₂ O ₅	Cr ₂ O ₃	Total
2	USNM 113716/IOB	51.53	1.32	15.34	9.16	0.14	8.09	11.31	2.39	0.07	0.11	0.04	99.51
2	USNM 113716/IOB	51.24	1.31	15.34	9.01	0.15	8.15	11.51	2.49	0.07	0.12	0.05	99.44
2	USNM 113716/IOB	51.15	1.32	15.25	9.39	0.16	8.11	11.29	2.40	0.07	0.12	0.05	99.31
2	USNM 113716/IOB	51.54	1.33	15.18	9.05	0.13	8.04	11.43	2.36	0.08	0.14	0.03	99.31
2	USNM 113716/IOB	51.62	1.29	15.06	9.21	0.15	8.01	11.40	2.50	0.08	0.13	0.04	99.49
2	USNM 113716/IOB	50.79	1.35	15.19	9.17	0.18	8.01	11.41	2.46	0.07	0.08	0.03	98.74
2	USNM 113716/IOB	51.63	1.29	15.37	9.09	0.14	8.03	11.13	2.44	0.08	0.11	0.06	99.37
2	USNM 113716/IOB	51.37	1.28	15.25	9.19	0.15	8.06	11.33	2.42	0.06	0.10	0.05	99.25
2	USNM 113716/IOB	51.65	1.27	15.32	9.21	0.16	8.04	11.34	2.46	0.07	0.10	0.04	99.66
2	USNM 113716/IOB	51.42	1.28	15.27	9.28	0.14	8.10	11.50	2.33	0.08	0.09	0.05	99.55
2	USNM 113716/IOB	51.68	1.28	15.26	9.24	0.14	8.12	11.21	2.51	0.07	0.10	0.04	99.66
2	USNM 113716/IOB	51.99	1.31	15.30	9.28	0.13	8.09	11.53	2.55	0.07	0.12	0.05	100.41
2	USNM 113716/IOB	51.76	1.31	15.32	9.04	0.19	8.20	11.48	2.44	0.06	0.12	0.04	99.94
2	USNM 113716/IOB	51.57	1.32	15.38	9.15	0.14	8.15	11.39	2.48	0.07	0.11	0.03	99.79
2	USNM 113716/IOB	51.67	1.36	15.55	9.27	0.12	8.05	11.33	2.58	0.08	0.12	0.04	100.16
3	USNM 113716/IOB	51.44	1.31	15.08	8.98	0.18	8.16	11.44	2.53	0.07	0.13	0.04	99.37
3	USNM 113716/IOB	51.24	1.34	15.02	8.95	0.16	8.27	11.40	2.43	0.07	0.14	0.04	99.07
3	USNM 113716/IOB	51.04	1.31	15.11	9.15	0.09	8.22	11.60	2.54	0.07	0.16	0.03	99.31
3	USNM 113716/IOB	51.62	1.34	15.18	9.03	0.15	8.23	11.38	2.53	0.08	0.13	0.06	99.72
3	USNM 113716/IOB	51.17	1.31	15.17	8.94	0.18	8.30	11.34	2.51	0.07	0.11	0.06	99.17
3	USNM 113716/IOB	51.28	1.31	15.30	9.00	0.15	8.26	11.32	2.57	0.07	0.10	0.05	99.40
3	USNM 113716/IOB	51.57	1.34	15.18	8.97	0.13	8.23	11.31	2.54	0.07	0.12	0.03	99.49
3	USNM 113716/IOB	51.13	1.38	15.16	9.03	0.16	8.28	11.38	2.44	0.08	0.09	0.03	99.16
3	USNM 113716/IOB	51.45	1.29	15.26	9.02	0.13	8.18	11.27	2.48	0.07	0.11	0.03	99.29

Run #	Standard	SiO ₂	TiO ₂	Al ₂ O ₃	FeO*	MnO	MgO	CaO	Na ₂ O	K ₂ O	P ₂ O ₅	Cr ₂ O ₃	Total
3	USNM 113716/IOB	51.20	1.35	15.12	9.14	0.16	8.37	11.42	2.53	0.07	0.11	0.05	99.50
3	USNM 113716/IOB	51.35	1.33	15.14	8.95	0.16	8.22	11.30	2.52	0.06	0.12	0.04	99.20
3	USNM 113716/IOB	51.27	1.32	15.23	9.06	0.15	8.23	11.39	2.49	0.08	0.12	0.05	99.40
3	USNM 113716/IOB	51.53	1.35	15.11	9.04	0.16	8.30	11.34	2.55	0.08	0.14	0.04	99.62
3	USNM 113716/IOB	51.70	1.37	15.34	9.12	0.16	8.13	11.27	2.56	0.07	0.12	0.04	99.89
3	USNM 113716/IOB	51.41	1.32	15.29	9.03	0.17	8.31	11.44	2.45	0.09	0.14	0.05	99.70
4	USNM 113716/IOB	50.98	1.32	15.09	9.12	0.16	8.18	11.26	2.54	0.09	0.14	0.05	98.93
4	USNM 113716/IOB	51.17	1.30	15.19	8.96	0.16	8.21	11.43	2.54	0.09	0.13	0.04	99.22
4	USNM 113716/IOB	51.17	1.29	15.14	9.01	0.16	8.26	11.44	2.59	0.08	0.11	0.04	99.29
4	USNM 113716/IOB	51.25	1.36	15.14	9.20	0.13	8.07	11.25	2.52	0.08	0.10	0.06	99.15
4	USNM 113716/IOB	51.26	1.30	15.26	9.23	0.14	8.15	11.37	2.60	0.08	0.15	0.04	99.57
4	USNM 113716/IOB	51.34	1.33	15.07	9.21	0.13	8.13	11.29	2.44	0.08	0.10	0.04	99.18
4	USNM 113716/IOB	51.08	1.38	15.09	9.08	0.15	8.10	11.16	2.55	0.07	0.12	0.04	98.82
4	USNM 113716/IOB	51.33	1.33	15.17	9.03	0.18	8.18	11.29	2.48	0.09	0.12	0.05	99.26
4	USNM 113716/IOB	51.32	1.33	15.12	8.85	0.16	8.14	11.26	2.46	0.08	0.12	0.04	98.88
4	USNM 113716/IOB	51.29	1.34	15.25	9.25	0.20	8.15	11.34	2.55	0.08	0.16	0.04	99.64
4	USNM 113716/IOB	51.47	1.33	15.11	9.34	0.17	8.19	11.31	2.55	0.08	0.16	0.05	99.77
4	USNM 113716/IOB	51.14	1.34	15.31	9.31	0.17	8.12	11.26	2.56	0.08	0.12	0.05	99.46
4	USNM 113716/IOB	51.56	1.34	15.10	9.13	0.15	8.11	11.30	2.52	0.09	0.11	0.03	99.43
4	USNM 113716/IOB	51.48	1.30	14.97	9.20	0.17	7.98	11.20	2.54	0.08	0.12	0.05	99.09
4	USNM 113716/IOB	51.58	1.33	15.16	9.07	0.16	8.02	11.24	2.45	0.07	0.11	0.03	99.22
5	USNM 113716/IOB	51.52	1.35	15.08	8.98	0.17	8.15	11.45	2.55	0.08	0.13	0.03	99.48
5	USNM 113716/IOB	51.54	1.33	15.23	9.07	0.15	8.15	11.52	2.57	0.09	0.12	0.02	99.79
5	USNM 113716/IOB	51.42	1.30	15.23	9.19	0.10	8.19	11.38	2.56	0.08	0.16	0.01	99.63

Run #	Standard	SiO ₂	TiO ₂	Al ₂ O ₃	FeO*	MnO	MgO	CaO	Na ₂ O	K ₂ O	P ₂ O ₅	Cr ₂ O ₃	Total
5	USNM 113716/LOB	51.25	1.34	15.19	9.00	0.14	8.22	11.46	2.55	0.08	0.11	0.06	99.40
5	USNM 113716/LOB	50.99	1.33	15.24	8.94	0.11	8.15	11.57	2.49	0.09	0.11	0.04	99.06
5	USNM 113716/LOB	51.44	1.37	15.19	9.02	0.17	8.31	11.52	2.52	0.08	0.09	0.05	99.74
5	USNM 113716/LOB	51.36	1.33	15.25	9.10	0.26	8.18	11.46	2.58	0.08	0.12	0.06	99.77
5	USNM 113716/LOB	51.36	1.32	15.27	9.27	0.18	8.27	11.47	2.62	0.08	0.07	0.04	99.95
5	USNM 113716/LOB	51.38	1.35	15.29	9.35	0.13	8.36	11.31	2.54	0.08	0.09	0.05	99.95
5	USNM 113716/LOB	51.58	1.35	15.23	8.96	0.16	8.18	11.54	2.59	0.08	0.13	0.04	99.84
5	USNM 113716/LOB	51.56	1.34	15.29	9.25	0.14	8.20	11.52	2.66	0.07	0.13	0.04	100.21
5	USNM 113716/LOB	51.76	1.34	15.22	8.97	0.19	8.11	11.45	2.45	0.08	0.13	0.03	99.72
5	USNM 113716/LOB	51.36	1.30	15.36	9.08	0.20	8.19	11.46	2.64	0.07	0.12	0.04	99.81
5	USNM 113716/LOB	51.56	1.33	15.25	9.05	0.13	8.17	11.52	2.54	0.08	0.12	0.05	99.79
5	USNM 113716/LOB	51.39	1.32	15.24	9.03	0.15	8.21	11.55	2.64	0.09	0.14	0.06	99.81
5	USNM 113716/LOB	51.36	1.27	15.25	9.07	0.20	8.16	11.35	2.60	0.09	0.12	0.03	99.50
5	USNM 113716/LOB	51.19	1.39	15.08	9.12	0.14	8.24	11.60	2.47	0.08	0.13	0.02	99.45
5	USNM 113716/LOB	51.14	1.34	15.11	8.97	0.17	8.11	11.36	2.58	0.07	0.13	0.04	99.02
6	USNM 113716/LOB	51.25	1.36	15.20	9.09	0.12	7.94	11.58	2.51	0.07	0.09	0.05	99.25
6	USNM 113716/LOB	51.41	1.33	15.27	9.13	0.19	7.99	11.42	2.53	0.08	0.11	0.05	99.51
6	USNM 113716/LOB	51.36	1.31	15.21	9.16	0.12	8.00	11.54	2.53	0.07	0.11	0.04	99.44
6	USNM 113716/LOB	51.35	1.35	15.30	9.16	0.15	8.10	11.34	2.59	0.09	0.13	0.03	99.59
6	USNM 113716/LOB	51.68	1.33	15.35	9.05	0.15	8.12	11.36	2.64	0.09	0.10	0.04	99.91
6	USNM 113716/LOB	51.39	1.36	15.19	9.20	0.20	8.04	11.45	2.62	0.07	0.11	0.05	99.66
6	USNM 113716/LOB	51.16	1.32	15.06	9.06	0.15	8.12	11.55	2.53	0.07	0.13	0.04	99.18
6	USNM 113716/LOB	50.95	1.31	15.09	9.26	0.17	8.12	11.47	2.58	0.08	0.14	0.06	99.21
6	USNM 113716/LOB	51.07	1.29	14.96	9.00	0.18	8.08	11.40	2.53	0.07	0.12	0.03	98.75

Run #	Standard	SiO ₂	TiO ₂	Al ₂ O ₃	FeO*	MnO	MgO	CaO	Na ₂ O	K ₂ O	P ₂ O ₅	Cr ₂ O ₃	Total
6	USNM 113716/LOB	51.11	1.32	15.10	9.00	0.14	8.02	11.55	2.61	0.08	0.13	0.03	99.08
6	USNM 113716/LOB	51.36	1.31	15.10	9.13	0.13	8.08	11.41	2.58	0.07	0.13	0.04	99.33
6	USNM 113716/LOB	51.20	1.37	15.04	8.99	0.19	7.98	11.39	2.55	0.08	0.10	0.04	98.94
6	USNM 113716/LOB	51.17	1.32	14.92	9.19	0.15	7.95	11.44	2.62	0.08	0.14	0.04	99.02
6	USNM 113716/LOB	51.50	1.34	15.09	9.04	0.16	8.03	11.42	2.61	0.08	0.12	0.04	99.44
6	USNM 113716/LOB	51.25	1.31	14.94	9.02	0.15	7.97	11.33	2.65	0.09	0.14	0.03	98.87
7	USNM 113716/LOB	51.43	1.40	15.16	9.02	0.15	8.11	11.47	2.62	0.07	0.15	0.05	99.64
7	USNM 113716/LOB	51.30	1.30	15.18	9.33	0.16	8.30	11.56	2.58	0.08	0.11	0.03	99.93
7	USNM 113716/LOB	51.76	1.41	15.15	9.34	0.13	8.36	11.56	2.58	0.08	0.11	0.04	100.50
7	USNM 113716/LOB	51.11	1.35	14.90	9.30	0.13	8.22	11.39	2.56	0.08	0.13	0.03	99.20
7	USNM 113716/LOB	51.06	1.36	14.79	9.43	0.19	8.22	11.61	2.68	0.08	0.13	0.05	99.59
7	USNM 113716/LOB	50.78	1.35	14.85	9.26	0.17	8.29	11.47	2.54	0.08	0.12	0.03	98.92
7	USNM 113716/LOB	51.11	1.37	14.95	9.35	0.13	8.21	11.46	2.61	0.08	0.10	0.05	99.43
7	USNM 113716/LOB	50.92	1.39	15.01	9.39	0.16	8.17	11.66	2.56	0.08	0.10	0.05	99.49
7	USNM 113716/LOB	50.88	1.38	14.89	9.28	0.14	8.24	11.51	2.61	0.08	0.12	0.03	99.15
8	USNM 113716/LOB	51.65	1.36	15.22	9.34	0.17	8.25	11.50	2.61	0.08	0.11	0.06	100.34
8	USNM 113716/LOB	51.60	1.34	15.13	9.27	0.14	8.17	11.50	2.60	0.08	0.10	0.05	99.99
8	USNM 113716/LOB	51.37	1.34	15.13	9.34	0.16	8.38	11.53	2.60	0.08	0.14	0.05	100.11
8	USNM 113716/LOB	51.49	1.35	15.22	9.48	0.13	8.34	11.56	2.63	0.09	0.13	0.05	100.45
8	USNM 113716/LOB	51.50	1.33	15.20	9.33	0.19	8.39	11.52	2.65	0.08	0.10	0.04	100.32
8	USNM 113716/LOB	51.77	1.38	15.27	9.33	0.17	8.29	11.52	2.66	0.08	0.14	0.04	100.64

Appendix 4: Unaveraged Chlorine and Sulfur Data.

When ASP samples were analyzed for chlorine and sulfur, two points were analyzed on each sample, then averaged together to represent the Cl and S contents of one of the 126 chemical groups. The exception to this was in the first run in which 3 points, rather than two were analyzed. This table presents each of the individual chlorine and sulfur analyses before averaging. Operating conditions are listed in the text. The corrected Cl column is the Cl content of the glass adjusted for the background level of Cl, as discussed in the Methods section.

Group	Sample	SiO ₂	TiO ₂	Al ₂ O ₃	FeO*	MnO	MgO	CaO	Na ₂ O	K ₂ O	P ₂ O ₅	Cr ₂ O ₃	S	Cl	Total	Corrected Cl
1	d33-1	50.31	1.57	15.29	9.84	0.17	7.86	12.17	2.73	0.14	0.13	0.03	0.1077	0.0147	100.37	0.0132
1	d33-1	51.17	1.63	15.26	9.66	0.18	7.98	12.18	2.70	0.14	0.14	0.04	0.1046	0.0144	101.18	0.0129
4	d34-1	51.84	1.87	14.34	11.33	0.23	6.99	11.13	2.97	0.20	0.17	0.02	0.1328	0.0048	101.23	0.0033
4	d34-1	51.91	1.92	14.30	11.21	0.19	6.79	11.12	3.13	0.20	0.17	0.01	0.1395	0.0055	101.09	0.0040
20	w10c	50.78	1.54	14.60	10.47	0.18	7.69	12.01	2.56	0.17	0.16	0.05	0.1336	0.0139	100.37	0.0097
20	w10c	50.94	1.56	14.58	10.54	0.16	7.69	11.94	2.69	0.16	0.14	0.03	0.1308	0.0123	100.58	0.0081
21	d39-3	51.23	1.24	15.38	9.05	0.14	8.15	12.57	2.46	0.12	0.10	0.04	0.1070	0.0132	100.61	0.0090
21	d39-3	51.28	1.22	15.24	9.16	0.21	8.26	12.61	2.33	0.11	0.12	0.07	0.1058	0.0114	100.71	0.0072
36	d43-2	50.78	1.37	15.72	9.34	0.15	8.44	12.29	2.68	0.07	0.13	0.04	0.1191	0.0043	101.14	0.0001
36	d43-2	51.00	1.39	15.59	9.48	0.15	8.57	12.12	2.78	0.08	0.10	0.05	0.1094	0.0056	101.42	0.0014
40	d44-2	51.22	1.36	14.74	10.53	0.24	7.44	12.04	2.77	0.11	0.12	0.04	0.1148	0.0053	100.73	0.0038
40	d44-2	51.73	1.33	14.79	10.52	0.16	7.63	12.04	2.66	0.11	0.14	0.04	0.1235	0.0054	101.26	0.0039
47	d47-6	50.42	1.08	15.67	9.17	0.16	8.52	12.63	2.37	0.14	0.10	0.06	0.0897	0.0057	100.41	0.0042
47	d47-6	51.23	1.06	15.82	9.37	0.13	8.21	12.58	2.41	0.14	0.08	0.06	0.0888	0.0054	101.17	0.0039
48	d48-2	49.43	1.19	15.98	9.98	0.16	8.07	11.56	2.40	0.15	0.09	0.04	0.096	0.0134	99.16	0.0119
48	d48-2	49.83	1.18	15.95	10.00	0.10	8.24	11.62	2.38	0.16	0.12	0.05	0.1047	0.0141	99.75	0.0126
49	d49-1	51.15	1.68	14.20	11.42	0.16	6.25	10.55	2.90	0.33	0.17	0.03	0.1288	0.0292	99.00	0.0277
49	d49-1	51.47	1.75	14.19	11.44	0.22	6.40	10.84	2.78	0.32	0.20	0.03	0.1224	0.0285	99.79	0.0270
50	d49-3	51.51	2.85	12.50	16.30	0.30	3.93	8.18	3.15	0.55	0.29	0.02	0.1995	0.1498	99.92	0.1483
50	d49-3	51.68	2.88	12.49	16.07	0.22	4.01	8.21	3.14	0.54	0.32	0.01	0.1983	0.1527	99.92	0.1512
66	d55	51.23	1.35	15.01	9.66	0.11	7.75	12.08	2.55	0.27	0.13	0.04	0.0941	0.0087	100.28	0.0072
66	d55	51.65	1.36	15.15	9.60	0.16	7.65	11.95	2.59	0.26	0.14	0.03	0.1046	0.0085	100.64	0.0070
68	w30a	51.53	1.76	14.73	10.30	0.21	7.01	11.28	2.77	0.37	0.19	0.03	0.1163	0.0156	100.31	0.0141
68	w30a	51.41	1.74	14.73	10.22	0.22	6.89	11.33	2.78	0.36	0.18	0.04	0.1264	0.0142	100.03	0.0127

Group	Sample	SiO ₂	TiO ₂	Al ₂ O ₃	FeO*	MnO	MgO	CaO	Na ₂ O	K ₂ O	P ₂ O ₅	Cr ₂ O ₃	S	Cl	Total	Corrected Cl
75	w32a	51.10	1.40	15.13	10.34	0.21	8.23	10.90	2.70	0.25	0.17	0.04	0.1089	0.0119	100.60	0.0104
75	w32a	50.64	1.42	15.28	10.30	0.19	8.26	11.03	2.64	0.25	0.12	0.05	0.1071	0.012	100.30	0.0105
84	d64-6	52.03	1.82	14.87	10.39	0.18	6.36	10.73	2.79	0.66	0.25	0.02	0.1259	0.0699	100.30	0.0684
84	d64-6	52.38	1.80	14.88	10.46	0.13	6.28	10.76	2.74	0.63	0.24	0.01	0.1208	0.0695	100.49	0.0680
84	d64-6	52.18	1.84	14.87	10.54	0.10	6.27	10.79	2.67	0.61	0.24	0.00	0.1290	0.0707	100.33	0.0692
84	d64-8	52.11	1.91	14.92	10.75	0.20	6.23	10.65	2.85	0.67	0.25	0.03	0.1238	0.0728	100.78	0.0713
84	d64-8	52.18	1.87	14.88	10.75	0.21	6.24	10.56	2.80	0.66	0.23	0.01	0.1423	0.0689	100.60	0.0674
84	d64-8	52.22	1.87	14.93	10.76	0.16	6.19	10.51	2.74	0.65	0.25	0.01	0.1121	0.0679	100.47	0.0664
85	d64-2	53.36	1.96	14.67	10.98	0.17	5.15	9.27	3.02	0.81	0.32	0.00	0.1074	0.1246	99.95	0.1231
85	d64-2	53.25	1.99	14.77	10.72	0.14	5.22	9.30	3.07	0.80	0.31	0.02	0.0946	0.1219	99.80	0.1204
85	d64-2	53.38	1.88	14.74	10.71	0.15	5.17	9.25	3.03	0.79	0.32	0.03	0.0957	0.1246	99.66	0.1231
85	d64-4	53.49	1.95	14.74	10.78	0.19	5.23	9.24	3.04	0.78	0.26	0.03	0.1204	0.1217	99.99	0.1202
85	d64-4	53.10	1.86	14.52	10.68	0.17	5.17	9.25	3.13	0.75	0.28	0.02	0.1092	0.1207	99.17	0.1192
85	d64-4	53.16	1.87	14.71	10.61	0.15	5.26	9.38	3.07	0.82	0.30	0.02	0.1210	0.1237	99.58	0.1222
86	w38a	50.61	1.41	14.87	9.99	0.19	7.69	12.13	2.36	0.27	0.17	0.05	0.1183	0.0241	99.88	0.0226
86	w38a	50.33	1.44	15.03	9.93	0.14	7.62	12.23	2.38	0.27	0.17	0.02	0.1186	0.0254	99.70	0.0239
93	d70-4	50.96	1.17	15.24	9.09	0.20	8.19	12.77	2.31	0.23	0.13	0.05	0.0941	0.0132	100.45	0.0117
93	d70-4	50.43	1.13	15.07	9.03	0.11	8.17	12.62	2.33	0.25	0.15	0.04	0.1075	0.0144	99.44	0.0129
96	d71-1	50.78	1.73	13.99	11.74	0.20	6.36	10.63	2.85	0.31	0.18	0.02	0.1376	0.0191	98.96	0.0176
96	d71-1	50.91	1.68	13.86	11.66	0.25	6.27	10.72	2.69	0.31	0.18	0.02	0.1435	0.0197	98.70	0.0182
97	d71-3	50.56	1.58	14.08	11.24	0.18	6.48	10.97	2.65	0.29	0.19	0.04	0.1315	0.0221	98.41	0.0206
97	d71-3	50.95	1.58	14.16	10.99	0.18	6.66	11.04	2.60	0.28	0.18	0.04	0.1362	0.0218	98.83	0.0203
100	d73-3	50.13	1.33	16.12	9.85	0.20	7.94	11.72	2.54	0.41	0.17	0.04	0.0905	0.0252	100.56	0.0237
100	d73-3	49.89	1.30	16.05	9.44	0.11	7.90	11.68	2.54	0.41	0.18	0.05	0.0980	0.0230	99.66	0.0215
101	d73-5	50.69	0.70	15.84	8.54	0.12	9.57	13.60	1.85	0.03	0.08	0.08	0.0839	0.0041	101.20	0.0026
101	d73-5	50.74	0.76	15.88	8.61	0.17	9.49	13.57	1.82	0.02	0.06	0.08	0.0865	0.0025	101.28	0.0010

Group	Sample	SiO ₂	TiO ₂	Al ₂ O ₃	FeO*	MnO	MgO	CaO	Na ₂ O	K ₂ O	P ₂ O ₅	Cr ₂ O ₃	S	Cl	Total	Corrected Cl
102	d73-6	50.95	1.03	16.09	8.28	0.15	8.80	12.86	2.34	0.27	0.19	0.07	0.0935	0.0168	101.13	0.0153
102	d73-6	51.33	0.97	15.96	8.27	0.15	8.89	12.85	2.33	0.27	0.19	0.06	0.0869	0.0153	101.37	0.0138
103	w47b	49.50	1.21	16.47	8.43	0.12	7.94	11.95	2.79	0.68	0.19	0.06	0.0949	0.0401	99.48	0.0386
103	w47b	49.98	1.25	16.54	8.45	0.15	7.87	11.95	2.70	0.66	0.19	0.03	0.0908	0.0396	99.91	0.0381
107	w48a	51.29	0.93	15.42	9.17	0.18	8.33	13.03	2.19	0.12	0.11	0.06	0.1051	0.0083	100.94	0.0068
107	w48a	51.23	0.93	15.47	9.17	0.11	8.48	12.96	2.06	0.13	0.11	0.05	0.0982	0.0095	100.81	0.0080
112	d79-1	51.16	1.08	15.40	8.85	0.10	8.36	12.81	2.33	0.10	0.07	0.06	0.1020	0.0092	100.44	0.0050
112	d79-1	51.28	1.07	15.33	8.96	0.13	8.52	12.82	2.26	0.10	0.12	0.04	0.1042	0.0077	100.75	0.0035
113	w53a	51.53	1.34	14.92	9.58	0.18	7.81	12.32	2.69	0.12	0.14	0.07	0.1135	0.0094	100.81	0.0052
113	w53a	51.60	1.36	14.94	9.44	0.20	7.76	12.30	2.64	0.11	0.13	0.06	0.1088	0.0088	100.65	0.0046
114	d76-2	49.75	1.28	17.38	9.11	0.18	8.30	11.33	2.96	0.18	0.11	0.04	0.0911	0.0128	100.72	0.0113
114	d76-2	49.42	1.27	17.46	9.21	0.15	8.23	11.28	3.01	0.19	0.13	0.04	0.092	0.0122	100.49	0.0107
116	d77-2	51.63	1.52	15.88	9.47	0.11	8.19	11.54	2.79	0.13	0.15	0.05	0.1023	0.0089	101.57	0.0074
116	d77-2	50.70	1.49	15.67	9.75	0.17	8.00	11.20	2.71	0.14	0.14	0.04	0.1077	0.0079	100.13	0.0064
119	d58-1	47.84	0.97	17.30	10.80	0.13	8.95	11.13	2.58	0.06	0.06	0.05	0.1095	0.0034	99.99	0.0019
119	d58-1	48.34	1.00	17.35	10.88	0.19	9.04	11.15	2.62	0.06	0.08	0.05	0.1183	0.0047	100.89	0.0032
120	d58-4	48.28	1.22	16.65	11.14	0.13	8.24	11.38	2.72	0.07	0.08	0.04	0.1323	0.0035	100.08	0.0020
120	d58-4	48.67	1.23	16.59	11.28	0.22	8.38	11.42	2.66	0.06	0.08	0.02	0.1321	0.0045	100.76	0.0030
124	w44a	50.40	2.35	13.57	13.15	0.23	4.81	9.44	3.37	0.75	0.32	0.00	0.1226	0.0792	98.59	0.0777
124	w44a	50.12	2.22	13.60	12.92	0.23	4.83	9.21	3.28	0.76	0.32	0.01	0.1307	0.0744	97.71	0.0729
125	w45a	50.15	1.93	14.22	11.68	0.19	6.01	10.65	3.04	0.61	0.30	0.00	0.122	0.0624	98.97	0.0609
125	w45a	50.32	1.85	14.15	11.46	0.14	5.96	10.66	3.04	0.60	0.29	0.01	0.1266	0.0615	98.66	0.0600
	MD37.d2-3	51.66	1.81	14.29	10.82	0.16	6.76	11.25	2.75	0.34	0.18	0.03	0.1240	0.0132	100.17	0.0117
	MD37.d2-3	51.68	1.75	14.45	10.80	0.16	6.68	11.14	2.73	0.33	0.20	0.02	0.1207	0.0147	100.07	0.0132
	MD37.d3-3	53.08	1.67	14.79	10.00	0.17	6.86	10.61	2.82	0.39	0.19	0.03	0.1098	0.0211	100.74	0.0196
	MD37.d3-3	52.85	1.67	14.76	10.15	0.16	6.75	10.55	2.83	0.38	0.18	0.01	0.1130	0.0198	100.42	0.0183

Appendix 5: Analyses of Kakanui Augite.

This table presents the results of analyzing augite standard USNM 122142, from Kakanui, New Zealand (Jarosewich, 1980). To establish the background Cl level within the microprobe this augite standard was analyzed several times over the course of a run. Because the augite contains no Cl, any measured Cl represented the background level of Cl. The average measurement over the four runs of this background Cl level was then subtracted from each of the sample analyses. This correction was 15 ppm Cl with a range of 13-19 ppm over the four runs. The exception to this was the second half of the fourth run in which the Cl background level was much higher than normal with an average of 42 ppm. Samples measured during this period were corrected for a background level of 42 ppm instead of 15 ppm. Operating conditions are listed in the text.

Blank	Run #	Counting times		SiO ₂	TiO ₂	Al ₂ O ₃	FeO*	MnO	MgO	CaO	Na ₂ O	K ₂ O	P ₂ O ₅	Cr ₂ O ₃	S	Cl	Total
		Cl (sec)	S(sec)														
Kakanui Augite	1	500	20	50.25	0.92	8.56	6.41	0.09	16.69	16.51	1.25	0.00	0.03	0.15	0.0179	0.0013	100.88
Kakanui Augite	1	500	20	49.95	0.87	8.60	6.25	0.14	16.69	16.65	1.28	0.00	0.01	0.15	0.0192	0.0013	100.60
<i>Average</i>				<i>50.10</i>	<i>0.90</i>	<i>8.58</i>	<i>6.33</i>	<i>0.11</i>	<i>16.69</i>	<i>16.58</i>	<i>1.26</i>	<i>0.00</i>	<i>0.02</i>	<i>0.15</i>	<i>0.0186</i>	<i>0.0013</i>	<i>100.74</i>
Kakanui Augite	2	1000	60	50.64	0.79	8.51	6.24	0.13	16.41	16.24	1.21	0.00	0.03	0.16	0.0032	0.0019	100.36
Kakanui Augite	2	1000	60	50.43	0.82	8.68	6.19	0.09	16.22	16.19	1.22	0.00	0.02	0.16	0.0032	0.0017	100.02
<i>Average</i>				<i>50.53</i>	<i>0.81</i>	<i>8.59</i>	<i>6.21</i>	<i>0.11</i>	<i>16.32</i>	<i>16.21</i>	<i>1.22</i>	<i>0.00</i>	<i>0.02</i>	<i>0.16</i>	<i>0.0032</i>	<i>0.0018</i>	<i>100.19</i>
Kakanui Augite	3	1000	60	50.29	0.78	8.57	6.08	0.09	16.45	16.36	1.22	0.00	0.02	0.16	0.0220	0.0018	100.03
Kakanui Augite	3	1000	60	49.46	0.80	8.47	6.00	0.17	16.55	16.35	1.27	0.00	0.02	0.16	0.0032	0.0015	99.26
<i>Average</i>				<i>49.87</i>	<i>0.79</i>	<i>8.52</i>	<i>6.04</i>	<i>0.13</i>	<i>16.50</i>	<i>16.35</i>	<i>1.25</i>	<i>0.00</i>	<i>0.02</i>	<i>0.16</i>	<i>0.0126</i>	<i>0.0017</i>	<i>99.65</i>
Kakanui Augite	4	1000	60	49.78	0.84	8.39	6.35	0.12	16.50	16.11	1.26	0.01	0.02	0.14	0.0049	0.0013	99.52
Kakanui Augite	4	1000	60	49.56	0.85	8.39	6.12	0.10	16.18	16.29	1.37	0.01	0.04	0.16	0.0047	0.0048	99.07
Kakanui Augite	4	1000	60	50.22	0.83	8.39	6.32	0.17	16.34	16.51	1.22	0.00	0.01	0.16	0.0013	0.0035	100.18
<i>Average</i>				<i>49.85</i>	<i>0.84</i>	<i>8.39</i>	<i>6.26</i>	<i>0.13</i>	<i>16.34</i>	<i>16.30</i>	<i>1.28</i>	<i>0.01</i>	<i>0.02</i>	<i>0.15</i>	<i>0.00</i>	<i>0.0032</i>	<i>99.59</i>

Average blank value of the first three runs and the first part of the fourth run:
15 ppm

Average blank value of the second part of the fourth run:
42 ppm

Appendix 6: Calculation of Eight Values.

The elements FeO^* , Na_2O , TiO_2 , K_2O and P_2O_5 were corrected for shallow-level crystal fractionation to a value of 8 wt. % MgO using methods similar to those developed by Klein and Langmuir (1987). A second order polynomial fit to the respective oxide variations as a function of MgO was made on a segment by segment basis. This table presents the equation used to calculate the eight values and the equations for each of the polynomial fits.

A. This is the equation used to calculate the eight values. Depending on the element value being calculated, the Na₂O measured value will be replaced with the FeO* measured value, the TiO₂ measured value, etc. The a and b values are taken from the polynomial fits made to the individual segments. Eight values were calculated for each chemical group.

$$Y_8 = a(8)^2 + b(8) + (\text{Na}_2\text{O measured}) - (a * (\text{MgO measured})^2) - (b * \text{MgO measured})$$

B. Equations for the polynomial fits made to each of the segments. A fit was also made to the ASP data set as a whole for comparison. Off-axis samples and those samples with less than 5 wt.% MgO were not included in the polynomial fits.

	FeO*	Na₂O
All segments	y= -0.0291x ² - 0.3925x + 14.606 r ² =0.6635	y= -0.0473x ² + 0.4881x + 1.5528 r ² =0.569
Segment L	y= 0.213x ² - 4.1487x + 29.092 r ² =0.5804	y= 0.2009x ² - 3.1956x + 15.291 r ² =0.4497
Segment K	y= -0.4144x ² + 4.6155x - 1.1468 r ² =0.7785	y= -0.4356x ² - 6.4192x - 21.636 r ² =0.2812
Segment J4	y= 0.1703x ² - 3.7032x + 28.343 r ² =0.6764	y= -0.1444x ² + 2.1895x - 5.7819 r ² =0.0507
Segment J3	y= -0.5126x ² + 7.233x - 15.42 r ² =0.4333	y= 2.993x ² - 48.908x + 201.98 r ² =0.8124
Segment J2	y= 0.1845x ² - 3.6362x + 27.011 r ² =0.9028	y= -0.0433x ² + 0.4131x + 1.8606 r ² =0.9338
Segment J1	y= 0.5896x ² - 9.0691x + 44.924 r ² =0.3672	y= 0.1051x ² - 1.6533x + 9.0072 r ² =0.3985
Segment I2	y= -0.1259x ² + 0.9856x + 9.5785 r ² =0.4815	y= 0.0456x ² - 0.8239x + 5.9681 r ² =0.9318
Segment I1	y= 0.1489x ² - 3.436x + 27.088 r ² =0.9716	y= -0.0781x ² + 0.8603x + 0.296 r ² =0.9464
Segment H	y= -0.9661x ² + 16.429x - 60.489 r ² =0.0656	y= 0.1197x ² - 2.4731x + 14.476 r ² =0.6339
Segment G	y= 2.9348x ² - 48.154x + 206.28 r ² =0.927	y= 0.9503x ² - 15.714x + 67.32 r ² = 0.7337
	TiO₂	K₂O
All segments	y= -0.0386x ² + 0.2226x + 2.0099 r ² = 0.8369	y= 0.0407x ² - 0.7287x + 3.3706 r ² =0.5684
Segment L	y= 0.0469x ² - 0.9415x + 6.0514 r ² =0.3443	y= 0.0281x ² - 0.4496x + 1.9457 r ² =0.3662
Segment K	y= -0.0209x ² - 0.1988x + 4.2361 r ² = 0.8986	y= 0.0288x ² - 0.492x + 2.1903 r ² =0.5773
Segment J4	y= -0.0946x ² + 1.2217x - 2.3435 r ² =0.445	y= 0.0165x ² - 0.2944x + 1.3633 r ² =0.5601

	TiO₂	K₂O
Segment J3	$y = 2.2952x^2 - 38.081x + 159.04$ $r^2 = 0.8509$	$y = 0.3632x^2 - 5.81x + 23.299$ $r^2 = 0.8686$
Segment J2	$y = 0.0286x^2 - 0.7771x + 5.6608$ $r^2 = 0.9661$	$y = 0.0019x^2 - 0.1112x + 0.9647$ $r^2 = 0.765$
Segment J1	$y = 0.197x^2 - 3.1066x + 13.699$ $r^2 = 0.4563$	$y = 0.0346x^2 - 0.5695x + 2.6088$ $r^2 = 0.3249$
Segment I2	$y = -0.0446x^2 + 0.3027x + 1.7592$ $r^2 = 0.6648$	$y = 0.0062x^2 - 0.2509x + 1.8555$ $r^2 = 0.8496$
Segment I1	$y = 0.0546x^2 - 1.0669x + 6.1378$ $r^2 = 0.9845$	$y = 0.0133x^2 - 0.2195x + 1.1382$ $r^2 = 0.9892$
Segment H	$y = -0.0157x^2 - 0.31x + 2.4343$ $r^2 = 0.7379$	$y = 0.2043x^2 - 3.772x + 17.511$ $r^2 = 0.5215$
Segment G	$y = 1.3987x^2 - 22.854x + 94.457$ $r^2 = 0.8433$	$y = -0.3175x^2 + 5.1111x - 20.421$ $r^2 = 0.7845$
	P₂O₅	
All segments	$y = 0.0035x^2 - 0.1016x + 0.7088$ $r^2 = 0.7765$	
Segment L	$y = -0.0126x^2 + 0.1531x - 0.2837$ $r^2 = 0.2559$	
Segment K	$y = -0.002x^2 - 0.0206x + 0.4021$ $r^2 = 0.7374$	
Segment J4	$y = 0.0181x^2 - 0.3166x + 1.4879$ $r^2 = 0.4283$	
Segment J3	$y = 0.5319x^2 - 8.7594x + 36.146$ $r^2 = 0.9497$	
Segment J2	$y = 0.0031x^2 - 0.0862x + 0.6185$ $r^2 = 0.9086$	
Segment J1	$y = 0.0512x^2 - 0.7712x + 3.0536$ $r^2 = 0.3239$	
Segment I2	$y = -0.0049x^2 + 0.015x + 0.335$ $r^2 = 0.8758$	
Segment I1	$y = -0.0094x^2 + 0.1109x - 0.1539$ $r^2 = 0.7547$	
Segment H	$y = 0.035x^2 - 0.6758x + 3.309$ $r^2 = 0.6833$	
Segment G	$y = 0.0229x^2 - 0.382x + 1.7045$ $r^2 = 0.2951$	